Fall 1-31-2001

Numerical studies of Newtonian and viscoelastic fluids

Felix J. Alcocer
New Jersey Institute of Technology

ABSTRACT

NUMERICAL STUDIES OF NEWTONIAN AND VISCOELASTIC FLUIDS

by
Felix J. Alcocer

The direct numerical simulation (DNS) approach is used to understand the flow behavior of Newtonian and viscoelastic fluids in porous materials, four-to-one contraction and the flow of a Newtonian fluid past an airfoil.

In simulations the viscoelastic fluid is modeled by the finitely extensible nonlinear elastic (FENE) dumbbell and Oldroyd-B models. The finite element method (FEM) is used to discretize the flow domain. The DNS results show that the permeability of a periodic porous medium depends on the wavelength used for arranging particles in the direction of flow. Specifically, it is shown that for a given particle size and porosity the permeability varies when the distance between particles in the flow direction is changed. The permeability is locally minimum for kD $\approx$ 7.7 and locally maximum for kD $\approx$ 5.0; where k is the wave number and D the diameter. A similar behavior holds for a viscoelastic fluid, except that the variation of permeability with kD is larger than for the Newtonian case.

For flow in the four-to-one contraction, it is found that the stress near the $3\pi/2$ corner is singular and that the singularity is stronger than for a Newtonian liquid. In the region away from the walls, the stress varies as $r^{-0.47}$ and near the walls it varies as $r^{-0.61}$. Since the singularity is integrable, the flow away from the corner is not effected when the flow around the corner is resolved by using a radial mesh with sufficient resolution in the tangential direction at the corner.

The DNS approach is also used to demonstrate that the boundary layer separation on the upper surface of the airfoil can be suppressed by placing injection and suction regions on the upper surface. The simulations are performed for $Re \leq 500$ and angle of attack up to 40^{o}. Analysis of numerical results shows that the pressure contribution to drag decreases when the boundary layer separation is avoided. The viscous contribution to drag, however, increases and thus there is only a negligible decrease in the total drag for $Re \leq 500$. Another beneficial effect of suction and injection is that the pressure contribution to the lift increases and the stall is avoided.

NUMERICAL STUDIES OF NEWTONIAN AND VISCOELASTIC FLUIDS

by
Felix J. Alcocer

A Dissertation
Submitted to the Faculty of
New Jersey Institute of Technology
In Partial Fulfillment of the Requirements for the Degree of
Doctor of Philosophy in Mechanical Engineering

Department of Mechanical Engineering

January 2001

APPROVAL PAGE

NUMERICAL STUDIES OF NEWTONIAN AND VISCOELASTIC FLUIDS

Felix J. Alcocer

Dr. Pushpendra Singh, Dissertation Advisor — Date
Assistant Professor of Mechanical Engineering, NJIT

Dr. Rong-Yaw Chen, Committee Member — Date
Professor of Mechanical Engineering, NJIT

Dr. Nadine Aubry, Committee Member — Date
Professor and Acting Chair of Mechanical Engineering, NJIT

Dr. Kwabena A. Narh, Committee Member — Date
Associate Professor of Mechanical Engineering, NJIT

Dr. Burt S. Tilley, Committee Member — Date
Assistant Professor of Mathematical Sciences, NJIT

BIOGRAPHICAL SKETCH

Author: Felix J. Alcocer

Degree: Doctor of Philosophy in Mechanical Engineering

Date: January 2001

Undergraduate and Graduate Education:

- Doctor of Philosophy in Mechanical Engineering
  New Jersey Institute of Technology
  Newark, New Jersey, 2001

- Master of Science in Mechanical Engineering
  New Jersey Institute of Technology
  Newark, New Jersey, 1997

- Bachelor of Science in Mechanical Engineering
  Pontifical Catholic University of Peru
  Lima, Peru, 1991

Major: Mechanical Engineering

Publications and Presentations:

Felix J. Alcocer, Vimal Kumar, P. Singh, "Permeability of periodic porous media", Physical Review E vol. 59, number 1, 711-714, January 1999.

Felix J. Alcocer, P. Singh, "Finite element simulations of viscoelastic porous media flows", Proceedings of the 1998 Conference of the Society of Rheology, Monterery, California, October 1998.

Felix J. Alcocer, P. Singh,"Numerical simulations of free surface viscoelastic flows using the level set method", Proceedings of the 1998 Conference of the Society of Rheology, Monterery, California, October 1998.

Dedicated to my beloved family

ACKNOWLEDGMENT

The author would like to express his sincere appreciation to his advisor, Dr. Pushpendra Singh, for his guidance, friendship and moral support throughout this research. This work would have never been accomplished without his help or advice.

Special thanks to Dr. Nadine Aubry, Dr. Rong Chen, Dr. Kwabena Narh and Dr. Burt Tilley for serving as members of the committee. The author would like to thank all of his research group colleagues for their support and cooperation during the research.

The author also would like to acknowledge the New Jersey Institute of Technology for giving him the opportunity to serve as a teaching assistant in the Mechanical Engineering department and for the stipend awards from the graduate studies office during the period of 1997-2000.

TABLE OF CONTENTS

TABLE OF CONTENTS
(Continued)

Chapter **Page**

LIST OF FIGURES

Figure **Page**

LIST OF FIGURES
(Continued)

LIST OF FIGURES
(Continued)

LIST OF FIGURES
(Continued)

LIST OF FIGURES
(Continued)

LIST OF FIGURES
(Continued)

CHAPTER 1

INTRODUCTION

1.1 Overview

The objective of this dissertation is to numerically study the fluid dynamics of Newtonian and viscoelastic fluids, though emphasis is primarily on the viscoelastic fluids. Specifically, the direct numerical simulation (DNS) approach is used to study Newtonian and viscoelastic flows in the following problems: Newtonian flow past an airfoil with suction and injection; flow of viscoelastic fluids in the four-to-one contraction and the nature of singularity near the $3\pi/2$ corner; and flow of Newtonian and viscoelastic liquids through periodic porous medium and the dependence of permeability on the wave length of periodic porous medium.

1.2 Newtonian Fluids

It is well known that for a Newtonian fluid, such as water, the shear stress is proportional to the shear rate. The coefficient of proportionality is called the viscosity. In other words, the viscosity of a Newtonian liquid is independent of the magnitude of the shear rate. Many common fluids, e.g. oils, air, etc, are Newtonian.

The dynamics behavior of Newtonian fluids is described by the following equations: the continuity or mass conservation (assuming incompressibility), the momentum equation, and the energy equation in the event the temperature one of the unknown variables.

For non-Newtonian liquids the stresses is nonlinearly related to the shear rate, and therefore the shear viscosity is not constant. A particular case of non-Newtonian fluids is

the viscoelastic fluid for which the stress not only depends on the current shear rate but also on the past strain history. Thus, the numerical solution of non-Newtonian fluids is much more difficult to obtain compared to that for the non-Newtonian liquids.

1.3 Viscoelastic Fluids

As noted above, the term 'viscoelastic fluids' is used to describe a class of non-Newtonian fluids for which the response is a combination of the viscous and elastic behavior. Some examples of these fluids are: polymers, paints, rubbers, lubricants, suspensions, etc. A study of viscoelastic fluids is important because of their wide spread use in a range of industrial applications.

Newtonian fluids, as previously discussed, are governed by the Navier-Stokes equations, as their response is purely viscous. An elastic body, on the other hand, is governed by the equations of elasticity. The response of a viscoelastic fluid is a combination of the viscous and the elastic body responses.

The simplest model used for describing these fluids is the Maxwell model, which represents a combination of a spring and a dashpot in series, see Figure 1.1. The spring accounts for the fluid elasticity and the dashpot accounts for its viscous nature. Clearly, when the applied force is zero the stress in the system goes to zero as the spring relaxes as a function of time, see Figure 1.1. The relaxation time for this system is equal to $\tau=\mu/G$, where G is the spring constant and μ is the dashpot friction coefficient. Similarly, when the system is subjected to a sudden force the stress in the system grows with time and reaches 90% of the steady state value when t is equal the relaxation time, see Figure 1.1.

$$\sigma + \tau\dot{\sigma} = \mu\dot{\gamma}$$

σ = Force
$\dot{\gamma}$ = Strain rate

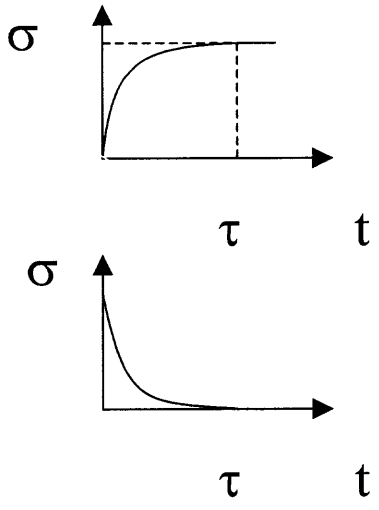

Figure 1.1 The stress growth and relaxation for the Maxwell model. Notice that it takes time of order τ for the stress to buildup and relax.

The viscoelastic nature of polymeric fluids can be seen in the rod climbing experiment, see Figure 1.3. In this experiment, a rod is rotated in the bucket filled with the viscoelastic fluid. It is well known that when the rod is rotated in the Newtonian fluid, (see Figure 1.2) the fluid near the rod surface is thrown away by the centrifugal force and thus the fluid surface near the rod goes down. For the viscoelastic fluid, on the other hand, the fluid near the rotating rod climbs.

The viscoelastic fluid near the rod climbs because the material fluid elements along the streamline are in a stretched state similar to that of a stretched rubber band. More specifically, for the viscoelastic liquids the primary normal stress difference is non-zero second, and thus the magnitude of normal stress in the radial direction is smaller than in circumferential direction.

As noted above, the elastic nature of viscoelastic fluids is characterized by a relaxation time. The relaxation time is a measure of the time the fluid takes to reach a state of equilibrium after the external stress applied on the fluid is removed. For real polymeric liquids the relaxation time depends on many factors including the molecular weight and its polymeric nature. In a flow problem, the elastic nature of a viscoelastic fluid can be quantified using a dimensionless relaxation time called Deborah number (De) which is defined to be the ratio of the relaxation time and the flow time scale.

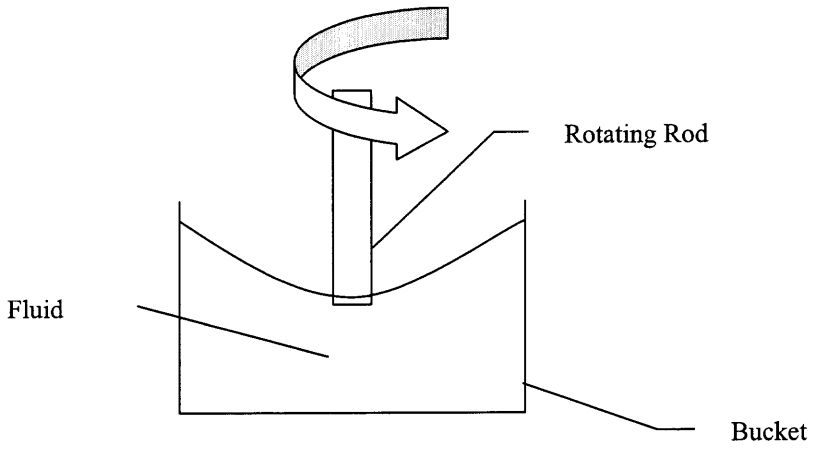

Figure 1.2 The fluid level near the rotating rod in a Newtonian fluid is lowered as the centrifugal force near the rod is larger than away from the rod.

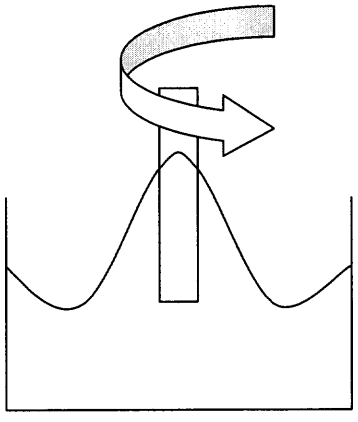

Figure 1.3 The fluid rises next to the rotating rod in a viscoelastic fluid as the fluid near the rod behaves like a stretched rubber band.

Next, the constitutive relation between the stress and the strain that is needed to close the momentum equation is discussed. The idea is to find a relation between the stress and the past strain rate history for the fluid under consideration. In the Navier-Stokes equations the stress is assumed to depend linearly on the current strain rate. But, since for viscoelastic liquids, the stress depends on the entire past strain history of the fluid, the constitutive equation takes a far more complex form. The popular constitutive models are: Maxwell, Oldroyd-B, White-Metzner, Integral, Giesekus, FENE, etc. For example, the integral form of the Maxwell model is:

$$\sigma(t) = \frac{\mu}{\tau} \int_{-\infty}^{t} e^{-\left(\frac{t-t'}{\tau}\right)} \gamma'(t') dt'$$

where t' is a past time and t is the present time.

Clearly, as the system of equations for a viscoelastic liquid is highly nonlinear, it is difficult to obtain an analytical solution for most problems. Nowadays, with the aid of computers and faster numerical methods, it is possible to numerically solve these nonlinear governing equations. In Chapter 2, the numerical method used in this work for solving the constitutive equation for the stress along with the mass and momentum conservation equations for a given flow field is described.

The results of direct numerical simulation help us in understanding the behavior of viscoelastic fluids. This approach is valuable in many practical flow problems. Also note that recent research activities have improved the numerical methods for solving the viscoelastic flow problems.

The two main problems in the numerical solution of viscoelastic flows are that the method may not converge at high Deborah numbers and that the number of unknowns is

more than twice of that for the Newtonian flow problems. Since the number of unknowns are more than twice of that for Newtonian flows, the dimension of matrices obtained during the solution procedure is more than twice as large as for Newtonian liquids, and the storage needed is more than four times of that for the Newtonian liquids. Therefore, the memory requirement limits the problems that can be studied numerically. The matrix free approaches for solving viscoelastic flow problem are thus essential, especially for solving industrial scale problems. In a matrix free approach the global matrices for the linear systems are not assembled. In our finite element code a conjugate gradient algorithm is used for solving the linear system matrix in which the product of a vector with the linear system matrix is computed directly without assembling the matrix.

In Chapter 3, a brief description of the numerical algorithm used for the solution of viscoelastic fluid flow problems is given. A detailed information can be found in Singh and Leal 1993. The method was developed for the constitutive models derived from nonlinear dumbbell theory and in particular applied for the specific case of the finitely extendable nonlinear elastic (FENE) dumbbell model proposed by Chilcott and Rallison (1988). The numerical algorithm is built around two unique features, the first is that it was implemented using a third-order accurate finite-element upwind scheme to discretize the convection term in the equation that describes the evolution of stress (or the second moment of the conformation distribution) in the FENE dumbbell model. This scheme was introduced by Tabata and Fujima (1991) for discretizing the convection term in the Navier-Stokes equation. The second unique feature of the numerical algorithm is that initial value problems are solved to obtain both the velocity and the configuration tensor (the configuration tensor is proportional to the second moment of the distribution

function for the end-end vector of a dumbbell). This allows to implement an algorithm which explicitly forces the configuration tensor to stay positive definite at all times, and, therefore, avoids forbidden negative values (see Joseph, 1990). These forbidden values cannot be easily avoided when an iterative method is used to seek a steady solution by dropping the time-derivative terms. Moreover, it is quite obvious that by solving the time-dependent equations even solutions for problems that may not have a steady solution can be obtained.

The method also shows that the accuracy of the third-order upwind scheme and the time-dependent algorithm that keeps the configuration tensor positive definite provides a straightforward numerical method that is stable at relatively large Deborah numbers. The FENE dumbbell constitutive equations are solved along with the momentum and continuity equations at small Reynolds numbers using an operator-splitting technique in which the time-discretization is second-order accurate.

In the FENE dumbbell model the stress tensor contains two distinct contributions, one coming from the conformation of the polymer and the other coming form the solvent. The solvent contribution is viscous in nature and appears as the highest-order term in the momentum equation, which makes it elliptic. Therefore, when this solvent contribution is present, the momentum equation cannot change type, i.e., it does not become hyperbolic for certain flows or for certain portions of the flow domain as the case with the Maxwell model (see Joseph and Saut, 1986, Zanden and Hulsen, 1998, Guillope and Saut, 1990, Rajagopalan *et al.* 1990). Thus, certain complications associated with the numerical solution of flow problems using the Maxwell model are avoided.

Nevertheless, in spite of the fact that the problems associated with a change of type of steady flow do not arise for the FENE dumbbell or Oldroyd-B type models, it is still difficult to simulate flows at large Deborah numbers. The common observation for both the Maxwell and Oldroyd-B type models is that a Deborah number exists at which the determinant of the configuration tensor becomes negative, i.e., one of the principle values of the configuration tensor becomes negative (see King *et al.*, 1988; Marchal and Crochet, 1986,1987). This Deborah number delineates the upper limit for which a reasonably smooth numerical solution can be obtained. It can be shown that in an analytical solution the configuration tensor cannot become negative. The fact that it does become negative in a numerical scheme is therefore a consequence of numerical errors. For the Maxwell model, an initial-value problem with a negative configuration tensor is ill posed (unstable to short waves). Therefore, if the configuration tensor becomes negative in a numerical simulation for the Maxwell model, then its further evolution in time is unstable to short waves (see Joseph, 1990). On the other hand, the FENE dumbbell model is not ill posed because of the smoothing action of the solvent viscosity. However, it is still unstable in the sense that for a given fixed strong flow field and negative initial value of the configuration tensor, the configuration tensor takes ever increasing negative values with time. Therefore, for both types of models, it is very important that the configuration tensor stays positive in a numerical solution.

There have, in fact, been some recent efforts to improve upon the range of Deborah numbers that can be achieved numerically, in which the configuration tensor remains positive. For example, Marchal and Crochet (1986, 1987) improved this range by constructing special elements in which they assign more degrees of freedom per element

to the stress. For these special elements they have implemented the streamline upwind and Petrov-Galerkin schemes. On the other hand, Amstrong, Brown, and coworkers (see King *et al.*, 1988; Burdette *et al.*, 1989; Northey *et al.*, 1990; Rajagopalan *et al.*, 1990; and others) have developed the so-called EEME and EVSS methods which utilize elements that have the same level of resolution for the stress and velocity components. It is difficult to make a fair comparison between these approaches because the special elements of Marchal and Crochet have a different level of resolution of the velocity and stress components. On the other hand, it is important to note that both approaches give better results as the mesh is refined, i.e., flows at larger Deborah number can be computed by using a finer mesh. The fact that Crochet's special elements have more degrees of freedom for the stress, and that the accuracy of the elements improves with the mesh refinement, both suggest that the dominant factor in achieving a better performance is, an increased accuracy for the stress field. In particular, if the velocity field is known (say given) and is independent of the stress field, then the Deborah number range can be improved just by refining the mesh or otherwise improving accuracy for the stress components. This simpler problem is important to study because there is no coupling between the velocity and stress fields, and so the numerical complications of the full problem can be isolated. In particular, if for the simpler problem the positive definiteness criteria cannot be satisfied, and if there is not a significant improvement in the upper limit of the Deborah number that can be numerically simulated using the same mesh as for the full problem, then it may be concluded that the numerical integration scheme for the stress equation is definitely unsatisfactory, and that it is responsible for the numerical failure in the full problem (see King *et al.*, 1988).

In Chapter 4, the permeability of a periodic porous media has been investigated in 2-D. The definition of Darcy's law is used to calculate the value of the permeability as a function of the dimensionless wave number kD, where k is the wave number based on the distance between particles in the stream-wise direction and D is the diameter. To isolate the kD dependence, the diameter D and the porosity are held fixed. The latter is achieved by making the product of distance between particles in the cross-stream and stream-wise directions constant. The numerical results show that the permeability increases with kD, but the increase is not monotonic. In particular, the permeability decreases for $\sim 5 < kD < \sim 7.7$, and becomes locally minimum at $kD \approx 7.7$. This value of kD is significant because it is the smallest wave number for which the stream-wise area-fraction spectrum is zero. For $kD < 5$ and $7.7 < kD < 11$, the permeability increases with kD. Numerical simulations also show that for $kD \approx 7.7$ the pressure distribution in the cross-stream direction is relatively flat which again is a consequence of the fact that the area-fraction distribution in the flow direction is approximately constant.

In Chapter 5, the 2-D permeability of a periodic porous media has been extended to viscoelastic fluids. The permeability has been calculated as a function of the Deborah number (De), a dimensional measure of the relaxation time and the dimensionless wave number kD. Again, the definition of Darcy's law is used to calculate the value of the permeability for viscoelastic fluids, though such a law is not valid due to the nonlinear behavior of this kind of fluids. The variations found in the permeability imply that the permeability of a periodic array can be modified significantly by changing the kD in the flow direction.

In Chapter 6, the 2-D numerical solution of a viscoelastic fluid passing a four-to-one contraction has been studied. A radial mesh is used near the corner of the contraction, which allows for independent mesh refinements in the radial and tangential directions. At the corner, there exists a singularity that makes the stress singular. It was possible to approximate the behavior of both the velocity and configuration fields in the vicinity of the corner by generalized power laws with exponents depending on the angular position. The numerical solution is used to find the exponent that satisfies this power law for the viscoelastic flow near the singular point (the corner). The radial mesh at the corner also allows us to obtain mesh convergent solutions away from the mesh.

To prevent the unwanted separation of the boundary layer for a flow past an airfoil is the main objective of Chapter 7. The NACA (National Advisory Committee for Aeronautics) airfoil 0012-64 has been used for this numerical study. The two dimensional simulations were carried out for different angles of attack. For high the angle of attacks, i.e., the angles greater than 15^{o}, and for high values of Re's the boundary layer on the upper surface separates. The Reynolds number in this study is between 100 and 1000. By preventing the separation of the boundary layer on an airfoil one avoids stalling and also an undesirable increase in the drag force, which increases when the boundary layer separate. The lift force decreases suddenly when the airfoil stalls. Also when the boundary layer separates, it creates vortex shedding which produce fluctuations over the airfoil thus the airfoil vibrates. For some applications it may be important to reduce or suppress these vibrations by preventing the separation of the boundary layer. The focus of this numerical work is to prevent the separation of the boundary layer by injecting fluid near the leading edge and sucking it close to the trailing edge. The suction and injection

velocities are varied in a range that is necessary for reattaching the boundary layer. The fluid injected mixes with the main stream flow and gives an additional momentum to the fluid in the boundary layer, which prevents the boundary layer separation. It may also help in reattaching the boundary layer when the separation has already occurred. The effect of using different injection velocities is also discussed.

To summarize, the motivation for the present study is to use the DNS approach to understand the behavior of Newtonian and viscoelastic fluids in these applications. By getting a better understanding of the properties of Newtonian and viscoelastic fluids we will be able to help industries directly concerned, in understanding the problems and for the designs for future applications. Also the numerical solutions found throughout this dissertation can be comparable and corroborated by the ones obtained by other researchers not only analytically but also numerically. Therefore, the gap between analytical and numerical solution could be bridged.

CHAPTER 2

GOVERNING EQUATIONS

It is assumed that the fluids considered in this study are incompressible (constant density) and that they satisfy the continuity (or mass conservation) and momentum equations.

For viscoelastic fluids, as previously stated, the constitutive equation which is the relation between the stress and the strain rate is also needed for closing the system of equations. Since the stress for viscoelastic liquids depends on the entire past strain history, the constitutive equation takes a relatively more complex form. In these simulations, the FENE dumbbell and Oldroyd-B models are used for modeling the viscoelastic fluids.

The governing equations are made dimensionless by using the following characteristic velocity, length, and time scales: the characteristic velocity U, the particle diameter D, and time $t_c = \frac{D}{U}$ respectively.

The following are the nondimensionalized continuity and momentum equations:

$$\nabla \cdot u = 0, \tag{2.1}$$

$$Re\left[\frac{\partial u}{\partial t} + u \cdot \nabla u\right] = -\nabla p + \left[\nabla \cdot T + \nabla^2 u\right]$$

with the polymer contribution to the stress for the viscoelastic effects calculated from

$$T = \frac{c}{De} f(trA)A \tag{2.2}$$

with

$$\frac{\partial A}{\partial t} + u.\nabla A = A\nabla u + \nabla u^T.A - \frac{f(trA)}{De}(A - I) \tag{2.3}$$

Here **I** is the identity tensor, **A** is the ensemble average of the second moment of the end-to-end vector **R** and tr**A** is the magnitude of the end-to-end vector **R** for the dumbbell scaled with the square of the equilibrium radius of gyration of a Gaussian chain. The parameters that appear explicitly in equation (2.1) and (2.2) are: the Reynolds number, ***Re*** $= \frac{UD}{\nu}$, defined in terms of the zero-shear-rate limit of the kinematic viscosity of the polymer solution ν, and the Deborah number which is defined as:

$$De = \frac{U}{D}\lambda$$

the ratio of the characteristic relaxation time of the polymer λ and the time scale t_c. The parameter

$$c \equiv \frac{\nu - \nu_s}{\nu_s},$$

which is a measure of the polymer concentration expressed in terms of the fractional contribution of the polymer to the zero-shear-rate limit of the kinematic viscosity of the solution ν, relative to the kinematic viscosity of the solvent ν_s.

Finally $f(tr\mathbf{A})$ is the nonlinear spring law which could take a variety of forms, but is assumed in the Chilcott-Rallison model to have the so-called Warner form

$$f(tr\mathbf{A}) = \frac{1}{1 - trA/L^2} \qquad (2.4)$$

Here tr**A** represents the ensemble average of the linear dimension of the polymer chain scaled with the equilibrium radius of gyration, while L is the dimensionless contour length again scaled with the equilibrium radius of gyration.

Thus, for a given geometric configuration the problem is completely characterized by the following four dimensionless parameters: Re, De, c and L, which appear in equations (2.1)-(2.4).

At this point it is convenient to point out the permissible range of values of the configuration tensor **A**. Using the fact that **A** is the ensemble average of **RR**, it is obvious that the diagonal components must be positive in every coordinate system. This requires

$$\det[\mathbf{A}]>0, \tag{2.4}$$

where det[**A**] is the determinant of **A**.

CHAPTER 3

NUMERICAL METHOD

In this section the numerical method used for solving the governing equations for Newtonian and viscoelastic liquids is described. It is important to note that since the governing partial differential equations are nonlinear, an analytical solution it is not always possible to obtain, especially for complex flow geometries that are of interest in the industrial applications of viscoelastic fluids. In fact, an analytical solution to these equations can be obtained only for a homogeneous flow, i.e. where the velocity filed is constant and thus the constitutive equation de-couples from the momentum equation. Therefore, for solving problems of practical interest we must solve these three governing equations numerically.

A detailed description of the algorithm used in this work can be found in Singh and Leal [59]. The two main ideas of the algorithm are; the first is a third order upwind scheme (see Tabata and Fujima [63]) to discretize the convection term in the FENE dumbbell model. The second idea is a time dependent solution algorithm that explicitly forces the principal values of the configuration tensor to be positive definite. The resulting numerical method is stable and allows us to solve viscoelastic flow problems at relatively large Deborah numbers.

A steady state solution, when such a solution exists, is obtained by solving the time dependent algorithm to steady state. When a steady solution to the problem does not exists the numerical solutions evolves with time for all times.

It is desired to solve time-dependent flow problems with given initial and boundary conditions. In general, the boundary, Γ, can be divided in two parts:

$$\Gamma = \Gamma o \cup \Gamma_N$$

where Γ_N is the part of the boundary on which a traction condition is to be applied, and Γo is the part of the boundary on which the velocity is prescribed.

Equation (2.1) and (2.2) must be solved subject to initial conditions

$$\begin{aligned} u(x, 0) &= u_o(x), \\ A(x, 0) &= I \end{aligned} \tag{3.1}$$

and the boundary conditions

$$\begin{aligned} u &= g_o \quad \text{on } \Gamma_o, \\ \upsilon_s \frac{\partial u}{\partial n} - np + T \cdot n &= g_N \quad \text{on } \Gamma_N, \end{aligned} \tag{3.2}$$

where $\mathbf{g}_N$ is the traction vector on Γ_N, plus appropriate boundary condition for **A**.

The function spaces for the finite-element method are defined to be:

$$\boldsymbol{U} = \{\mathbf{u} \in \boldsymbol{H}^1(\Omega)^2; \mathbf{u} = \mathbf{g}_o \text{ on } \Gamma_o\},$$

$$\mathbf{V} = \{\mathbf{v} \in \boldsymbol{H}^1(\Omega); \mathbf{v} = 0 \text{ on } \Gamma_o\},$$

$$\mathbf{S} = \{\mathbf{s} / \mathbf{s} \in \boldsymbol{L}^2(\Omega)\}.$$

After multiplying (2.1) by the weighting funtions $\mathbf{v} \in \mathbf{V}$ and (2.2) by $\mathbf{s} \in \boldsymbol{L}^2$, and integrating by parts the following variational formulation for the steady-state case is obtained:

$$\begin{aligned} \upsilon_s \int_\Omega \nabla \mathbf{u} \cdot \nabla \mathbf{v} dx + \int_\Omega \mathbf{v} \cdot (\mathbf{u} \cdot \nabla)\mathbf{u} dx - \int_\Omega p \, \mathrm{div} \mathbf{v} dx + \int_\Omega \mathbf{v} \cdot (\nabla \cdot \mathbf{T}) dx &= \int_{\Gamma_N} \mathbf{v} \cdot \mathbf{g}_N ds \quad \text{for all } \mathbf{v} \in \mathbf{V}, \\ \int_\Omega q \, \mathrm{div} \mathbf{u} \, dx = 0 \quad \text{for all } q \in \boldsymbol{L}^2(\Omega), & \end{aligned} \tag{3.3}$$

$$\int_\Omega \mathbf{s} \cdot (\mathbf{u} \cdot \nabla)\mathbf{A} dx - \int_\Omega \mathbf{s} \cdot (\mathbf{A} \cdot \nabla \mathbf{u} + \nabla \mathbf{u}^T \cdot \mathbf{A}) dx + \int_\Omega \frac{f(\mathrm{Tr}\mathbf{A})}{\mathrm{De}} \mathbf{s} \cdot (\mathbf{A} - \mathbf{I}) dx = 0 \quad \text{for all } \mathbf{s} \in \boldsymbol{L}^2(\Omega).$$

The numerical solution of the above equations is difficult because of the nonlinear term $(\mathbf{u}\cdot\nabla)\mathbf{u}$ in the momentum equation, the incompressibility condition associated with the momentum equation, and the convection term $\mathbf{u}\cdot\nabla\mathbf{A}$ in the constitutive equations.

The first two of these complications are coupled (i.e., appear simultaneously) in the momentum equation, but can be de-coupled by using an operator-splitting technique (see Bristeau *et al.*[8]), which requires the solution of three fractional time-step problems for each complete time step. The same fractional time steps are used for the FENE dumbbell equation which gives a second-order accurate scheme in time for both the velocity and the configuration fields. The method is described for the finite-difference semidiscretization (i.e., only the time derivatives are discretized) of the problem in time (step Δt). First, the velocity and stress fields are initialized by describing

$$u^{o} = u_{o},$$

$$A^{o} = A_{o}.$$

For a start-up problem, $\mathbf{u}_{o} = 0$ and $\mathbf{A}_{o} = \mathbf{I}$, where $\mathbf{I}$ is the identity tensor. For n=1, 2, …., it is obtained $(\mathbf{u}^{n}, p^{n}, \mathbf{A}^{n})$ from $(\mathbf{u}^{n-1}, p^{n-1}, \mathbf{A}^{n-1})$ in the fractional time steps $\theta\Delta t$, $(1-2\theta)\Delta t$, and $\theta\Delta t$, where $0 < \theta < 0.5$ is picked to obtain a second-order accurate scheme. The intermediate time variables $(\mathbf{u}^{n+\theta}, \mathbf{A}^{n+\theta})$ and $(\mathbf{u}^{n+1-\theta}, \mathbf{A}^{n+1-\theta})$ are defined via the following discretized equations. The operator $\nu\nabla\underline{\mathbf{u}}$ is split into two parts by multiplying by $\zeta+\xi$, where $\zeta+\xi=1$. If it is assumed that $\zeta=(1-2\theta)/(1-\theta)$ and $\xi=\theta/(1-\theta)$, then the matrices of the time derivative and diffusion terms are the same at each time step.

Step 1.

$$\frac{\mathbf{u}^{n+\theta}-\mathbf{u}^{n}}{\theta\Delta t}-\zeta v\Delta\mathbf{u}^{n+\theta}+\nabla p^{n+\theta}=(\xi\mathbf{v}-c\upsilon_{s})\Delta\mathbf{u}^{n}-(\mathbf{u}^{n}\cdot\nabla)\mathbf{u}^{n}+\mathbf{v}\nabla\cdot\mathbf{T}^{n},$$

$$\mathrm{div}(\mathbf{u}^{n+\theta})=0, \tag{3.4a}$$

$$\frac{\mathbf{A}^{n+\theta}-\mathbf{A}^{n}}{\theta\Delta t}+\zeta\left[\frac{f(R^{n+\theta})}{De}\mathbf{A}^{n+\theta}-\mathbf{A}^{n+\theta}\cdot\nabla\mathbf{u}^{u+\theta}-(\nabla\mathbf{u}^{u+\theta})^{T}\cdot\mathbf{A}^{n+\theta}\right] \text{ where R= Tr } \mathbf{A}$$

$$=\xi\left[\frac{f(R^{n})}{De}\mathbf{A}^{n}-\mathbf{A}^{n}\cdot\nabla\mathbf{u}^{u}-(\nabla\mathbf{u}^{u})^{T}\cdot\mathbf{A}^{n}\right]-\left[\mathbf{u}^{n}\cdot\nabla\mathbf{A}^{n}\right]_{3}+\frac{f(R^{n+\theta})}{De}\mathbf{I},$$

where $\mathbf{u}^{n+\theta}$ satisfies boundary conditions (3.2) on Γ.

Step 2.

$$\frac{\mathbf{u}^{n+1-\theta}-\mathbf{u}^{n+\theta}}{(1-2\theta)\Delta t}-\xi v\Delta\mathbf{u}^{n+1-\theta}+(\mathbf{u}^{n+1-\theta}\cdot\nabla)\mathbf{u}^{n+1-\theta}=(\zeta\mathbf{v}-c\upsilon_{s})\Delta\mathbf{u}^{n+\theta}-\nabla p^{n+\theta}+\mathbf{v}\nabla\cdot\mathbf{T}^{n+\theta},$$

$$\frac{\mathbf{A}^{n+1-\theta}-\mathbf{A}^{n+\theta}}{\theta\Delta t}+\xi\left[\frac{f(R^{n+1-\theta})}{De}\mathbf{A}^{n+1-\theta}-\mathbf{A}^{n+1-\theta}\cdot\nabla\mathbf{u}^{u+1-\theta}-(\nabla\mathbf{u}^{u+1-\theta})^{T}\cdot\mathbf{A}^{n+1-\theta}\right] \tag{3.4b}$$

$$=\zeta\left[\frac{f(R^{n+\theta})}{De}\mathbf{A}^{n+\theta}-\mathbf{A}^{n+\theta}\cdot\nabla\mathbf{u}^{u+\theta}-(\nabla\mathbf{u}^{u+\theta})^{T}\cdot\mathbf{A}^{n+\theta}\right]-\left[\mathbf{u}^{n+\theta}\cdot\nabla\mathbf{A}^{n+\theta}\right]_{3}+\frac{f(R^{n+\theta})}{De}\mathbf{I},$$

where $\mathbf{u}^{n+1-\theta}$ satisfies boundary conditions (3.2) on Γ.

Step 3.

$$\frac{\mathbf{u}^{n+1}-\mathbf{u}^{n+1-\theta}}{\theta\Delta t}-\zeta v\Delta\mathbf{u}^{n+1}+\nabla p^{n+1}=(\xi\mathbf{v}-c\upsilon_{s})\Delta\mathbf{u}^{n+1-\theta}-(\mathbf{u}^{n+1-\theta}\cdot\nabla)\mathbf{u}^{n+1-\theta}+\mathbf{v}\nabla\cdot\mathbf{T}^{n+1-\theta},$$

$$\mathrm{div}(\mathbf{u}^{n+1})=0, \tag{3.4c}$$

$$\frac{\mathbf{A}^{n+1}-\mathbf{A}^{n+1-\theta}}{(1-\theta)\Delta t}+\xi\left[\frac{f(R^{n+1})}{De}\mathbf{A}^{n+1}-\mathbf{A}^{n+1}\cdot\nabla\mathbf{u}^{u+1}-(\nabla\mathbf{u}^{u+1})^{T}\cdot\mathbf{A}^{n+1}\right]$$

$$= \zeta\left[\frac{f(R^{n+1-\theta})}{De}\mathbf{A}^{n+\theta} - \mathbf{A}^{n+1-\theta}\cdot\nabla\mathbf{u}^{u+1-\theta} - (\nabla\mathbf{u}^{u+1-\theta})^{T}\cdot\mathbf{A}^{n+1-\theta}\right] - \left[\mathbf{u}^{n+1-\theta}\cdot\nabla\mathbf{A}^{n+1-\theta}\right]_3 + \frac{f(R^{n+1-\theta})}{De}\mathbf{I},$$

where $\mathbf{u}^{n+1}$ satisfies boundary conditions (3.2) on Γ.

The above scheme has the following properties:

1. By using the operator-splitting method the non-linearity and incompressibility in the momentum equation are decoupled.
2. Steps 1 and 3 for the momentum equation are reduced to Stokes-like problems (see Bristeau *et al.* [8] for the details).
3. Step 2 for the momentum equation is a nonlinear problem, but with no incompressibility condition attached.
4. For a linear model problem, it can be shown that if $\theta = 1 - 1/\sqrt{2} = 0.29289$, then the scheme is second-order accurate and unconditionally stable.
5. It may be noted that in the present implementation of this scheme the coupled nonlinear equations (3.4a-c) are solved using the Newton's method.
6. The convection term, $\left[\mathbf{u}^{n_i}\cdot\nabla\mathbf{A}^{n_i}\right]_3$, in (3.4a-c) represents the third-order upwind approximation of $\mathbf{u}\cdot\nabla\mathbf{A}$ proposed by Tabata and Fujima [63] (also Glowinski and Pironeau [19]). In this approximation $\mathbf{u}\cdot\nabla\mathbf{A}(\mathbf{x}^0)$ is approximated using the known values $\mathbf{A}$ at the following five points: $\mathbf{x}^{-2}$, $\mathbf{x}^{-1}$, $\mathbf{x}^0$, $\mathbf{x}^1$, $\mathbf{x}^2$, see Figure 3.1. These five points lie on the line that is parallel to $\mathbf{u}$ and passes through $\mathbf{x}^0$, $\mathbf{x}^{-1}$, $\mathbf{x}^{-2}$ are on the upstream side of $\mathbf{x}^0$, and $\mathbf{x}^1$, $\mathbf{x}^2$ are on the downstream side of $\mathbf{x}^0$. Let $\xi^i = |\mathbf{x}^i - \mathbf{x}^0|/h$, where $h = |\mathbf{x}^{-1} - x^0|$, then

$$\left|u^{n_i}\cdot\nabla A^{n_i}\right|_3 = |\mathbf{u}(\mathbf{x}^0)|\sum_i \frac{\tau_i A(\mathbf{x}^i)}{h},$$

where

$$\tau_i = \frac{\prod_{i\neq 0,j}(\xi^0 - \xi^j + \alpha)}{\prod_{i\neq j}(\xi^i - \xi^j)}, \qquad i\neq 0,$$

$$\tau_0 = -\sum_{i\neq 0}\tau_i$$

It is easy to show that

$$[u\cdot\nabla A]_3 = \mathbf{u}\cdot\nabla A + \alpha\frac{h^3}{4!}\frac{\partial^4 A}{\partial\xi^4} + O(h^4).$$

For α =0, the above approximation is centered and fourth-order accurate. On the other hand, if α >0, then it is third-order accurate and upwinded. The degree of upwinding in this scheme is controlled by α.

In the above formulation the convection term is treated explicitly (i.e., as an inhomogeneous forcing term) irrespective of its sign and thus would allow the configuration tensor to become negative, therefore there would a new algorithm that treats the convection term explicitly or implicitly depending on its sign. This new algorithm is guaranteed to preserve the nonnegative definiteness of the configuration tensor.

The solution domain is discretized using the pseudo P_2 - P_1 - P_2 elements. By using the pseudo P_2 elements it is obtained matrices that have a bandwidth of about one-half of the regular P_2 elements. This leads to a considerable savings in inverting matrices. Of course, there is some loss in spatial resolution which could be compensated for by increasing the number of nodes. Let τ_h denote the triangulation of $\bar{\Omega}$. Each triangle is

further subdivided into four triangles by joining the midpoints of each side, see Figure 3.1. Let τ_k be the set of four subtriangles of $K \in \tau_h$. Then the pressure, p, is in the space

$$Q_h = \{q_h \in \mathbf{L}^2(\Omega);\ q_{h|k} \in P_1,\ \forall K \in \tau_h\},$$

the discrete velocity space, U_h is defined as

$$U_h = W_h \cap U,$$

where $W_h = \{\mathbf{w}_h \in C^0(\Omega)^2;\ \mathbf{w}_{h|k} \in P_1,\ \forall K' \in \tau_k,\ \forall K \in \tau_h\}$, and the configuration tensor, $\boldsymbol{A}$, is in the space $S_h = \{\mathbf{s}_h \in \mathbf{L}^2(\Omega);\ \mathbf{s}_{h|k} \in P_1,\ \forall K' \in \tau_k\ \forall K \in \tau_h\}$.

The weighting-functions are in the space

$$V_h = W_h \cap V.$$

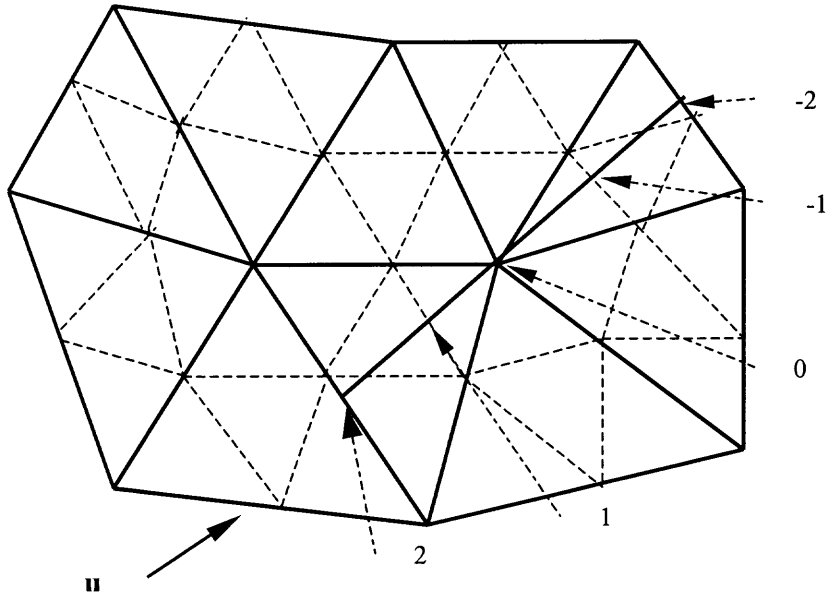

Figure 3.1 A schematic of the points used for approximating the convection term in the FENE model.

CHAPTER 4

PERMEABILITY OF PERIODIC POROUS MEDIA

4.1 Abstract

The permeability of the two-dimensional periodic arrays of cylinders is obtained numerically as a function of the dimensionless wave number kD, where k is the wave number based on the distance between particles in the stream-wise direction and D is the diameter. To isolate the kD dependence, the diameter D and the porosity are held fixed. The latter is achieved by making the product of distance between particles in the cross-stream and stream-wise directions constant. The numerical results show that the permeability increases with kD, but the increase is not monotonic. In particular, the permeability decreases for $\sim 5 < kD < \sim 7.7$, and becomes locally minimum at $kD \approx 7.7$. This value of kD is significant because it is the smallest wave number for which the stream-wise area-fraction spectrum is zero. For $kD < 5$ and $7.7 < kD < 11$, the permeability increases with kD. Numerical simulations also show that for $kD \approx 7.7$ the pressure distribution in the cross-stream direction is relatively flat which again is a consequence of the fact that the area-fraction distribution in the flow direction is approximately constant.

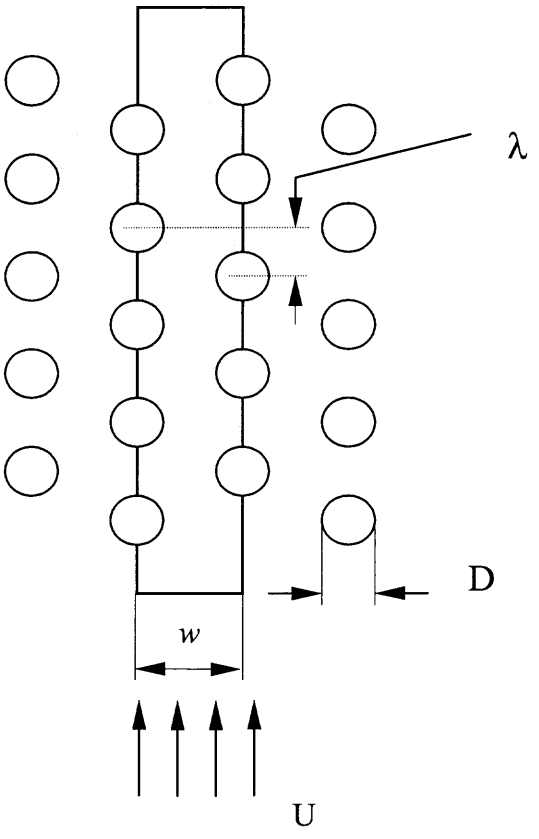

Figure. 4.1a A schematic of a periodic array of cylinder is shown. The interparticle distance in the z direction is λ and in the cross-stream direction is *w*. The shaded area is a typical computational domain for our simulations

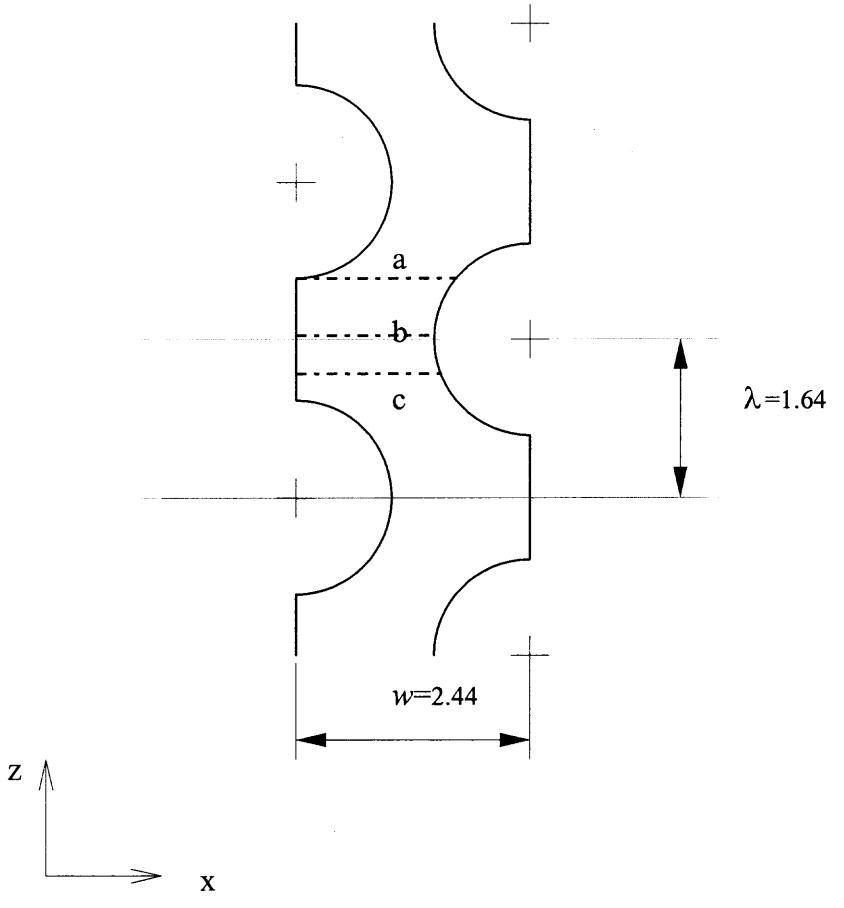

Figure 4.1b The porous medium for $\lambda = 1.64$.

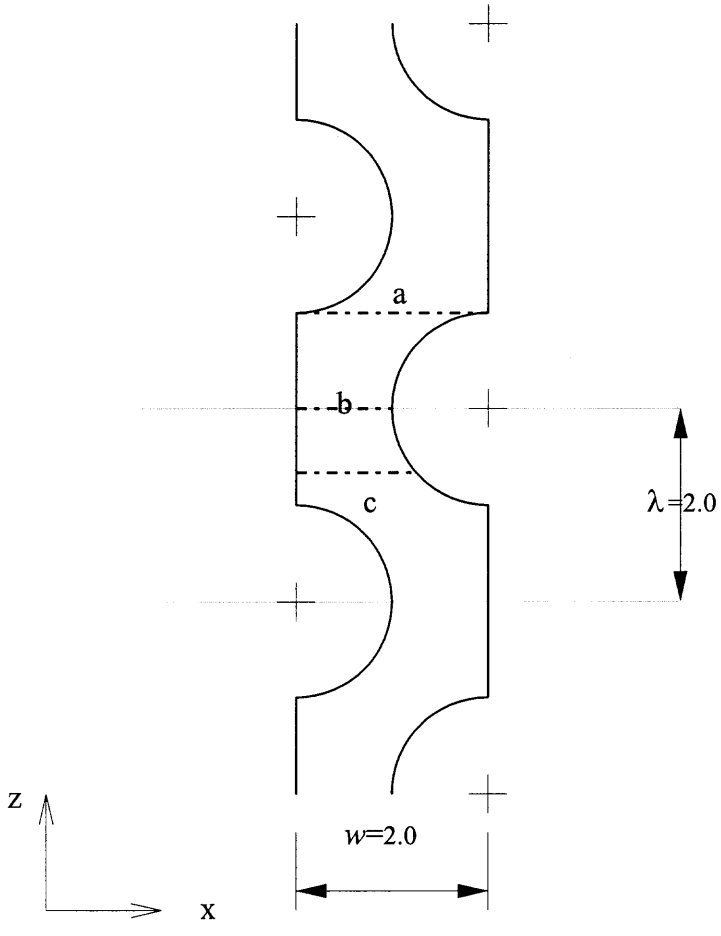

Figure 4.1c The porous medium for $\lambda = 2$.

4.2 Introduction

The direct numerical simulation capability for investigating the porous media flows is important in a number of applications. The objectives in these applications may range from determining the flow field for the given velocity and pressure boundary conditions to designing a porous medium with the desired flow properties.

An example of the former is the direct numerical simulation of underground flows in the oil recovery applications. Examples of the latter include many applications where the objective is to design the optimal porous medium geometry for trapping or absorbing fluids.

It is noteworthy that even though the flow field in a porous medium varies at the length scales comparable to the size of particles, in many applications a detailed knowledge of these particle scale variations is not required. Instead, an averaged macroscopic response is sufficient. A detailed knowledge of the particle scale variations, however, can be helpful in designing the optimal porous medium for specialized applications.

A macro scale model such as Darcy's law is extremely useful because it allows us to predict the macroscopic flow field without solving the detailed fluid flow problem, Darcy's law states that the volume averaged superficial fluid velocity U is proportional to the pressure gradient:

$$U = \kappa . \frac{\nabla p}{\mu}, \qquad (4.1\text{-}1)$$

where μ is the viscosity, p is the pressure and κ is the effective permeability tensor for the medium. The permeability tensor κ for a medium depends on several factors, including the porosity and the particle size distribution. Several correlation have been developed to

relate the permeability of a porous medium to these distributions, (see (7), (16), (23) and (25)).

The permeability of a porous medium also depends on the microstructure or the relative arrangement of particles. In fact, analysis based on Darcy's law works well only when the assumptions used for driving it are valid; i.e., the medium is random, completely wet (the surface tension effects are not present), and the fluid is Newtonian (7), (26), (40) and (53). A porous medium, in general, may not be random, but can have a distinct microstructure, i.e., the particle arrangement contains a preferred direction for the flowing fluid. This may be the case when the particles are arranged in a systematic pattern, as is the case for many man-made porous materials. To apply Darcy's law in such cases, the macroscopic permeability should be determined by accounting for the microstructure, (32) and (45).

It is possible to numerically estimate the macroscopic permeability of a micro structured porous medium by including its key micro structural features into the computational domain. There are several direct numerical studies where the permeability of a collection of periodically arranged particles is determined numerically (see (25) and (69)). For example, it was shown in (69) that the permeability of the face centered cubic (FCC), body centered cubic (BCC) and simple cubic (SC) lattices of spheres—with the same porosity and D—are different. In other words, the arrangement of particles relative to the flow direction is important in determining the permeability.

In this research, the dependence of permeability on the microstructure is studied by continuously varying kD (or the area-fraction distribution) along the flow direction for a two-dimensional porous medium. Our simulations show that for a given porosity and

particle size, the permeability depends on the wavelength λ or the distance between the particles in the flow direction (see Figure 4.1a). The diameter D and λ can be used to define a dimensionless wave number kD for the porous medium, where $k=2\pi/\lambda$. For small kD, the permeability increases with increasing kD, but this increase is not monotonic. The permeability starts to decrease at $kD\approx5$ and reaches a local minimum at $kD\approx7.7$. As it will be discussed in the next section, the kD value at this local minimum of permeability is significant because it is the smallest dimensionless wave number for which the area fraction spectrum is zero. Thus, the changes in permeability and area-fraction distribution with kD are related.

4.3 Permeability and Area Fraction Distribution of Periodic Porous Medium

In this study, it will be assumed that the particles (or cylinders) are arranged periodically in the space as shown in Figure 4.1a. Therefore, away from the entrance and the exit the velocity field is periodic, and the pressure drop for each period cell is constant. This constant pressure drop for a period cell determines the permeability of the porous medium.

A typical computational domain used in our simulations is shown in Figure 4.1b. The domain is specified in terms of two parameters: the distance λ used for arranging particles in the flow direction and the width w. To ensure that the solids fraction $\frac{0.5\pi R^2}{\lambda w}$ is constant, the product λw was held fixed at 4 and the particles radius R=1. Thus, the solids fraction for our simulations is 0.393.

To define the area-fraction on the planes perpendicular to the flow direction—assumed here to be the z-axis of the coordinate system—we will assume that the particles are cylinders of radius R. The number density distribution is denoted by N(z). Let the area-fraction $\phi_a(z)$ be the fraction of the plane z covered by the particles. The following expression for ϕ_a can be obtained by adding the areas of intersections of N(z+x) particles that have centers at a distance x from the plane z

$$\phi_a(z) = \int_{-D/2}^{D/2} N(x+z)\, 2\sqrt{\frac{D^2}{4} - x^2}\, dx \quad . \tag{4.1}$$

Note that the integration limits are from -D/2 to D/2, as only the particles that are at a distance less than R from the plane z have a non-zero area of intersection (see (56) where the area-fraction was obtained for the spherical particles).

Assuming that N(z) is in the Fourier transform class, the Fourier transform of the above expression can be obtained using the convolution-multiplication theorem

$$\phi_a(k) = D^2\, \Theta(kD)\, N(k) \tag{4.2}$$

where k is the wave number, $\Theta(kD) = \int_{-1/2}^{1/2} 2\sqrt{\frac{1}{4} - x^2}\, e^{ikDx}\, dx$ is the blockage function, $\phi_a(k)$ is the Fourier transform of $\phi_a(z)$ and N(k) is the Fourier transform of N(z). The graph of $\Theta(kD)$ is shown in Figure 4.2. From this figure we note that the set of zeros of $\Theta(kD)$ is: kD= 7.663, 14.031, 20.347, ... Expression (4.2), therefore, implies that the dimensionless wave numbers, kD, for which $\Theta(kD)$ is zero, are blocked, i.e., are missing in the spectrum of the area-fraction.

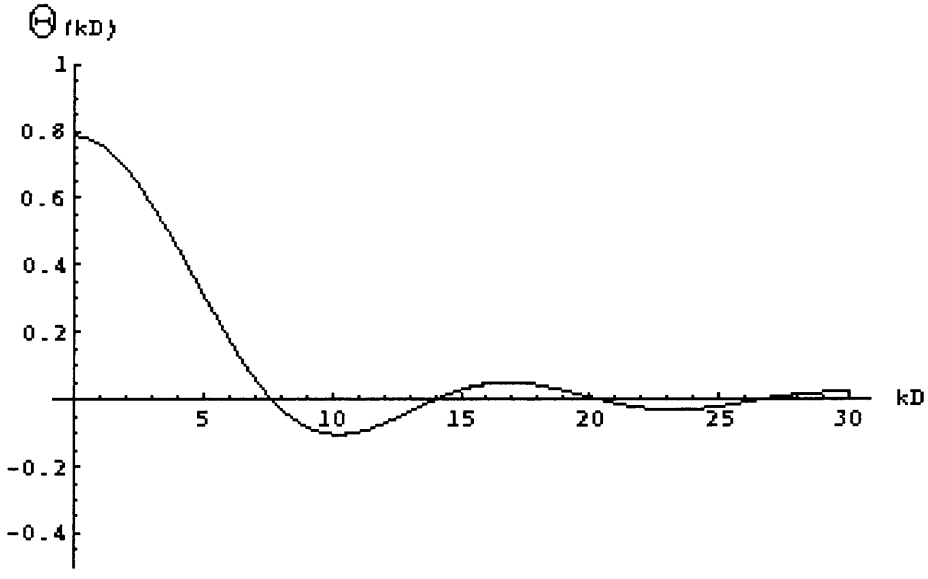

Figure 4.2 Θ(kD) is plotted as a function of kD

To understand the physical significance of $\Theta(kD)$ we note that if N(k) is non-zero only for the wave numbers for which $\Theta(kD)$ is zero, the area available to the flowing fluid in the z-direction will be constant, as in this case $\phi_a(k)=0$ for all $k>0$. On the other hand, if $\Theta(kD)$ is nonzero for $N(k)\neq 0$, the area-fraction will vary with z. For example, for the periodic porous medium shown in Figure 4.1b, $N(k) = \sum_n \delta(k - \frac{2\pi n}{\lambda})$, where n is an integer and $\lambda/R=2\pi/kR=1.64$ is the distance between particles in the flow direction. In this case, for the first non-zero mode of N(k), i.e. kD=7.66, $\Theta(kD)$ is zero, and thus this mode does not cause any variation in the area available to the fluid. The area fraction—i.e., the convolution of (4.1)—is, however, not exactly constant because only the first zero of $\Theta(kD)$ coincides with the first non-zero term of N(k). For the higher order modes of N(k), $\Theta(kD)$ is non-zero. But, since $\Theta(kD)$ is small for the higher order modes of N(k), the area-fraction varies—but only slightly—with z. For $\lambda=2$ (kD=6.28), on the other hand, since $\Theta(6.28)\neq 0$, the area-fraction varies substantially with z (see Figure 4.1c).

It is noteworthy that for the SC, FCC and BCC lattices with the same porosity, the kD value along the flow direction is different. For example, when the solids fraction is 0.45 the kD values for the SC, FCC and BCC lattices are 5.97, 6.98 and 9.48, respectively. As noted before, the past numerical studies show that the permeability of the SC lattice is smaller than that of the FCC lattice, but the permeability of the FCC lattice is larger than that of the BCC lattice (32) and (44). Thus, the permeability changes non-monotonically with kD. The permeability for other values of kD is not known, as in these studies only the above three cubic lattices were studied. This non-monotonic

variation of permeability for spherical particles is interesting, and needs further investigation.

4.4 Problem Statement and Boundary Conditions

The objective of this research is to numerically simulate the periodic porous media flows, and use the simulation results both for estimating the effective permeability and for understanding the micro-scale flow features. The Navier-Stokes and continuity equations are solved using the finite-element method in the periodic computational domains using the boundary conditions described below. The Reynolds number is assumed to be zero. The details of the numerical method are given in (55).

The following boundary conditions are applied at the boundaries of computational domain: At the inlet of the computational domain the incoming superficial velocity U is specified. Along the sides of the computational domain periodic boundary conditions, i.e., $u=0$, $\frac{\partial v}{\partial x}=0$, are applied, where u is the x-component of velocity and v is the y-component of velocity. At the exit of the computational domain the no-traction boundary condition is applied, and the no-slip boundary condition is imposed at the surface of particles.

4.5 Results and Conclusions

Figure 4.3 shows that the relationship between the incoming velocity U and the pressure drop Δp over a fixed distance is linear. In this figure the velocity U is assumed to be 1, 2, or 3. The linear relationship between U and the pressure gradient for Newtonian liquid shows that the Darcy's law is applicable for our periodic porous medium.

Figure 4.4 shows the value of pressure drop for three different mesh resolutions. The three meshes respectively contains 1143, 1669 and 3014 triangular elements and 2556, 3666 and 6479 nodes. From this figure it is clear that the pressure drop over a fixed distance is independent of the mesh resolution used. Therefore, for all calculations reported later in this dissertation the mesh with 1669 elements was used.

For the simulation the permeability κ along the z-direction is calculated by using the definition of Darcy's Law:

$$\kappa = \frac{\mu U}{\frac{\Delta p}{\lambda}} \tag{4.3}$$

where Δp is the pressure drop over the distance λ, μ is the viscosity and U is the superficial velocity. As noted before, for the simulations the porosity is 0.607, and the viscosity and the superficial velocity are held fixed.

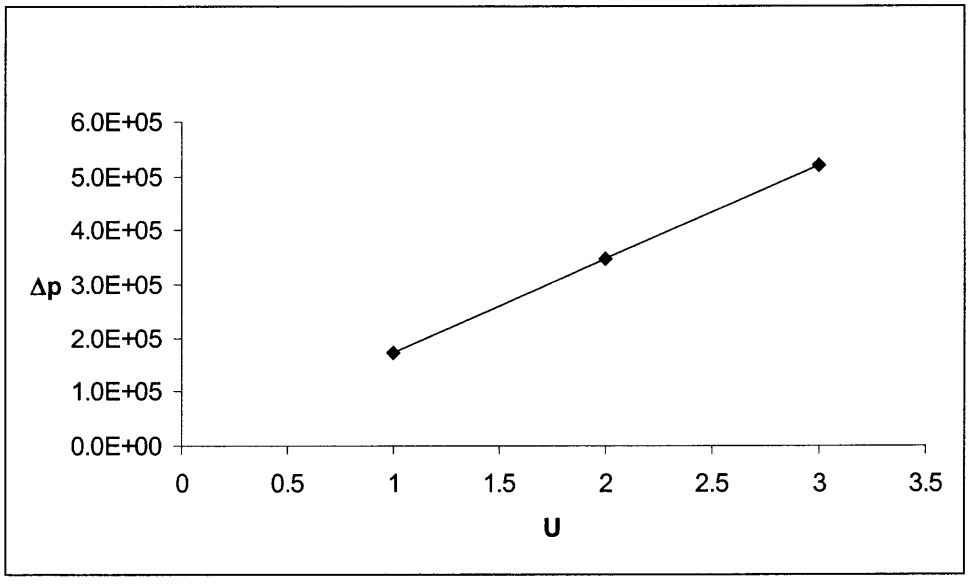

Figure 4.3 The pressure drop Δp over a distance of 29.92 is plotted as a function of the superficial velocity U for w= 2.25. The linear relationship shows that the Darcy's law is valid and the permeability is 2.88E-3.

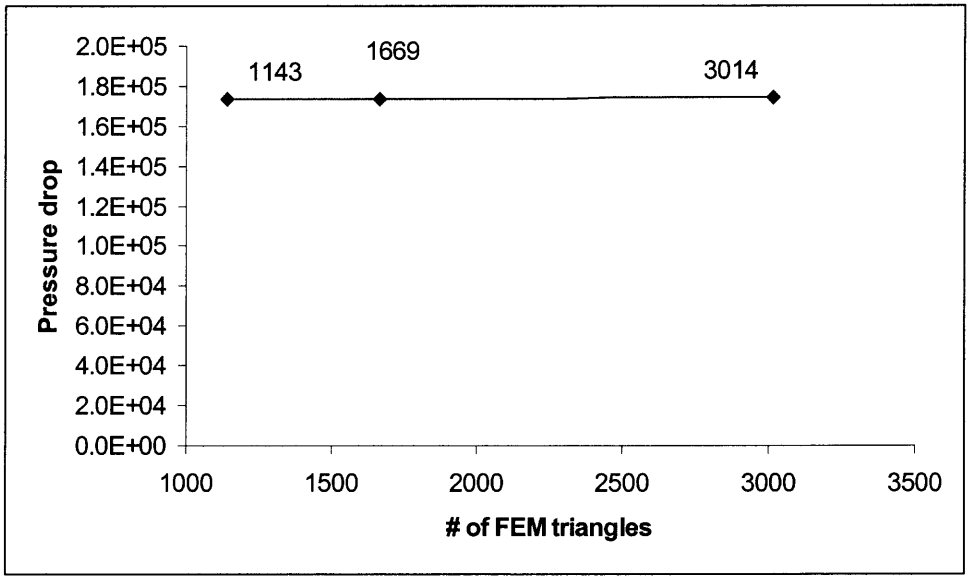

Figure 4.4 The pressure drop over a fixed distance of 29.92 is plotted for three different mesh resolution containing 1143, 1669, and 3014 triangles. U=2, w=2.25. These results show that the pressure drop is independent of mesh resolution.

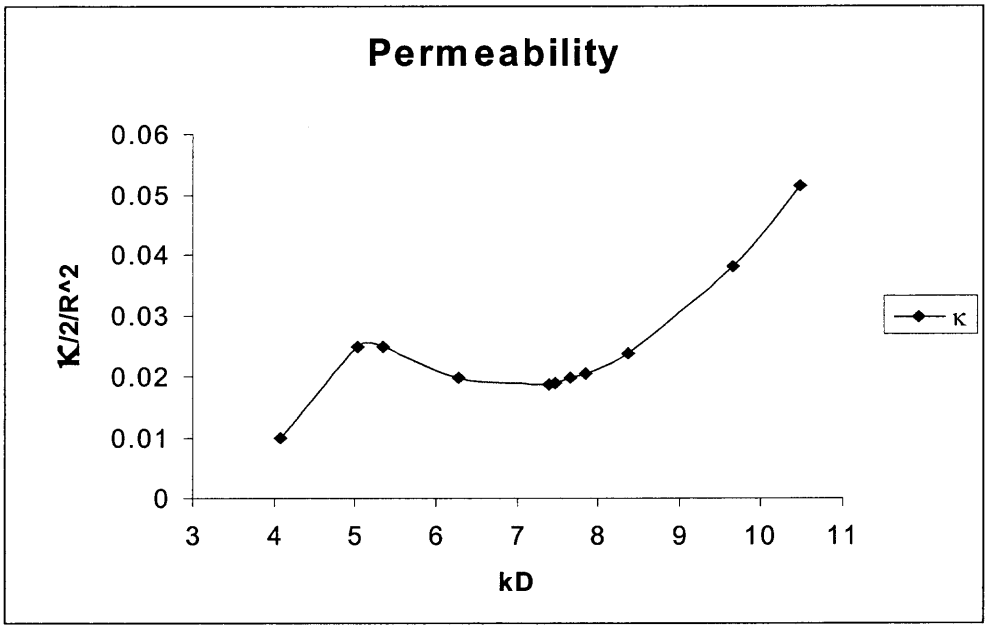

Figure 4.5 Numerically computed permeability $\kappa/2/R^2$ is shown as a function of kD

It is noticed that the permeability of a channel of width w varies as w^2. Since for the simulations $\lambda w=4$ and the wave number k is inversely related to λ, the width of an equivalent flat channel increases with kD. The computed values of the permeability are shown in Figure 4.5 as a function of the dimensionless wave number kD. From this figure, it can be stated that for $kD<5$, as expected, the permeability increases with increasing kD. But, for $5<kD<7.7$ the permeability decreases with kD. The permeability reaches a local minimum at $kD\approx7.7$. After reaching this local minimum, the permeability increases with increasing kD. The calculations were carried out for kD up to 11. Note that for $kD\approx7.7$, $\Theta(7.7)\approx0$, i.e., this value of kD is missing in the area-fraction spectrum (see section 4.3). This shows that the area-fraction distribution along the flow direction plays a role in determining the permeability.

Another interesting feature for $kD=7.7$ is that the pressure distribution in the cross-stream direction is relatively flat (see Figure 4.6a). For $kD=6.28$, on the other hand, the pressure varies substantially in the cross-stream direction (see Figure 4.6b). This again is related to the area-fraction variation in the flow direction. In particular, when the area-available to the flow is constant or varies relatively slowly in the stream-wise the pressure distribution in the cross-stream direction is relatively flat.

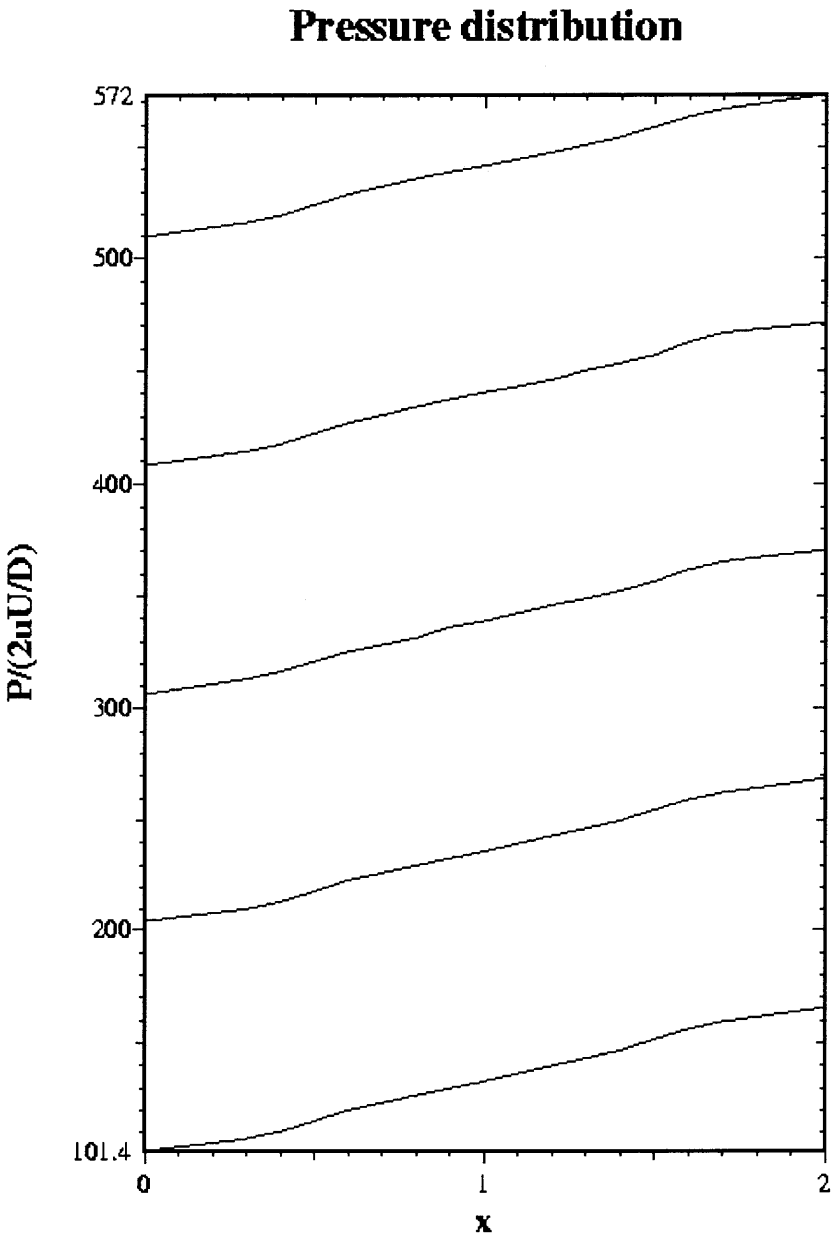

Figure 4.6a The dimensionless pressure distribution in the cross-section direction are shown at five different z locations, λ=2.0.

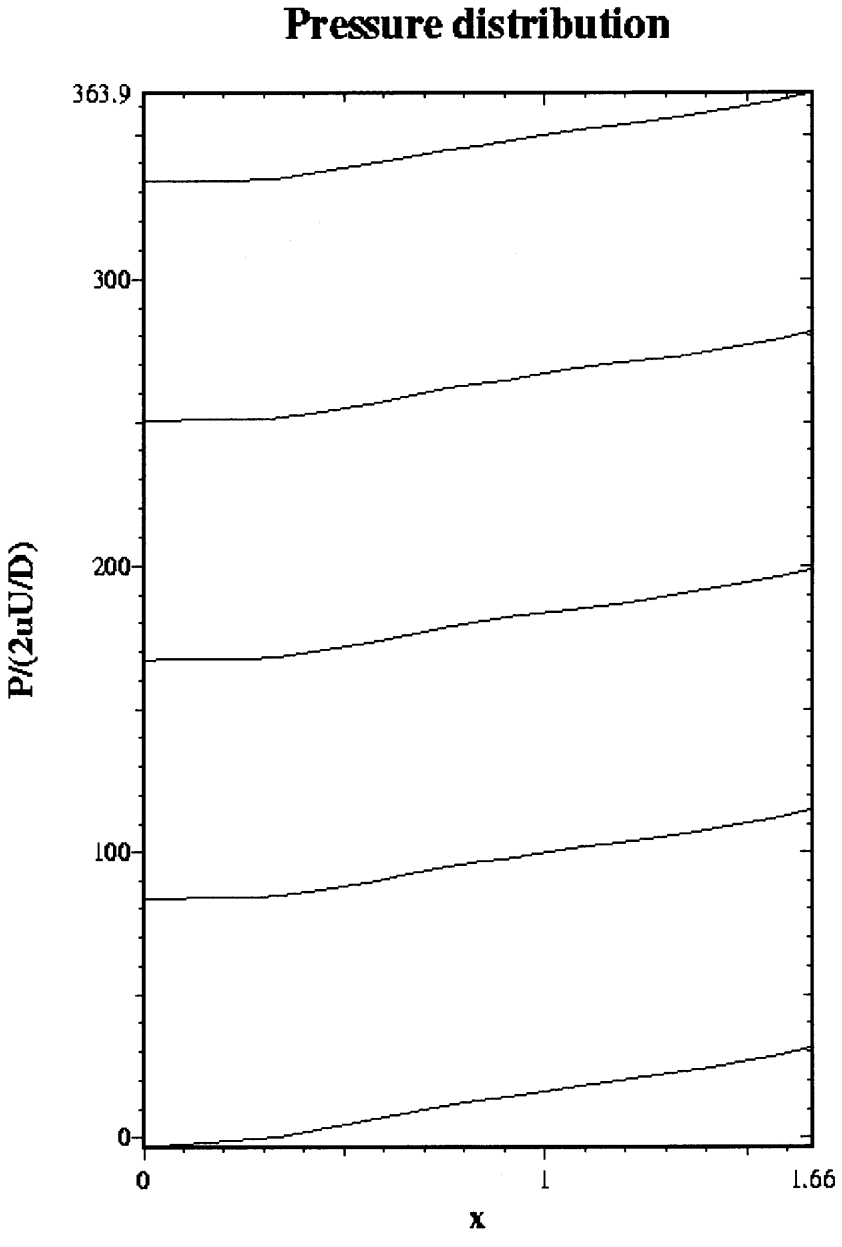

Figure 4.6b The dimensionless pressure distribution in the cross-section direction are shown at five different z locations, λ=1.64.

Finally, it may be concluded that the periodic porous medium N(k) contains higher order modes—i.e., in addition to the primary mode at $k=2\pi/\lambda$—for which $\Theta(kD)$ may not be zero. For example, even for $\lambda/R=1.64$ the area-fraction is not exactly constant in space. But, since $\Theta(kD)$ is small for the higher order modes, they lead to only small variations in the area-fraction along the stream-wise direction. Furthermore, as $\Theta(kD)$ decreases with increasing kD, the dependence of permeability on the area-fraction decreases with kD, and the permeability approaches the value for an equivalent flat channel.

CHAPTER 5

VISCOELASTIC POROUS MEDIA FLOWS

5.1 Overview

In this chapter, the motion of a viscoelastic fluid flow passing through a two-dimensional periodic porous medium is studied numerically. For this study, the porosity is held fixed at 60% and the variations of permeability, pressure-drop, and tr**A** (measurement of the elongation of the polymer molecules) distributions are investigated as a function of the wave number kD and dimensionless relaxation time De along the flow direction.

Numerical results show that the permeability for viscoelastic fluid does not change monotonically with kD, where k is the wave number, $k=2\pi/\lambda$ and λ is the distance between the particles in the flow direction and D is the diameter of particles. The local minimum of the permeability is at kD =7.7 and the local maximum is at kD=5.0. These results are similar to the results obtained earlier shown in chapter 4 for Newtonian fluids, see Alcocer, Kumar and Singh (2). It is found that the pressure drop for Newtonian flows is smaller than for viscoelastic flows, this is because for viscoelastic flows, the molecules (i.e., polymer molecules) are being stretched and consequently the resistance to the fluid flow is increased and so is the pressure-drop. It is also found that the pressure drop decreases when the De increases, for all of the cases.

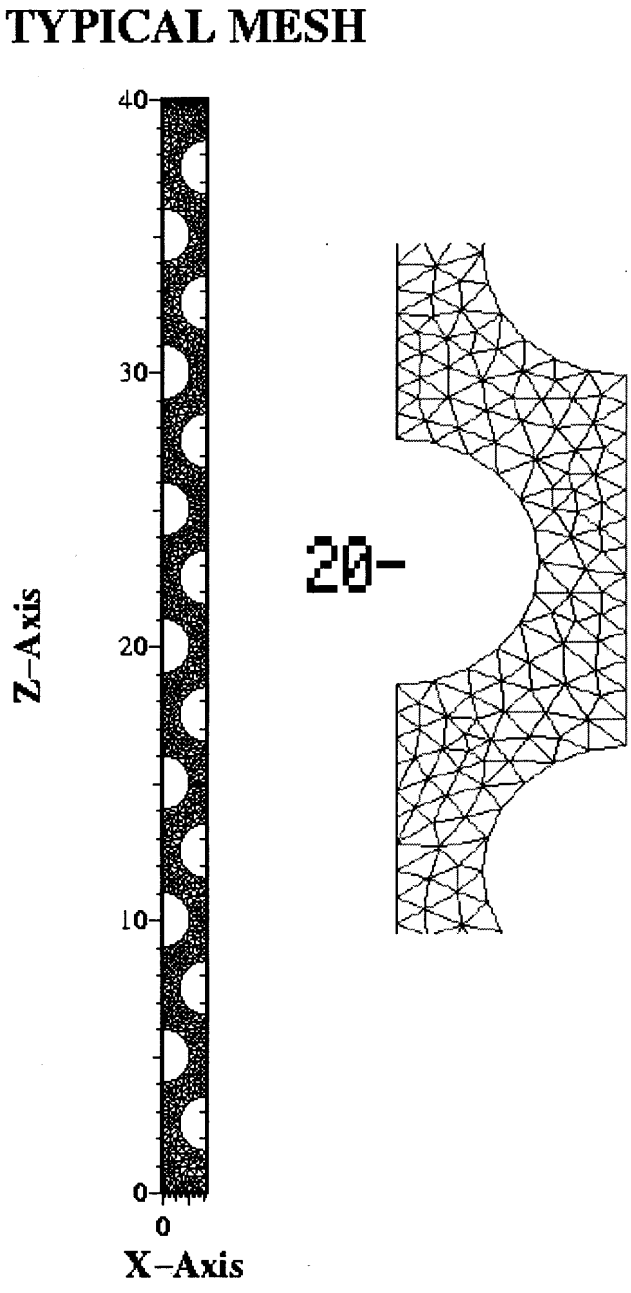

Figure 5.1 Typical mesh used in the simulation and its magnified view

5.2 Introduction

Numerical capability for simulating viscoelastic porous media flows is important because of their use in many technological applications, as well as for understanding many flows in nature.

There are many examples of porous materials encountered in everyday life and the environment. For instance, with the exception of metals, some dense rocks, and some plastics, virtually all solids and semi-solid materials are porous to varying degrees. The fluid flow through these materials has applications in many branches of engineering and science, e.g., ground water hydrology, oil recovery, reservoir engineering and soil mechanics. Textiles and leathers are highly porous; they owe their thermal insulating properties, as well as the property that they 'breathe', to their porous structure. Paper towels and tissue papers are also highly porous and their absorbency is partly due to their porous structure and partly due to the property that they are strongly wetted by water. Building materials such as bricks, concrete, limestone, sandstone and lumber are all porous. Wood can be impregnated because of its porosity. Soil is capable of performing its function of sustaining plant life only because it can hold water in its pore spaces, and plants absorb this water by the action of their capillaries.

The objective of numerical simulation of porous media may range from determining the flow field for given velocity and pressure boundary conditions to designing a porous medium with the desired flow properties. It is noteworthy that even though the flow field in a porous medium varies at length scales comparable to the size of particles, in many applications a detailed knowledge of these particle scale variations is not required. Instead, an averaged macroscopic response is sufficient. A detailed

knowledge of the particle scale variations, however, can be helpful in designing the optimal porous medium for specialized applications.

A macro scale model such as Darcy's law is extremely useful because it allows us to predict the macroscopic flow field without solving the detailed fluid flow problem. Darcy's law states that the volume averaged superficial fluid velocity U is proportional to the pressure gradient:

$$U = \boldsymbol{\kappa}.\frac{\nabla p}{\mu}$$

where μ is the viscosity, p is the pressure and $\boldsymbol{\kappa}$ is the effective permeability tensor for the medium. The permeability tensor $\boldsymbol{\kappa}$ for a medium depends on several factors, including the porosity and the particle size distribution. Several correlations have been developed to relate the porous medium permeability to these distributions, see (6), (16), (23), and (25).

The permeability of a porous medium also depends on the microstructure or the relative arrangement of particles. This dependence, however, is not completely understood because it is difficult to quantify the relationship between the microstructure and permeability—for both experiments and simulations. In fact, analysis based on Darcy's law works well only when the assumptions used for driving it are valid; i.e., the medium is random, completely wet (the surface tension effects are not present), and the fluid is Newtonian (6), (26), (53). A porous medium may not be random, but have a distinct microstructure i.e., the particle arrangement contains a preferred direction for the flowing fluid. This may be the case when the particles are arranged in a systematic pattern, as is the case for many man-made porous materials. To apply Darcy's law in such cases, macroscopic permeability should be determined by accounting for the microstructure.

It is possible to numerically estimate the macroscopic permeability of these microstructure porous media by including their key microstructural features into a computational domain that is smaller than the actual medium. There are several direct numerical studies where the permeability of a collection of periodically arranged particles is determined numerically, but it has been difficult to establish a relationship between the microstructure and the permeability, see (16), (23).

From Darcy's law we note that permeability is a measure of the ease with which a fluid passes through a porous material. For Newtonian porous media flows the permeability depends only on the pore geometry and can be shown to be independent of the properties of penetrating fluid. Several models have been developed for the permeability κ, some of them are purely empirical and some have a theoretical basis. An example of a purely empirical model is Krumbein & Monk (1943)

$$\kappa=0.617\text{e-}11d^2$$

where κ (permeability in cm^2) is related to a mean grain diameter d (in microns), see (5). There are several theoretical models that are obtained from Darcy's law. One of the most widely accepted derivations of permeability and its relationship to porous medium properties is the one proposed by Kozeny (1927) and later modified by Carman (5). The latter equation has an empirical coefficient, this is typical of a third class of formulas of permeability that are semi-empirical i.e., where the theoretical analysis using conceptual models gives a relationship between κ and various matrix parameters. The numerical coefficients, however, must be determined experimentally for each particular porous matrix or to a group of similar porous matrices.

Darcy's law, in general, is not valid for viscoelastic flows where the evolution of stress is given by the partial differential equations. But it is possible to obtain generalized models for non-Newtonian flows. For example, for the Ostwald-de Waele model,

$$\underline{\underline{\tau}} = -\left\{ m \left| \sqrt{\tfrac{1}{2}\left(\underline{\underline{D}} : \underline{\underline{D}}\right)} \right|^{n-1} \right\} \underline{\underline{D}}$$

The effective permeability μ is given by

$$\mu = m\left[\frac{2(25/12)^n\left(3+\frac{1}{n}\right)^n 3^{n+1}}{150}\right]\frac{D_p^{1-n}\varepsilon^{2(1-n)}}{(1-\varepsilon)^{1-n}}$$

Here m and n are the rheological parameters, D_p is the particle diameter, and ε is the porosity of the porous medium as determined for a Newtonian flow through the medium, $\underline{\underline{\tau}}$ is the stress tensor and $\underline{\underline{D}}$ is the symmetric part of the velocity gradient tensor. Furthermore, κ is the permeability of the medium for the Newtonian flows. Note that μ does not have the units of viscosity, for n=1, it reduces to Newton's law of viscosity with $m=\mu$; thus the deviation of n from unity indicates the degree of deviation from Newtonian behavior. For values of n less than unity the behavior is pseudoplastic, whereas for n greater than unity the behavior is dilatant.

One of the goals of this study is to understand the role of viscoelasticity in determining the pressure drop, and thus also the permeability of the medium. The role of relaxation time is quantified in terms of the dimensionless relaxation time called the Deborah number $De = \frac{\lambda U}{D}$, where λ is the relaxation time, U is the characteristic velocity and D is the particle diameter. When the Deborah number is O(1) the elastic effects may be as important as the viscous effects, and hence may lead to significant modification of the flow field.

The simulations show that for high Deborah number flows there is a strong coupling between the fluid relaxation time and the length scale associated with the porous media periodicity. To understand the coupling mechanism, viscoelastic flows will be studied in the periodic porous media (see Figure 4.1a). It will be assumed that the fluid flow in the cross-stream direction is periodic which simplifies the problem as the periodic boundary conditions can be imposed on the sides of the computational domain.

In the investigation, the finite element method is used to discretize the computational domain, and the FENE dumbbell and Oldroyd-B models to model the viscoelastic flow. In these models the stress contains two distinct contributions: one coming from the conformation of the polymer and the other coming from the viscous nature of the solvent. The solvent contribution is viscous in nature and appears as the highest-order term in the momentum equation, which makes it elliptic.

The simulations were started by first obtaining the solution of the Newtonian flow which developed instantaneously when the simulation was started. Once the Newtonian solution was obtained, then this solution was used as the starting point for the viscoelastic case. The steady state (no variations with time) viscoelastic solutions were obtained by running a time dependent code. The calculations were stopped when the pressure and velocity fields reached their respective steady state values.

5.3 Computational Domain and Boundary Conditions

A typical computational domain is shown as the shaded period cell in Figure 4.1a. The Reynolds number in the present study is assumed to be Re $=3.3\text{x}10^{-4}$ for both Newtonian and non-Newtonian flows, therefore is considered to be negligible. Thus, for a given

geometric configuration of the periodic domain, the problem is completely characterized by the three parameters:

De, c and L.

In the present work, consider the behavior predicted for a range of values for De, L=64 and c=1.0. It is obvious that c=1 represents a more concentrated solution where the presence of the polymer produces an incremental increase in the zero-shear-rate limit of the kinematics viscosity of the solution that is exactly equal to the kinematics viscosity of the solvent. It may be noted that the concentration of a specific polymer that would produce such an increment in ν (kinematics viscosity) would depend upon the molecular weight, the molecular weight distribution and the solvent, among other factors. The Deborah number can be varied over a wide range by changing the value of relaxation time, in our simulations we are using 0.02, 0.1, 0.5 and 1.0. The magnitude of the dimensionless contour length L is known to be proportional to the square root of the number of statistical sub-units in the polymer values up to O(40-50) in order to encompass polymers with molecular weights of order several million.

In the simulations there is a restriction to the case of two-dimensional periodic porous media. The domain is defined in terms of two parameters: w and λ, w is the distance between the center of the circles in a plane perpendicular to the fluid flow, and λ is the distance between the center of circles along the fluid flow direction (see Figure 4.1a). The porosity ε is defined as $\varepsilon = \frac{\pi r^2}{2w\lambda}$, and for the simulations it is held fixed at 0.6. This value of porosity is achieved by keeping the product $w\lambda$=4.0.

The role of viscoelasticity in determining the pressure drop is investigated for these different domains that have the same porosity of 60%, but have different values of

w and λ. The computational domain is discretized using the finite element method. A typical mesh with 4019 nodes is shown in Figure 5.1. In the simulations, the fluid is passing through a periodic porous medium in which the solid particles are represented by the circles. The porous medium is periodic, and the walls and surfaces have zero velocity and no-slip boundary conditions apply also, a typical computational domain can be seen in the Figure 4.1. The velocity U is known at the inlet, and for the simulations it is assumed a value of U=1.0, and traction boundary conditions are specified at the exit.

The two parameters, De and λ, determine the pressure and the tr**A** distribution in the medium. The pressure drop (see Figure 5.2) is a measure of the resistance offered by the medium to the flowing fluid. The tr**A** distribution (see Figure 5.3 and 5.4) indicates the extent to which the polymer molecules are stretched as the fluid passes through the medium. The effective permeability of the medium is also investigated as a function of the dimensionless wave number kD and De.

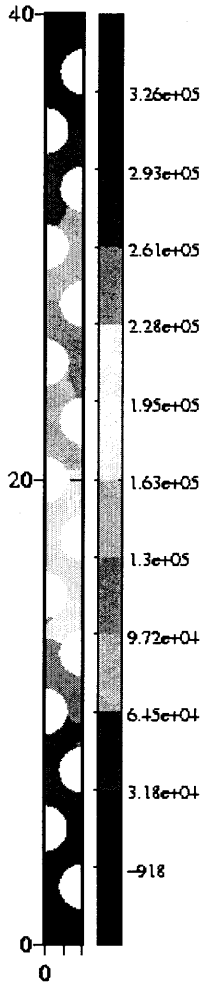

Figure 5.2 Values of pressure drop along the fluid flow

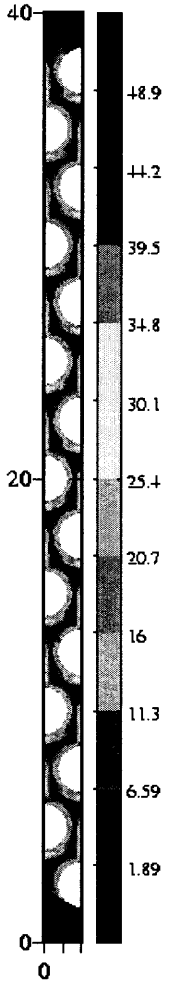

Figure 5.3 Values of trA along the fluid flow

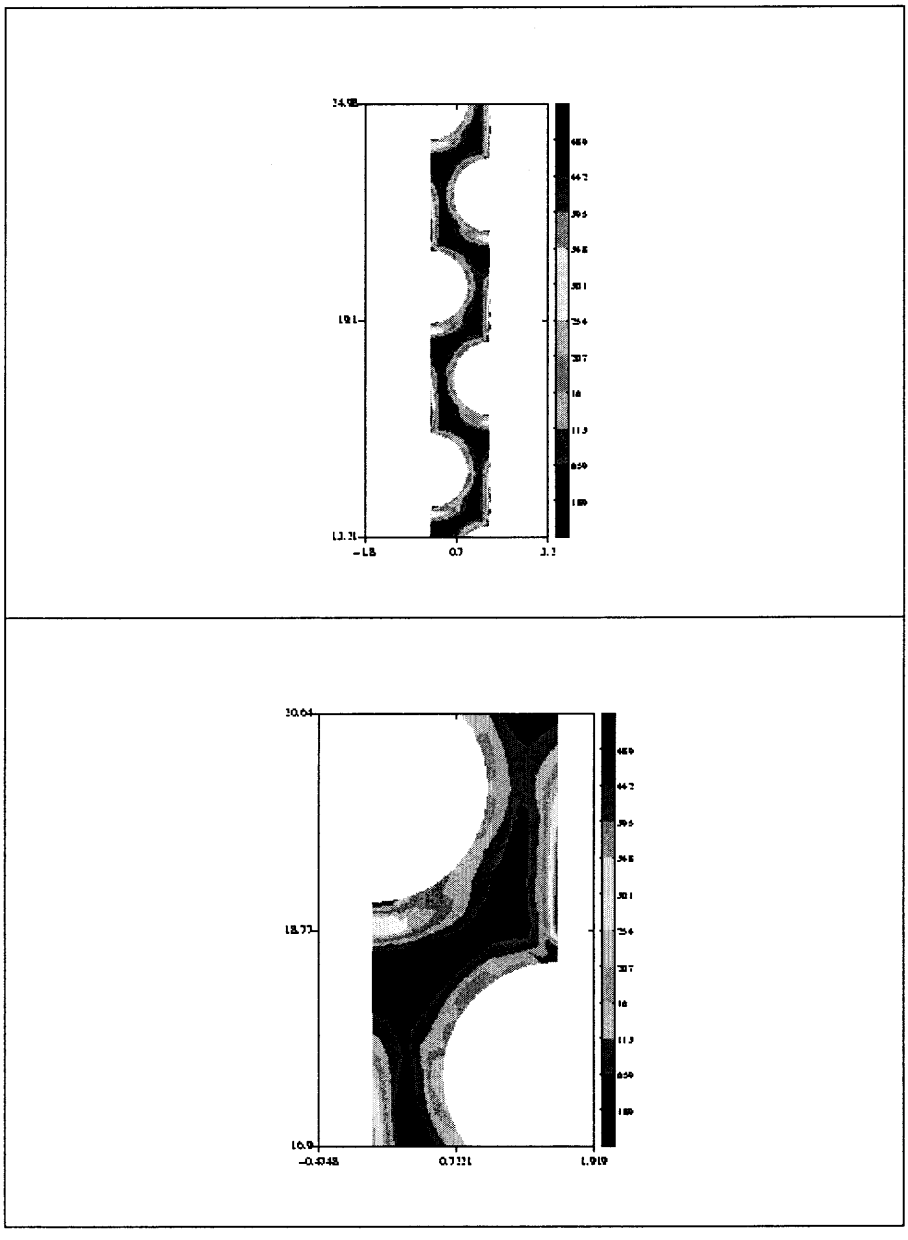

Figure 5.4 Magnified views of the trA profile

5.4 Results

In Figure 5.5, the permeability is shown as a function of the dimensionless wave number kD. From this figure it may be noticed that the permeability increases with kD for kD<5, but this increase is not monotonic. The permeability starts to decrease at kD =5 and reaches a local minimum at kD =7.7. After reaching this minimum the permeability increases with kD. The qualitative dependence of permeability on kD for viscoelastic fluids is similar to that for the Newtonian fluids reported in (2). From this figure we also note that the permeability increases as the dimensionless relaxation time is increased.

The pressure drop and the maximum value of tr**A** are plotted as a function of the Deborah number for different values of λ are shown in Figures 5.8 and 5.9.

5.4.1 Variation with kD

From Figure 5.8 it may be noticed that the pressure drop decreases with increasing kD i.e., the smallest pressure drop is for the biggest value of kD=8.37. For kD =3.59 the area available to the flow is smaller therefore pressure drop is large. On the other hand, if kD is increased, i.e., to kD = 4.18 the pressure drop decreases substantially, furthermore, it can be seen in the Figure 5.8 that for kD = 8.37 the smallest pressure drop is obtained.

The results of these numerical simulations for the permeability of periodic array of cylinders for Newtonian flows are in good agreement with the results published in (16), (54). In these papers the results are obtained for the triangular (T) and square (S) arrays of cylinders. It is easy to show that for the square array kD = 2π and for the triangular array kD = 8.269. The results for the other kD values, which correspond to the other periodic arrangements of Figures 4.1b and 4.1c, are not available.

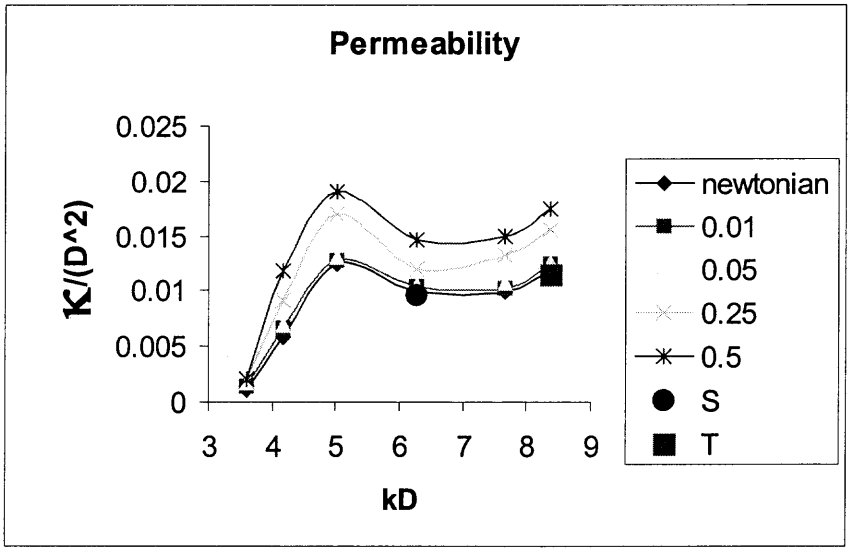

Figure 5.5 Viscoelastic permeability as a function of kD

The trace of configuration tensor $\underline{\underline{A}}$ (trA), which is a measurement of extensional effects, can be measured experimentally using the birefringence technique. According to the results shown in Figure 5.7, the tr**A** decreases when increasing kD The largest value of tr**A** is for kD = 3.6 and the smallest value is for kD = 8.37. This is due to the fact that for the bigger values of kD the shear rate in the medium is smaller as the area available becomes larger. The pressure drop and tr**A** follow the same pattern with the variation of kD, and also seem to converge to the specific values with the variation of kD. This means that for a given De the pressure-drop will converge to a unique value when kD is increased. There will be a point beyond which the pressure drop remains unchanged for any value of kD as long as it is less than 7.66. Also note that the product $w\lambda$ is equal to 4.0 at all the times. It can be observed that a similar behavior applies for the tr**A**.

5.4.2 Variation with De

The pressure drop decreases with increasing De while the tr**A** increases with increasing De though in both cases the pressure drop and tr**A** follow the same pattern, in other words every curve seems to converge to certain value as De is increased.

In real applications, the De is known (given or assumed), and it can also be estimated when mixing different fluids by averaging them. The value of De can be used in the design of any needed equipment. For instance, the value for the pressure drop can be calculated and this value can be used so that the appropriate size of the equipment can be designed in a proper manner and not oversize or over-dimensionalized, also the costs of running operations can be minimized efficiently.

The pressure-drop for viscoelastic flows is higher than for Newtonian flows, the latter can be seen in Figure 5.8. This fact has been demonstrated in this study and can be corroborated by many other research papers, and the reasoning behind it, is that the polymer molecules are being stretched in the viscoelastic flows and consequently a higher value of pressure is needed to overcome the flow. For Newtonian flows this behavior is not seen since they are pure viscous and the value of the Re is relatively small, and only very close to the walls the viscosity value will have remarkable effects due to the boundary layer. It can also be noticed that the value of the pressure drop for Newtonian flows is independent of the value of kD, the latter can be seen in Figure 5.8 as well.

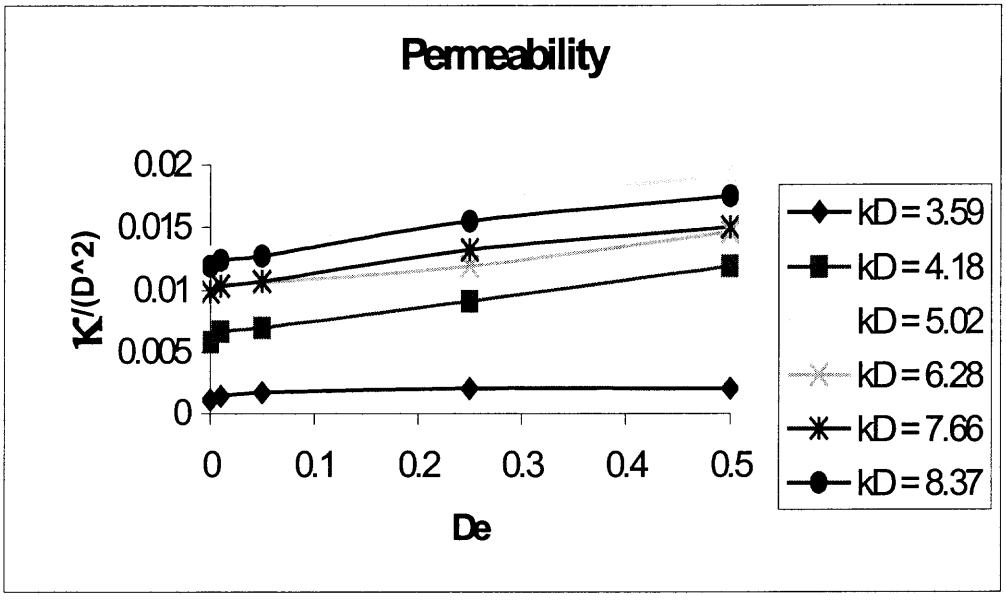

Figure 5.6 Viscoelastic permeability as a function of the De

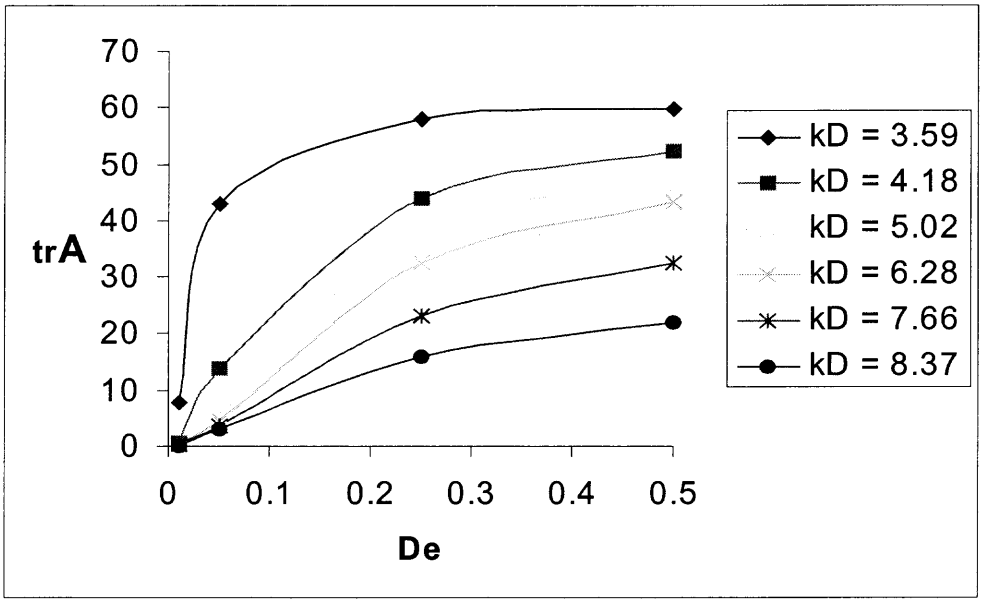

Figure 5.7 Maximum values of trA as a function of De

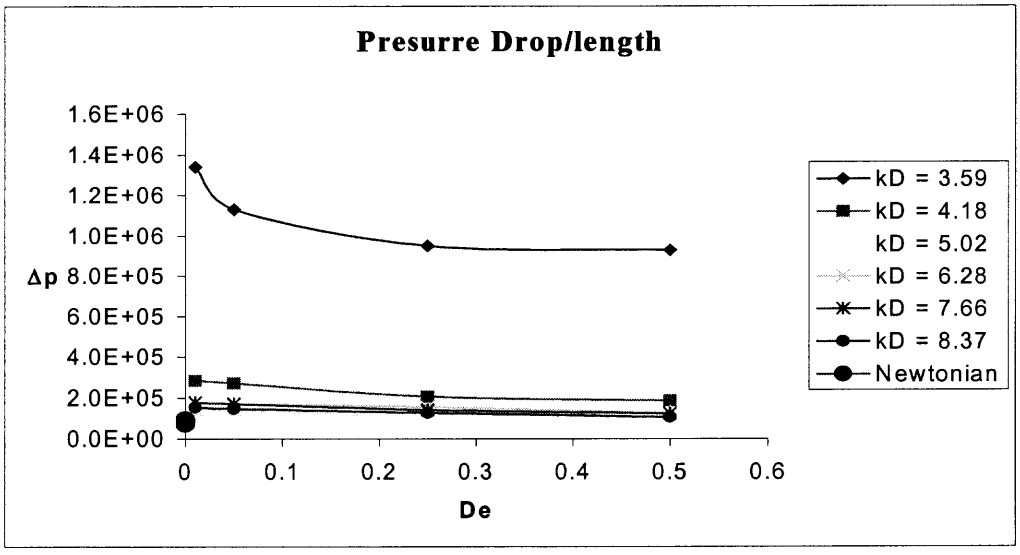

Figure 5.8 Pressure drop per unit length in the fluid flow direction

CHAPTER 6

VISCOELASTIC FLOW IN A FOUR-TO-ONE CONTRACTION

6.1 Introduction

This Chapter describes the numerical solution of a viscoelastic fluid, modeled by the Chilcott-Rallison version of the FENE dumbbell model, passing through a four-to-one contraction. Figure 6.1 shows a typical two-dimensional four-to-one contraction.

The four-to-one and other contractions are found in the extrusion devices used for processing polymeric materials. When the fluid crosses an abrupt contraction the flow area changes suddenly and the material fluid elements are subjected to relatively large extensional strain rates. A polymeric material element because of its very complex molecular structure exhibits a complex flow behavior when it is subjected to large extension rates. Also, its behavior is not only highly nonlinear but also viscoelastic. The viscoelastic flow is especially difficult to compute near the corner where the velocity gradient is singular, i.e., the stress approaches infinity at the corner. In this Chapter the velocity and stresses distributions are numerically studied both near and away from the corner.

Many researchers have numerically and analytically studied the problem of four-to-one contraction, among those are Davies and Devlin (14), Hinch (24), Renardy (52) and Singh and Leal (). All of these researches have studied the flow in the vicinity of the singular point (corner).

Renardy numerically obtained a solution for the Maxwell fluid assuming that the velocity field is the same as for a Newtonian fluid. This simplification allowed him to transform the constitutive equation for the stress into an ordinary differential equation

(ODE) by integrating along streamlines of the undisturbed flow. He assumed that there is a core region away from the walls in which the solution can be approximated by the following form $r^{-0.74}f(\theta)$. He also showed that there is a boundary layer region near the walls in which there is a stronger but integrable stress singularity, $O(r^{-0.91})$.

Davies and Devlin (14) and Hinch (24) also searched for an analytical solution of the corner flow problem of an Oldroyd-B fluid. Both analyses assumed that a solution of separable form exists (just like Renardy), but only Hinch considered this form in the limit when $r \rightarrow 0$, see Figure 6.3. Hinch was able to obtain predictions taking into account the non-Newtonian form for the velocity field. He showed that the stress singularity in the core region is of the form $r^{-2/3}$ and of form $r^{-4/9}$ for the velocity gradient.

In most previous numerical studies, except in Singh and Leal (58), the solutions were obtained by using the regular finite element method without any special attention to resolve the viscoelastic stresses near the corner. More specifically the resolution was increased at the corners by making the elements in the mesh smaller but without any changes in the element configuration (e.g., the number of elements around the corner). Using the latter discretization, it is difficult to obtain a solution to either the Upper Convected Maxwell model (UCM) or the Oldroyd-B model when the value of Deborah number is too large or when the element size is too small, as the numerical methods fail or the solutions loses its spatial smoothness.

Keunings (29) proved that the maximum value of the Deborah number for which a converged solution can be obtained actually decreases when the mesh resolution is incremented. Therefore, when a relatively coarse mesh is used, the maximum value of the Deborah number at which convergence failure occurs is relatively higher (see Dupont and

Crochet (18) and Luo and Mitsoulis (36)). Moreover, Apelian (3) and Coates (8) have also shown for both the UCM and Oldroyd-B model, that the maximum Deborah number for which a converged solution can be obtained decreases with increasing resolution. Their numerical simulations show that the viscoelastic stresses at the corner grow as r^{-1}, see Figures 6.3, 6.4 and 6.5. Since for their numerical solution the stress field varies like r^{-1}, it is not square integrable, and thus they concluded that for high Deborah numbers a numerical solution for these models cannot be obtained using the finite element method.

To avoid the high Deborah number problem, Apelian created a new model called the Modified Upper Convected Maxwell model (MUCM), in which the maximum value of stress is limited, and controlled by two independent parameters α and F, see (3).

The behavior of the FENE dumbbell and the MUCM models are similar in the sense that both have a limitation on the maximum value of the stress. In the case of the FENE dumbbell model, L (finite extensibility parameter) limits the trace of the configuration. Assuming small values for L, and α and F respectively, the models seem to converge for a bounded solution for the corner problem. Moreover the stress field at the corner for both the MUCM and the FENE models varies like a Newtonian flow, i. e., $r^{-0.5}$

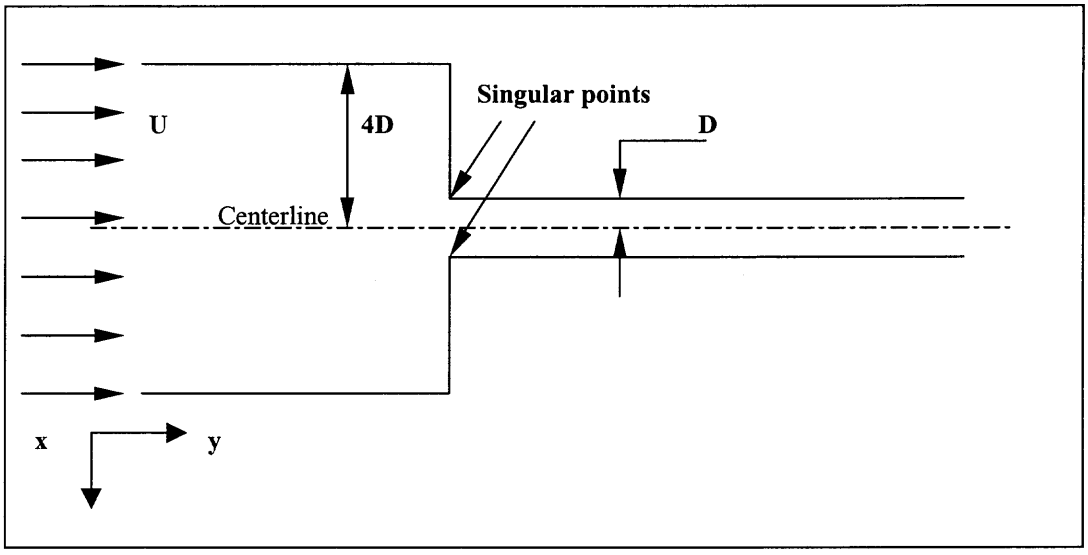

Figure 6.1 A schematic of the four-to-one contraction device.

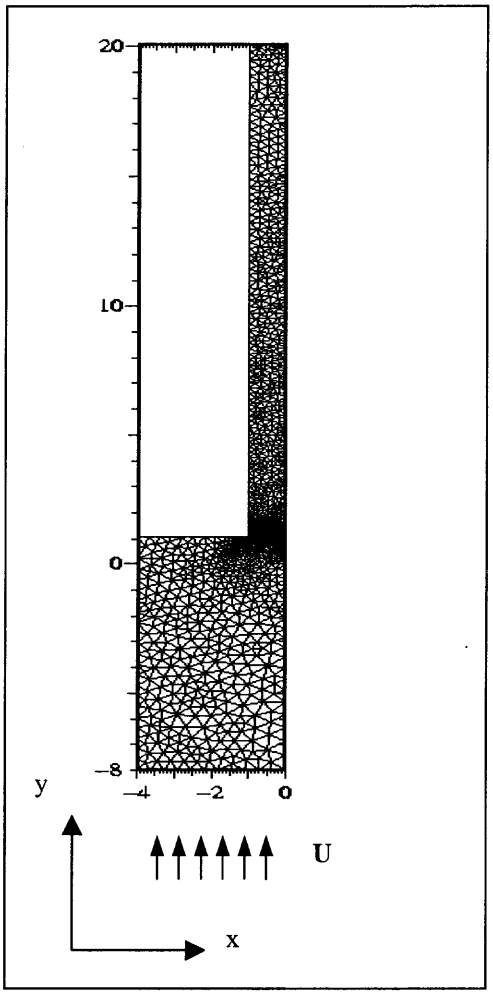

Figure 6.2 Typical finite element mesh used in our calculations.

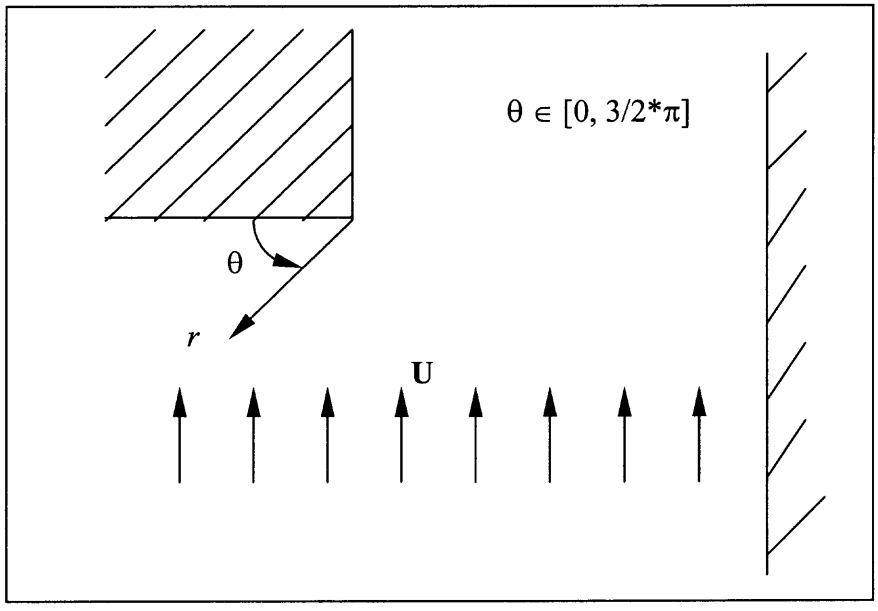

Figure 6 3 The r -θ coordinate system used at the corner.

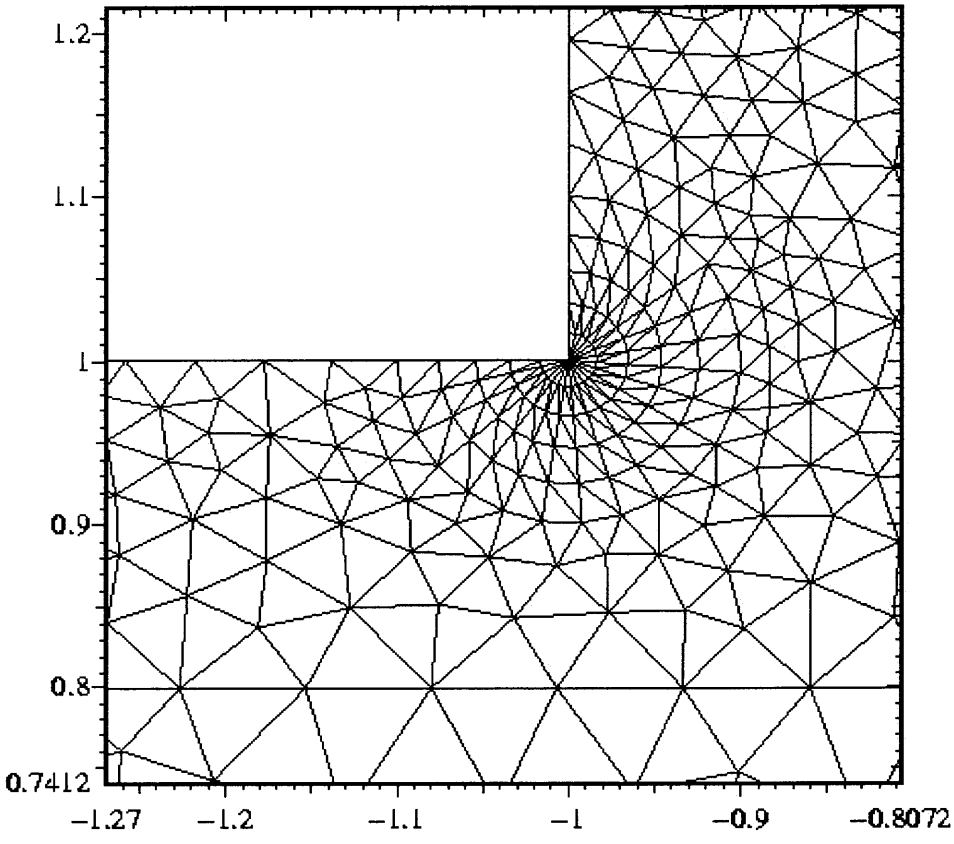

Figure 6.4 Radial mesh at the corner

The aim of this Chapter is to show that converged solutions for the Chilcott-Rallison FENE dumbbell model, both near and away from the corner, can be obtained by using a special discretization around the corner, and to describe the behavior of material polymeric elements in a four-to-one contraction device.

As noted before, the main reason for the numerical problems faced by other researchers are due to the discretization used around the corner. In order to explain this we note that the stream function around the corner has the following separable form for the Newtonian flows: $\psi \approx r^{\lambda} f(\theta)$. This implies that the velocity gradient field retains θ-dependence even in the limit $r \to 0$. In fact, the magnitude of velocity gradient variation with θ increases as the corner is approached. But, when a typical mesh with three to six elements near the corner is used the main difficulty is that there is inadequate θ-resolution for resolving this complex θ-dependent variation near the corner.

In this study, as in Singh and Leal (), a radial mesh has been created which allows us to increase θ-resolution near the corner, see Figures 6.4 and 6.5. It is also shown that for the FENE dumbbell model, solutions for relatively high Deborah numbers O(1) can be obtained using a fine radial resolution at the corners and a relatively high value of L, the dumbbell extensibility parameter $O(L^2 = 600)$.

There is a region near the corner ($r << 1$), where the viscoelastic stress increases as $r^{-\mu}$, in agreement with Hinch and Renardy for the Oldroyd-B model. In this work, for some cases L is taking to be sufficiently large so that the solution is independent of L. Also, note that in the limit when f(tr$\boldsymbol{A}$) is approximately equal to one the FENE dumbbell model and the Oldroyd-B models are identical which is the case when L is sufficiently

large. Consequently, the solutions described in this chapter for these cases with L large for the FENE model are comparable to that obtained by Hinch.

Also note that the solutions obtained for the FENE dumbbell model will depend on the polymer concentration c. For c=0, the contribution of the polymer to the stress field is zero and thus the velocity field is the same as for the Newtonian fluid. These results can be compared with those of Renardy where the velocity field is assumed to be the same as for the Newtonian fluid.

In order to compare the numerical results presented here for the FENE dumbbell with the analytical results it is assumed that the configuration tensor is of the separable form: $\boldsymbol{A} \approx r^{\mu(\theta)}\, g(\theta)$. For simulations $\mu=\mu(\theta)$, but, there is a region where μ is almost constant. Close to the walls the magnitude of $\boldsymbol{A}$ depends on the value of θ, for c=0, the value of $\boldsymbol{A}$ on the walls should be identical, since it is a pure shear flow. On the walls, the governing equation for $\boldsymbol{A}$ turns out to be algebraic, since the velocity on the walls is zero. For $c\neq 0$ the solutions using the finite element method are obtained. There is a region where μ is almost constant, but close to the walls the polymer contribution to the stress varies with θ, therefore, the velocity gradient and the configuration tensor will also depend on θ, see Figure 6.5.

The velocity and configuration fields have different behavior near the corner. The spatial distribution of the velocity field will be described in terms of the magnitude of the local strain-rate tensor: $|\mathbf{D}| = \sqrt{\mathrm{tr}\left[\mathbf{D}\mathbf{D}^{\mathrm{T}}\right]}$, which is a measure of the rate of strain tensor. The spatial distribution of the configuration tensor is described in terms of its trace, i.e. $\mathrm{tr}\boldsymbol{A}=A_{11}+A_{22}$, which is a dimensionless measure of the length of the dumbbell.

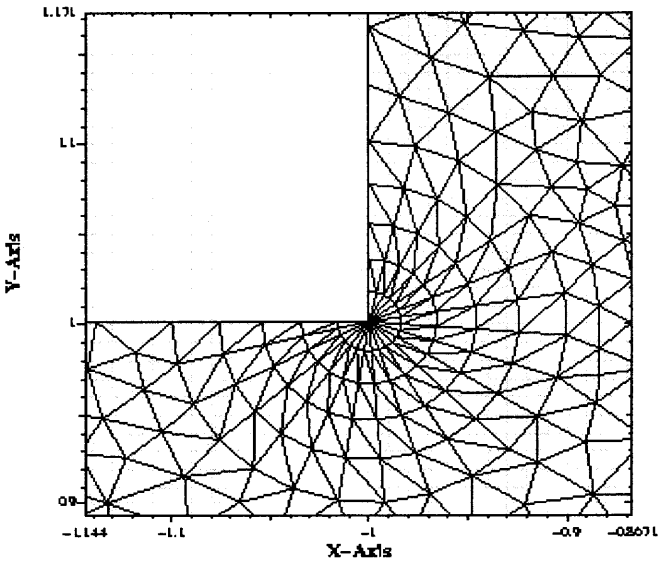

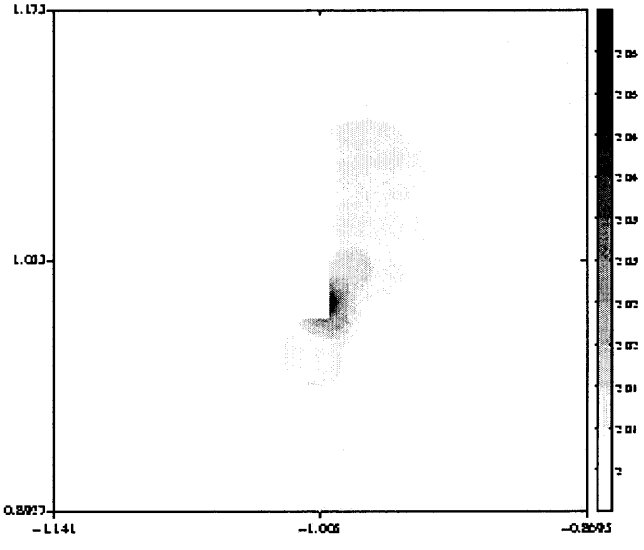

Figure 6.5 The corner mesh and the viscoelastic stresses near the corner

6.2 Definition of the Domain

A typical four-to-one contraction geometry is shown in Figure 6.1. The symmetry allows us to use one half of the actual domain as the computational domain, see Figure 6.2. This reduces the size of the computational problem by one half and thus also the computational time needed for solving the governing equations.

6.3 Boundary Conditions

The incoming velocity U along the y-direction is assumed to be parabolic at y = -8, with a value of U=0 for x = -4, and U=1 for x = 0. Along the y-axis (x = 0) the following boundary conditions are imposed: u=0, $\frac{\partial v}{\partial x}$, where u and v are the x and y components of the velocity. The velocities u and v on the walls are assumed to be zero.

The Reynolds number in the present study is assumed to be Re = 3.3×10^{-3}, for both Newtonian and viscoelastic fluids. The inertial effects are therefore negligible. Thus, for a given geometric configuration of the domain, the problem is completely characterized by the three parameters, De, c and L. In the present work, the behavior is investigated for a range of values for De $\in$ [0.02, 0.2, 0.5, 1.0], L^2=600 and c=0 and1.0.

6.4 Stokes Flow Around a Corner

A solution for the Stokes flow around a corner of arbitrary angle was found by Dean and Montagnon (15) and Moffatt (41) to be of the following form $\psi = r^{\lambda} f(\theta)$, where ψ is the stream function, and r and θ are as shown in Figure 6.3. They also showed that by using the stream function formulation the strain rate magnitude is of the following form: $|\mathbf{D}| = r^{\lambda - 2} f_1(\theta)$. For the Newtonian case for a $3\pi/2$ corner, the strain rate

becomes singular when $r \rightarrow 0$. It is clear that the tangential gradients of $|\mathbf{D}|$ become larger when $r \rightarrow 0$. In order to compare the analytic solutions with the numerical solutions shown later, the log-log plots are used. Also note that since $\log |\mathbf{D}| = (\lambda-2)\log r + \log f_1(\theta)$, $\log |\mathbf{D}|$ varies linearly with $\log(r)$. For Stokes flows the slope $\lambda-2 \approx -0.445$ (see Dean and Montagnon (15) for details). For different values of θ, a family of straight lines will be displayed. This family of straight lines will be compared with the results obtained using the finite element numerical scheme for Newtonian flow.

Before comparing the analytical solutions with the numerical solutions, it is important to note that the analytical solution for $|\mathbf{D}|$ is singular at $r = 0$ because the exponent is negative. The numerical solution on the other hand converges to a steady value when $r \rightarrow 0$. For r-values smaller than the size of the radial element the numerical and analytical solutions therefore, cannot be compared. The numerical and analytical solutions however can be compared for r larger than the size of an element, which for the present simulation is for $r \in$ [1.6E-02, 0.21]. The latter will be observed in the following sections.

The numerical solutions for both Newtonian and viscoelastic liquids are obtained using the same radial finite element mesh. Figures 6.6 and 6.7 show the numerical results for the Newtonian flow using a mesh with 6273 nodes and 3000 unstructured triangular elements. Figures 6.8 and 6.9 show the numerical results for the Newtonian flow using 6923 and 5993 nodes respectively. The radial element size for the three cases considered is 0.02, 0.02 and 0.005. Also, note that only the region near the corner is refined. From these figures, it is clear that the distribution of |D| near the corner is relatively insensitive to the radial element size. Also note that for $r>0.21$ the numerically obtained $|\mathbf{D}|$ is quite

different from the analytical results discussed above, as for this region the global solution dominates over the corner singularity. Therefore, for $r \geq 0.21$ the numerical solution starts to transition from the local behavior expected at the corner to the solution for the global flow field.

The values of $|\mathbf{D}|$ in the numerical results for smaller values of $r < 0.001$ start to converge to a fixed value when $r \rightarrow 0$. This departure between the analytical and numerical solutions for small r's as noted above, and also explained in (58) occurs at smaller values of r with increasing corner resolution. The numerical solutions for this Newtonian fluid case converged for the radial finite element mesh described above.

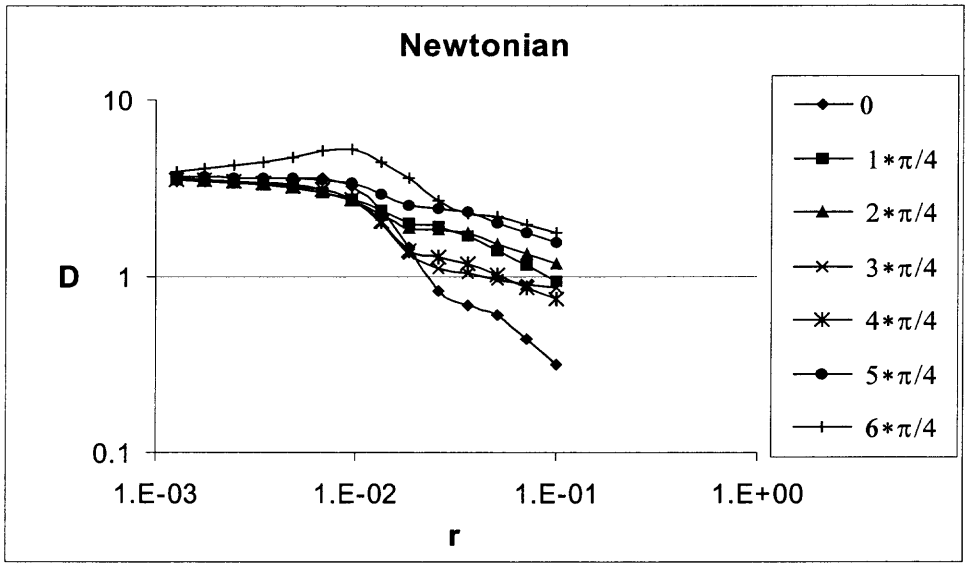

Figure 6.6 For Newtonian fluid log |**D**| is plotted as a function of log(r) for different values of θ. Number of nodes is 6273.

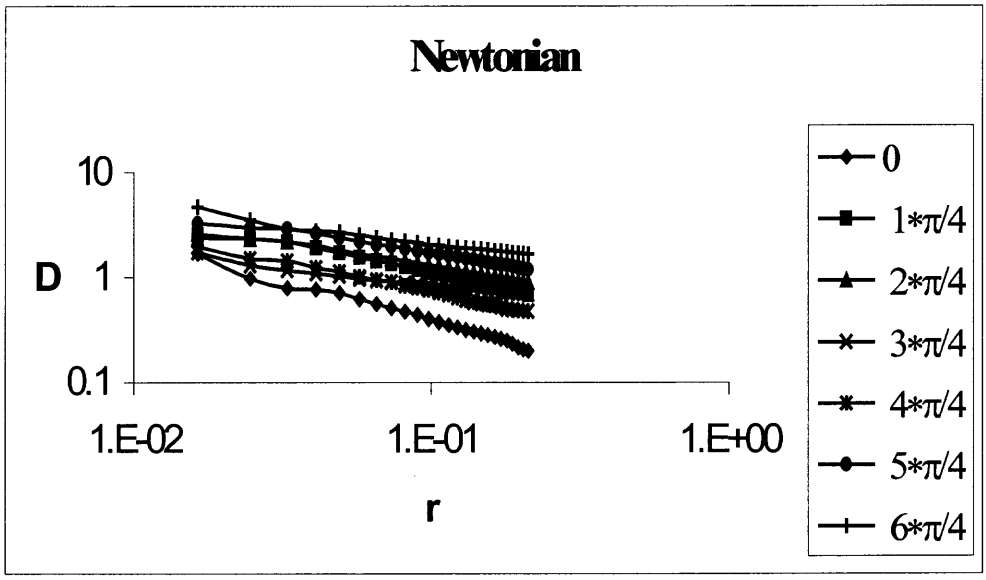

Figure 6.7 For Newtonian fluid log |**D**| is plotted as a function of log(r) for different values of θ, for r between 10^{-2} and 2.1×10^{-1}. Number of nodes is 6273.

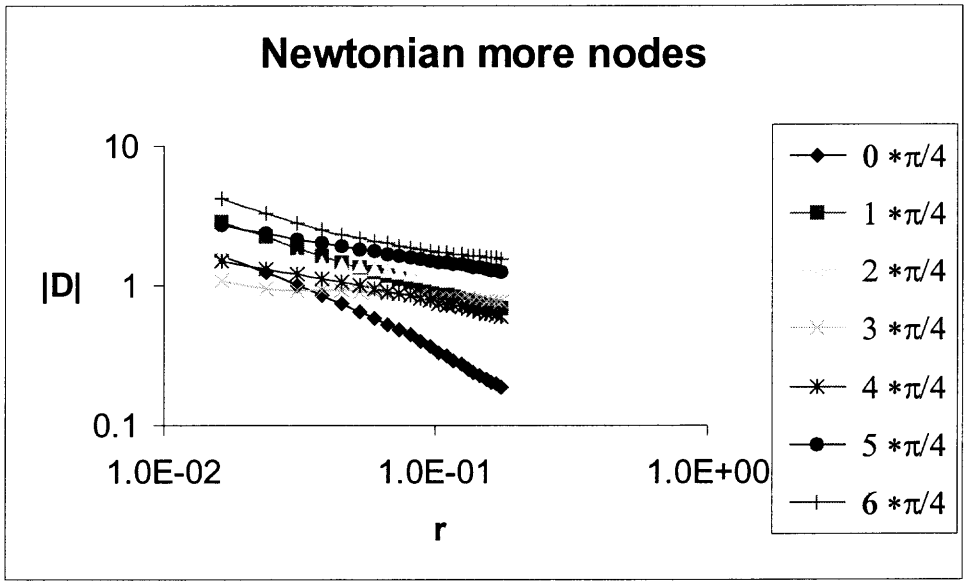

Figure 6.8 For Newtonian fluid log |**D**| is plotted as a function of log(r) for different values of θ, for r between 10^{-2} and 2.1×10^{-1}. Number of nodes is 6923.

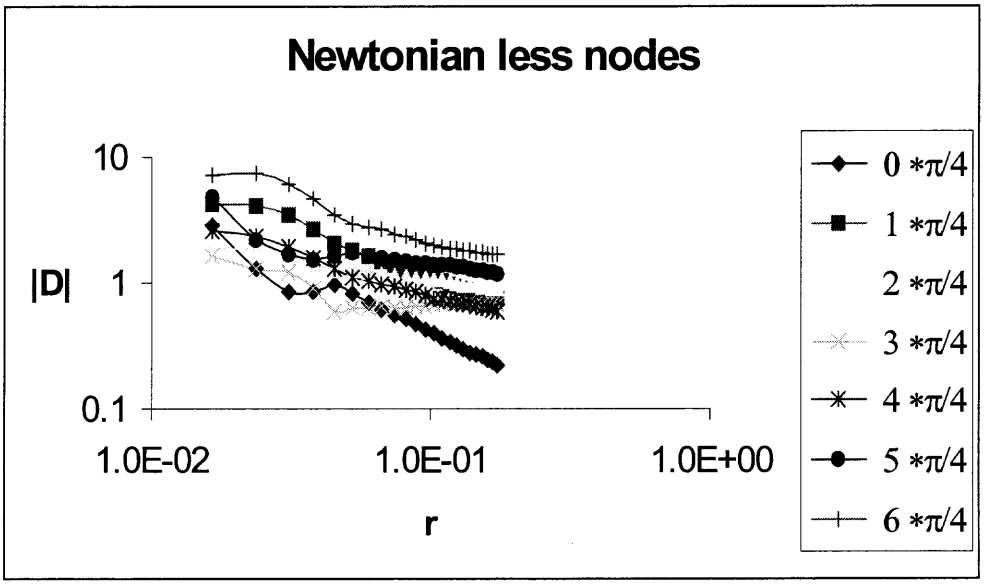

Figure 6.9 For Newtonian fluid log |**D**| is plotted as a function of log(r) for different values of θ, for r between 10^{-2} and 2.1×10^{-1}. Number of nodes is 5993.

6.5 Viscoelastic Flow Near the Corner

The numerical solutions for the Newtonian flow in a four-to-one contraction was used as the starting point for the calculations of viscoelastic fluid. The solution of a viscoelastic fluid will depend on the value of the dimensionless relaxation time (Deborah number, De). Four different values of Deborah number were used for these numerical calculations, i.e., De = 0.02, 0.2, 0.5 or 1.0. The effect of using different values for De will be shown in Figures 6.11, 6.12, 6.13 and 6.14.

Analysis of these figures, shows that the slope of the velocity gradient field $|\mathbf{D}|$ versus r on a log–log scale close to the corner ($r \to 0$), for all θ values shown is approximately zero and the value at the corner is ~3.65. On the other hand, farther away from the corner $|\mathbf{D}|$ decreases with r.

The numerical results show that both the polymeric stresses (configuration tensor) and the velocity gradient in the vicinity of the corner can be described by generalized power laws as discussed above. Specifically, the stress and strain rates can be assumed to be of the form:

$$\boldsymbol{A} \approx r^{\mu(\theta)}\, g(\theta)$$

$$|D| \approx r^{(\lambda(\theta)-2)}\, f_1(\theta)$$

where both exponents μ and λ are functions of θ.In order to calculate the exponents for these power laws tr$\boldsymbol{A}$ and $|\mathbf{D}|$ are plotted as functions of r for several values of θ on a log-log plot. The slopes μ and λ of the linear regions on these plots will be calculated for these viscoelastic fluids. The values of μ and λ varies with θ. For $r \in$ [1.6E-02, 0.21], the slopes are almost constant, and thus the numerical solution of the above power laws.

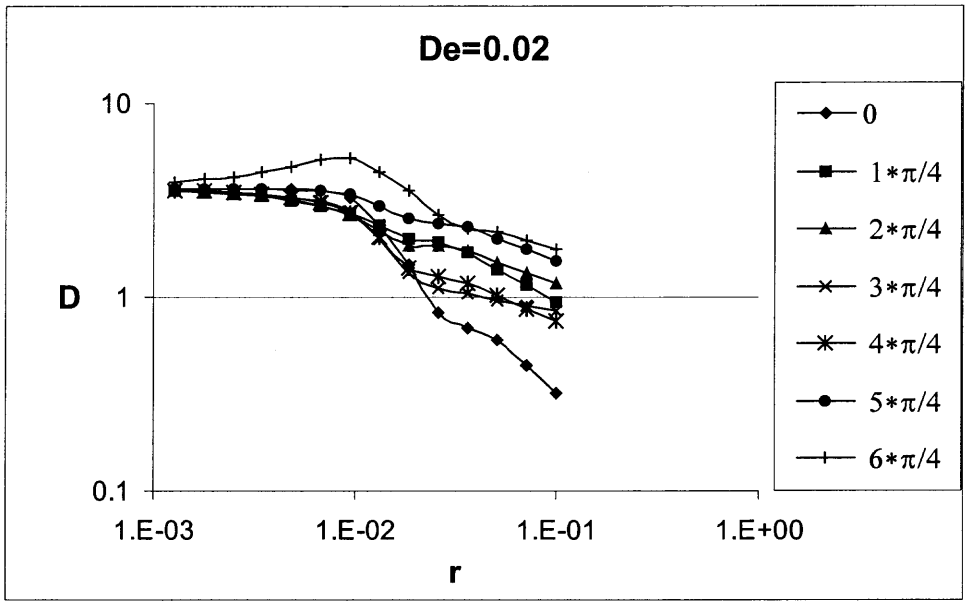

Figure 6.10 For viscoelastic fluid log |**D**| is plotted as a function of log(r) for different values of θ.

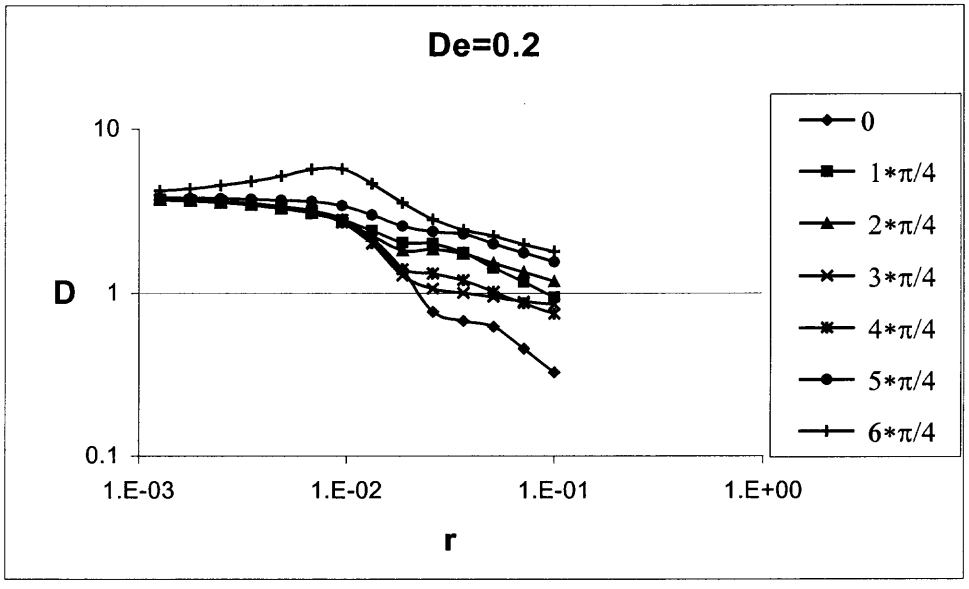

Figure 6.11 For viscoelastic fluid log |**D**| is plotted as a function of log(*r*) for different values of θ.

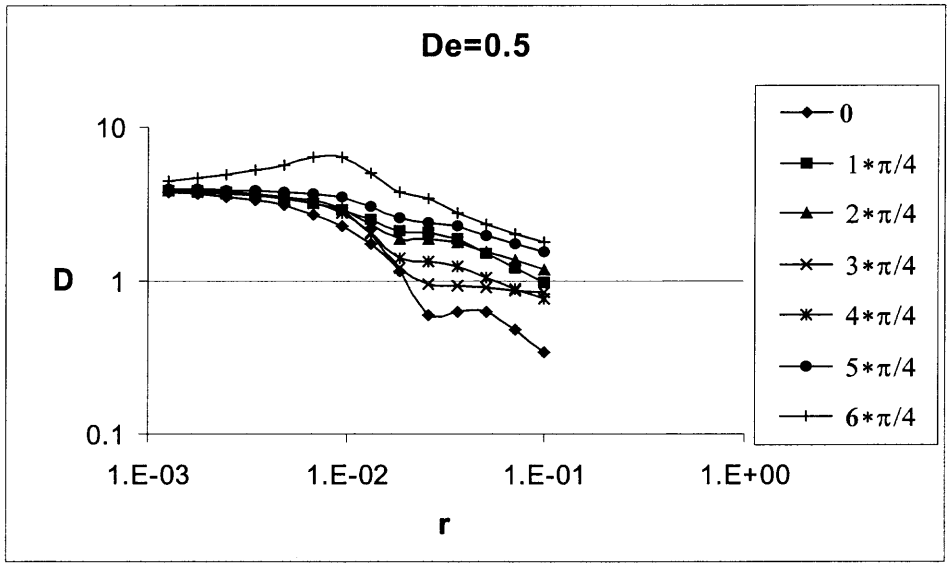

Figure 6.12 For viscoelastic fluid log |**D**| is plotted as a function of log(r) for different values of θ.

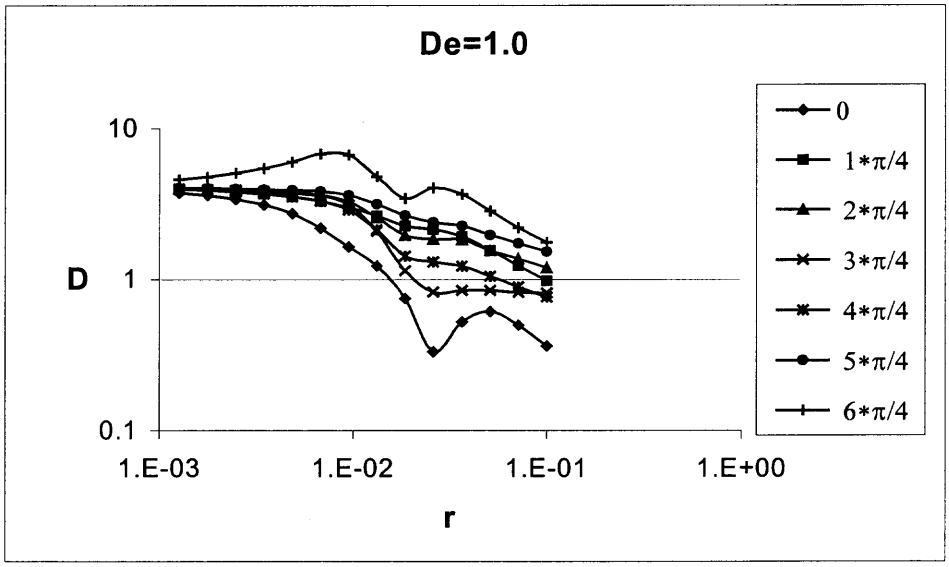

Figure 6.13 For viscoelastic fluid log |**D**| is plotted as a function of log(r) for different values of θ.

In order to calculate the exponents for the power laws, the slope is calculated in the region where variation with log (r) is linear. In Figures 6.15, 6.16, 6.17 and 6.18, values of log $|\mathbf{D}|$ are shown as a function of log (r). The linear region is for r between 1.64×10^{-2} and 0.213. It can also be stated that for the viscoelastic case the results depend on the value of the De. Also by comparing the viscoelastic solutions with the Newtonian solutions shown in Figures 6.6 and 6.7, it can be observed that the slopes in the linear region are different but the pattern of the solutions is quite similar.

Figures 6.6 and 6.7 shows the case of pure Newtonian solution, i.e., when the polymer concentration is zero (c = 0), the solution corresponds to an infinitely dilute solution where the velocity field is held fixed, but the polymer configuration is allowed to evolve. The configuration obtained in this case is identical to the configuration obtained for the Maxwell model when the velocity field is assumed to be the same as for the Stokes flow.

The case of c = 1.0 corresponds to a dilute polymer solution, where the polymer (dumbbell) conformation can be strongly influenced by the flow, but the flow itself remains very close to that for a Newtonian fluid except possibly in the regions where the dumbbells are highly stretched. Figures 6.14, 6.15, 6.16 and 6.17, show solutions for the viscoelastic cases. From these plots it can be inferred that the pattern is similar to the Newtonian solution. The velocity gradient values are slightly different but they converge towards a value close to 3.65 when $r \rightarrow 0$.

Figures 6.18 and 6.19 also show velocity gradient values in the log scale but this time the number of nodes were 5993 and 6923 respectively. The slopes of these plots are very similar to the one shown in Figure 6.17.

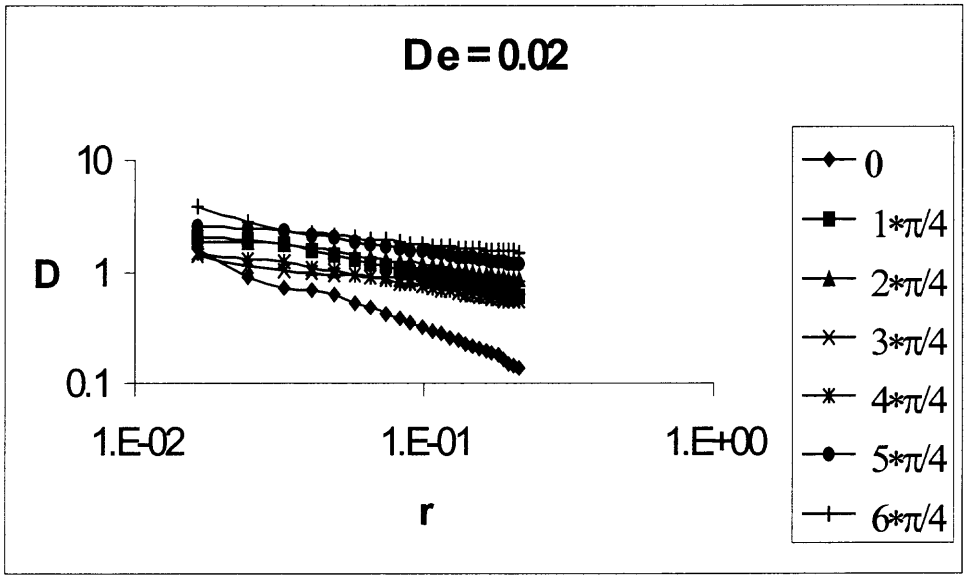

Figure 6.14 For viscoelastic fluid log |**D**| is plotted as a function of log(r) for different values of θ, for r between 10^{-2} and 2.1×10^{-1}

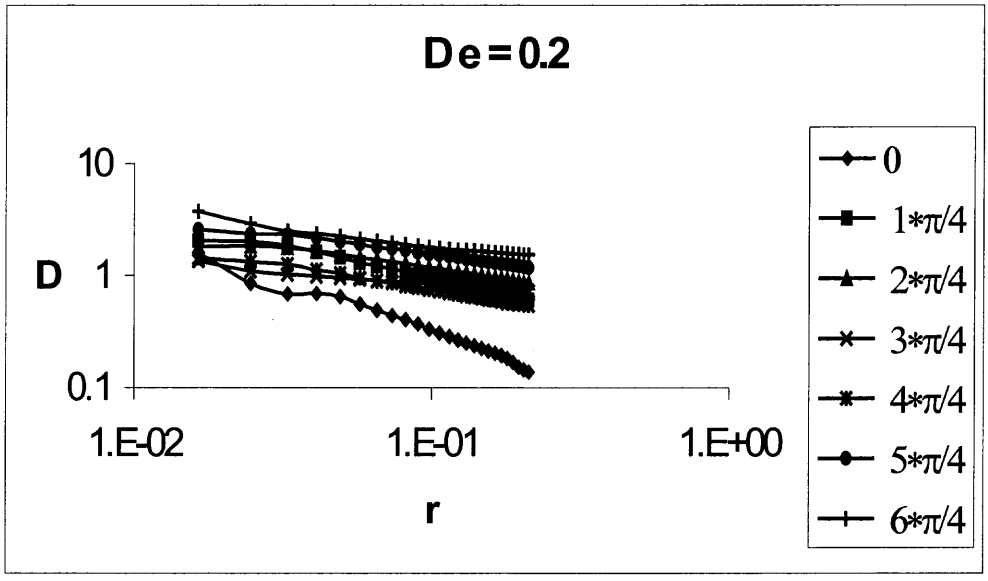

Figure 6.15 For viscoelastic fluid log |**D**| is plotted as a function of log(r) for different values of θ, for r between 10^{-2} and $2.1\text{x}10^{-1}$

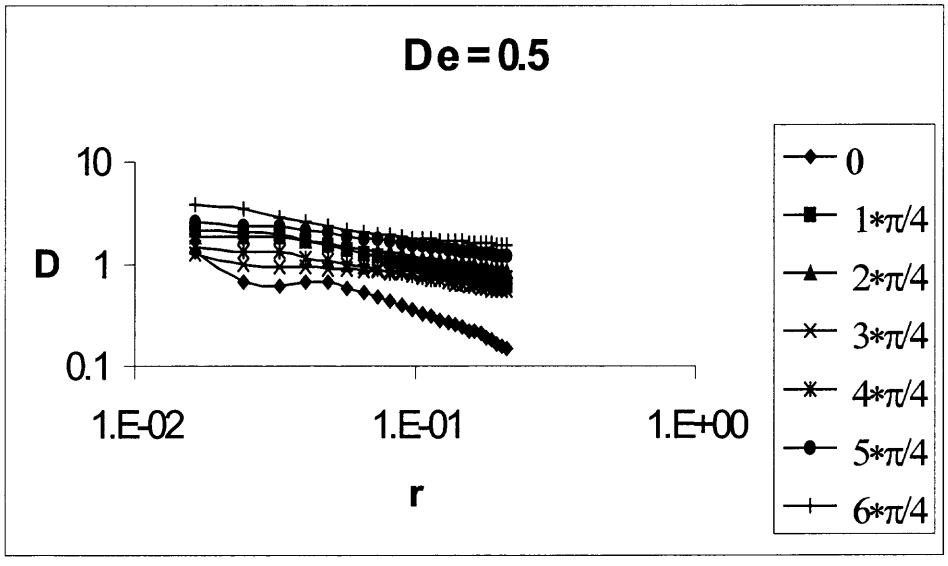

Figure 6.16 For viscoelastic fluid log |**D**| is plotted as a function of log(r) for different values of θ, for r between 10^{-2} and 2.1×10^{-1}

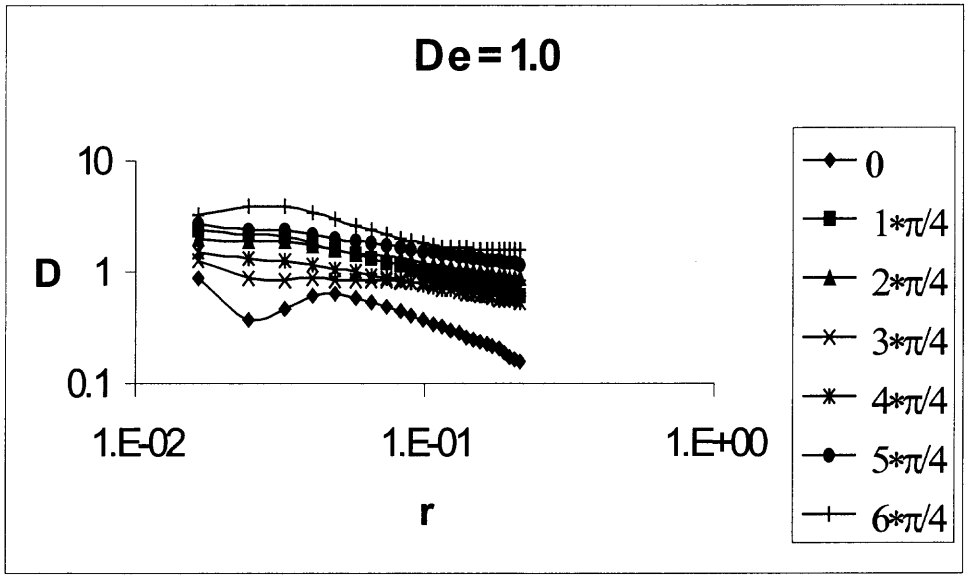

Figure 6.17 For viscoelastic fluid log |**D**| is plotted as a function of log(r) for different values of θ, for r between 10^{-2} and 2.1×10^{-1}. Number of nodes 6273.

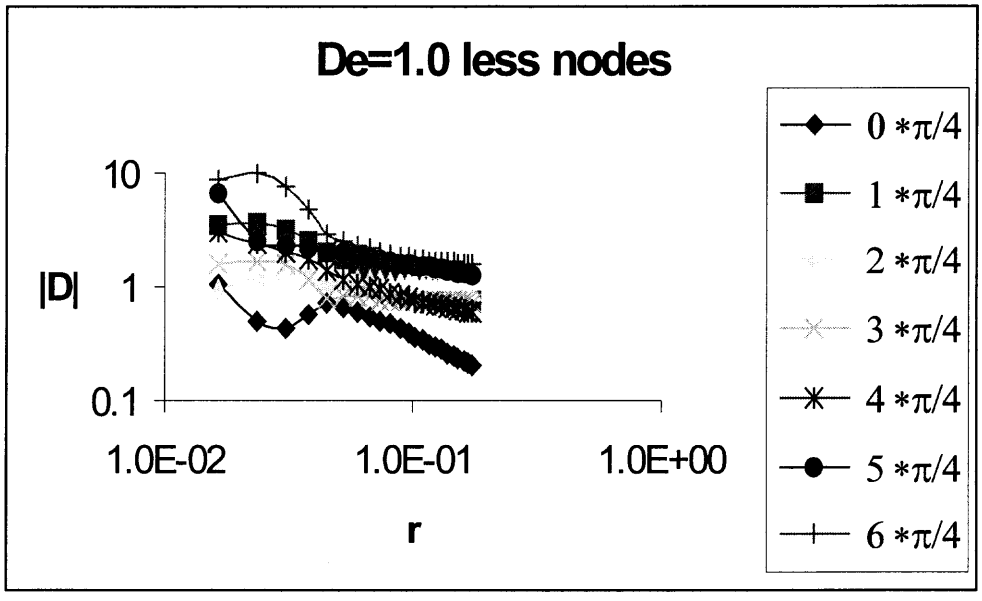

Figure 6.18 For viscoelastic fluid log |**D**| is plotted as a function of log(r) for different values of θ, for r between 10^{-2} and 2.1×10^{-1}. Number of nodes 5993.

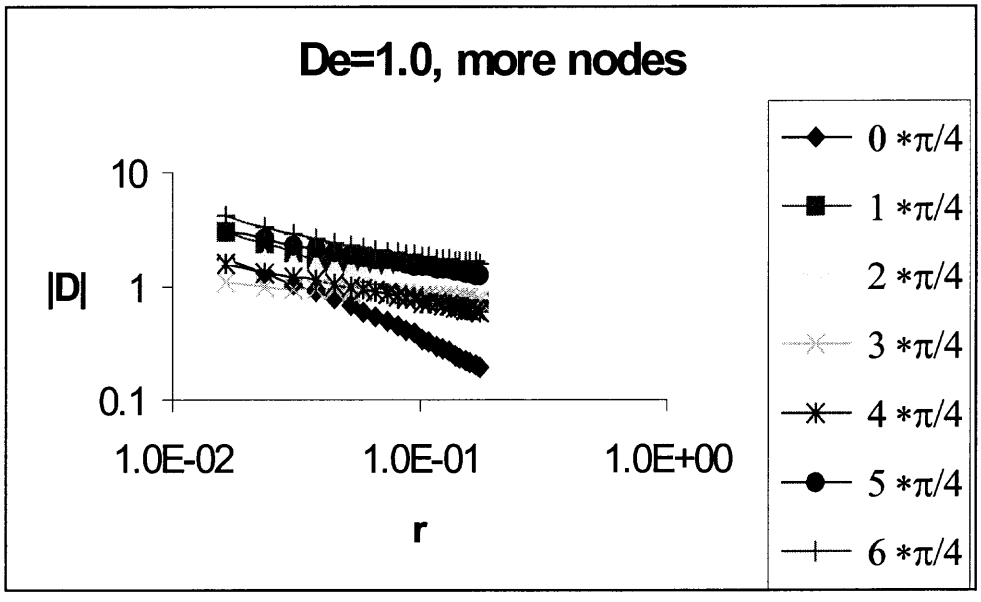

Figure 6.19 For viscoelastic fluid log |**D**| is plotted as a function of log(r) for different values of θ, for r between 10^{-2} and 2.1×10^{-1}. Number of nodes 6923.

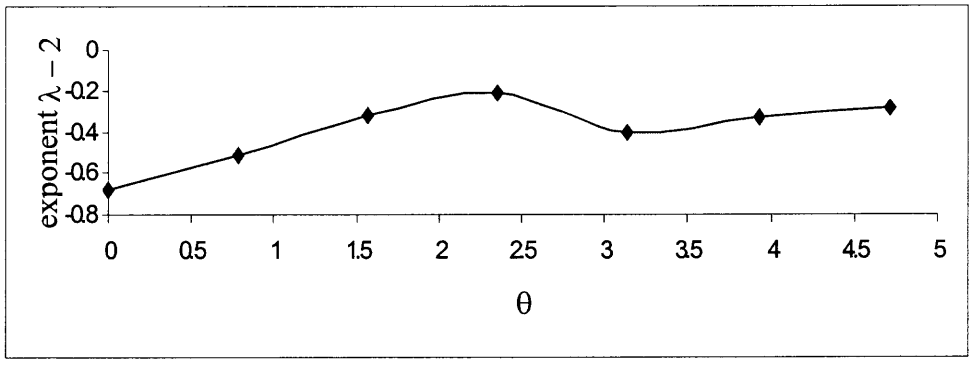

Figure 6.20 The exponent λ–2 obtained from numerical simulations if plotted as a function of θ, De = 1.0. Number of nodes 6273.

In Figure 6.20, the exponent λ is plotted as a function of θ for |D| in the power law region for c=1, De=1, L^2=600. From this figure we note that λ is not a constant. This variation with θ is due to the asymmetric distribution of the polymeric stresses near the corner.

6.5.1 Polymer Configuration

This section describes the results for the configuration tensor in the vicinity of the corner for different values of De. The slope μ in (1) is obtained by plotting log tr$\boldsymbol{A}$ as a function of log (r).

By analyzing Figures 6.21, 6.22, 6.23 and 6.24, the role of De in determining the slope is investigated. For De = 0.02, the values of the log tr$\boldsymbol{A}$ is very small, therefore the slopes of the curves with log r is very small (almost zero). In this case the flow is essentially Newtonian. These slopes start to increase for the higher values of De as the viscoelastic stresses increase with De.

In Figure 6.21, the value of log tr$\boldsymbol{A}$ is plotted in the vicinity of the corner (obtained for L^2 = 600) as a function of the log r for seven different values of θ and De =1.0. It can be seen that for small values of r, very close to the walls ($r \approx$ 1.0E-3) the value of log tr$\boldsymbol{A}$ increases with log r, until it reaches a maximum value for $r \approx$ 1.0E-2 approximately. For larger values of log r, log tr$\boldsymbol{A}$ decreases linearly with log r. But for $r>$ 1.0E-2, the log tr$\boldsymbol{A}$ value keeps decreasing and reaches a relatively constant value that depends on the value of the angle θ.

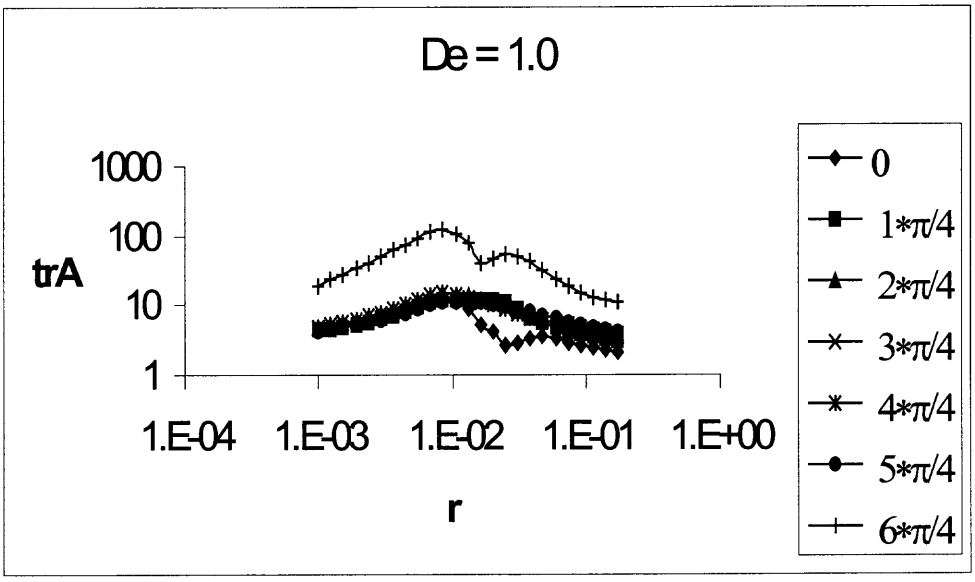

Figure 6.21 Log tr$A$ is plotted as a function of log r, for different values of θ. L^2 = 600, and c = 1.0.

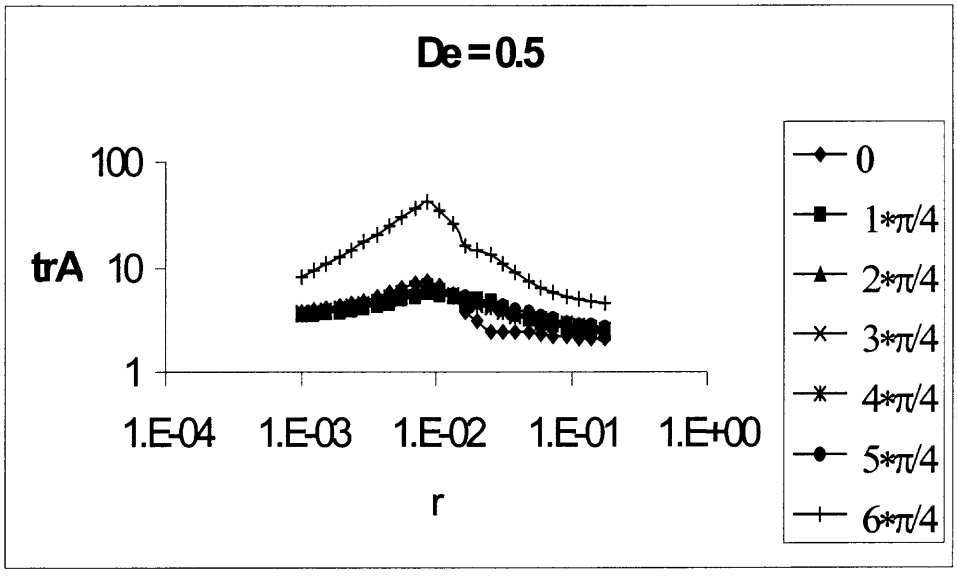

Figure 6.22 Log tr$A$ is plotted as a function of log r for different values of θ. L^2 = 600, and c = 1.0.

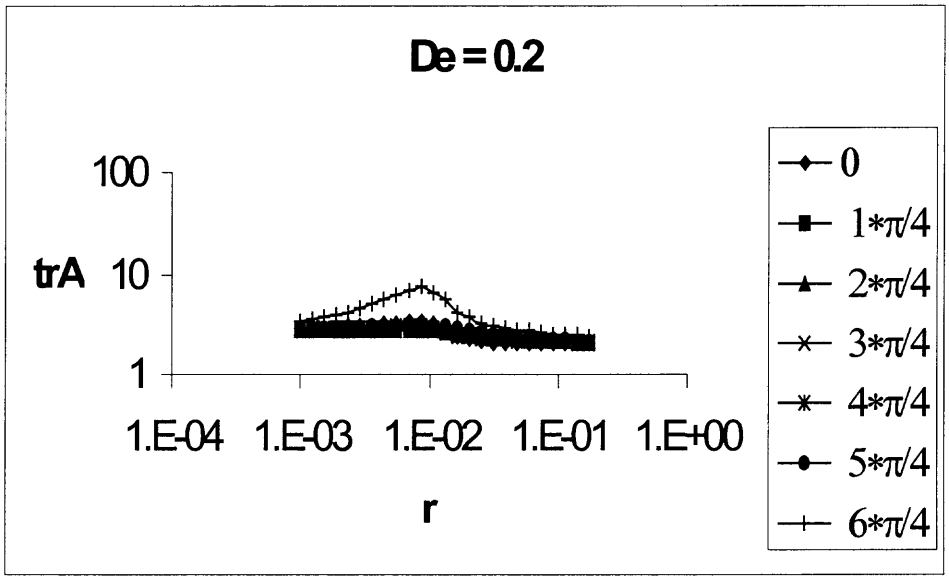

Figure 6.23 Log tr$A$ is plotted as a function of log r for different values of θ. L^2 = 600, and c = 1.0.

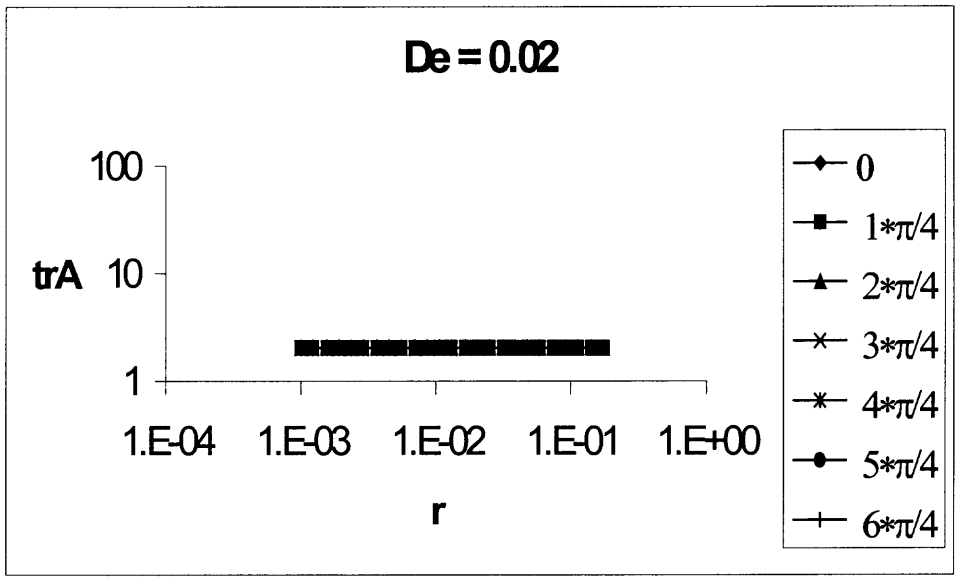

Figure 6.24 Log tr$A$ is plotted as a function of log r for different values of θ. L^2 = 600, and c = 1.0.

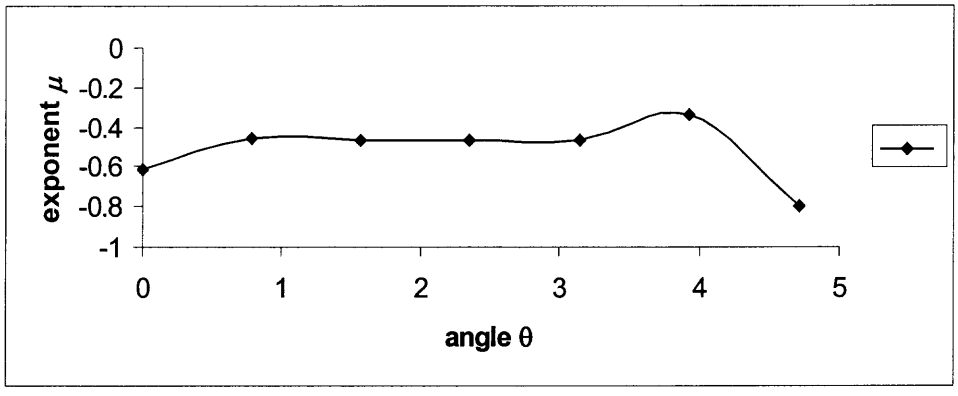

Figure 6.25 The exponent μ obtained from the FEM. De = 1.0.

In Figure 6.25, the exponent μ, i.e. the slope of the log(tr$\boldsymbol{A}$) vs log(r) plot, of the power laws is plotted as a function of θ, for De =1.0. It can be seen that away from the walls μ is approximately constant, but near the walls (θ = 0 and 4.71) the value depends on θ. This, as noted before, is due to the stress boundary layers near the walls. The results shown in Figure 6.25 are relatively close to the one obtained by Hinch, i.e. $\mu \approx -2/3$. The reason for a small difference is the numerical discretization error. The value of the tr$\boldsymbol{A}$ away from the walls is approximately constant.

6.6 Flow in a Four-to-one Contraction

In this subsection, the numerical results obtained away from the corner of the four-to-one contraction are described. As noted before, the numerically obtained solutions for the radial mesh converge both near and away from the corner for all values of De investigated. Figures 6.26, 6.27, 6.28, 6.29, 6.30 and 6.31 show numerical results for the overall fluid flow in the four-to-one contraction. In Figure 6.26, the streamlines are plotted. Notice that the streamlines converge as the area is reduced by a factor of four. Figure 6.27 shows the pressure distribution for the entire domain. As expected, the pressure decreases evenly along the fluid flow direction and the rate of pressure drop in the narrow channel is larger. Isobars away from the corner are perpendicular to the channel walls. Also note that there is a large pressure drop in the area near the corner just before the contraction.

Figures 6.28, 6.29, 6.30 and 6.31 show isovalues of log(tr$\boldsymbol{A}$) for different values of De. Since the values of tr$\boldsymbol{A}$ are larger near the corner region and much smaller away from the corner, the log scale allows us to visualize tr$\boldsymbol{A}$ distribution in the entire domain.

From these figures, it can be noticed that tr$\boldsymbol{A}$ distribution depends with De. For small De's, trA away from the corner is approximately two which means that the fluid is in a relaxed state. For higher values of De, on the other hand, tr$\boldsymbol{A}$ near and also away from the corner are larger than two. But, as expected, tr$\boldsymbol{A}$ near to the corner is larger than away from the corner. These figures also show that trA downstream of the corner is larger than on the upstream side of the corner. This is due to the hyperbolic nature of the constitutive equations. The highly stretched polymeric material elements near the corner are swept downstream of the corner and take some time to relax back. As the material elements moving away from the corner are subjected to smaller but finite strain rates they take longer than the fluid relaxation time to relax. This leads to the formation of a region downstream of the corner where trA is relatively large.

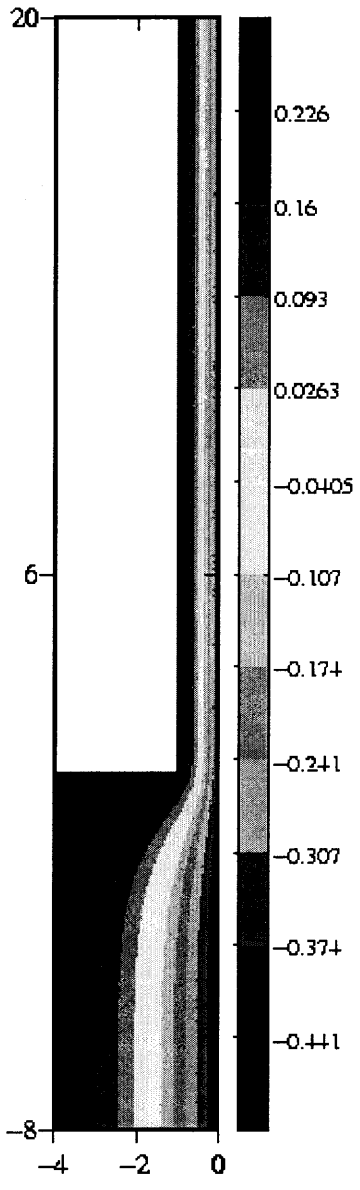

Figure 6.26 Streamlines in a four-to-one contraction device.

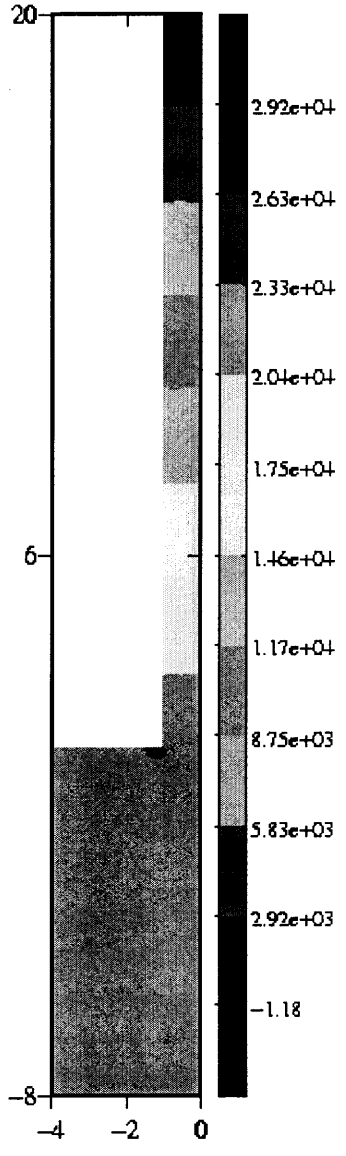

Figure 6.27 Isobars in a four-to-one contraction device.

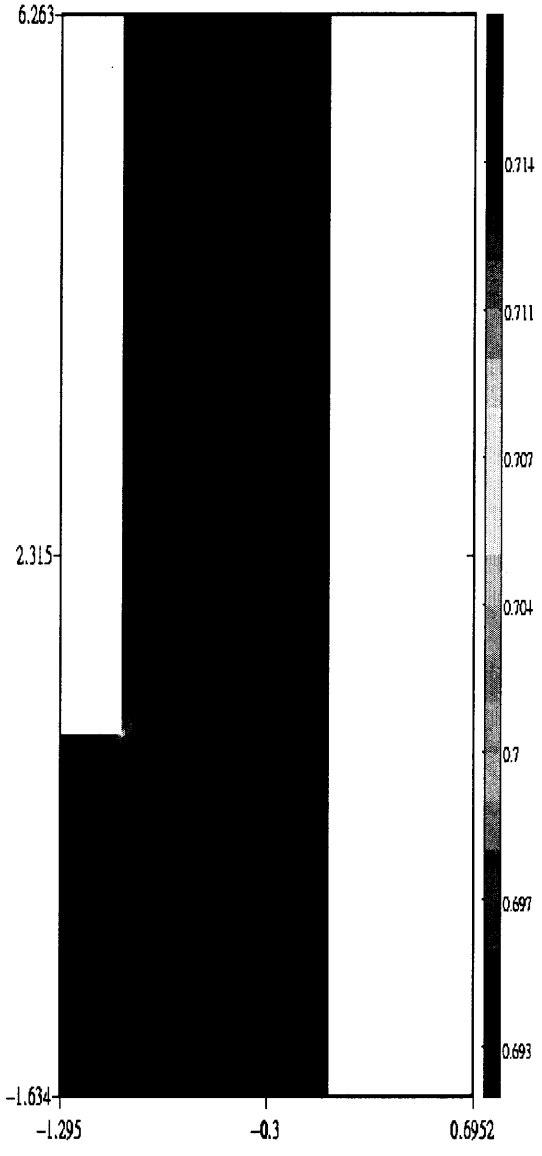

Figure 6.28 Isovalues of log(tr$\boldsymbol{A}$) in the four-to-one contraction device are shown for De = 0.02.

Figure 6.29 Isovalues of log(tr$\boldsymbol{A}$) in the four-to-one contraction device are shown for De = 0.2.

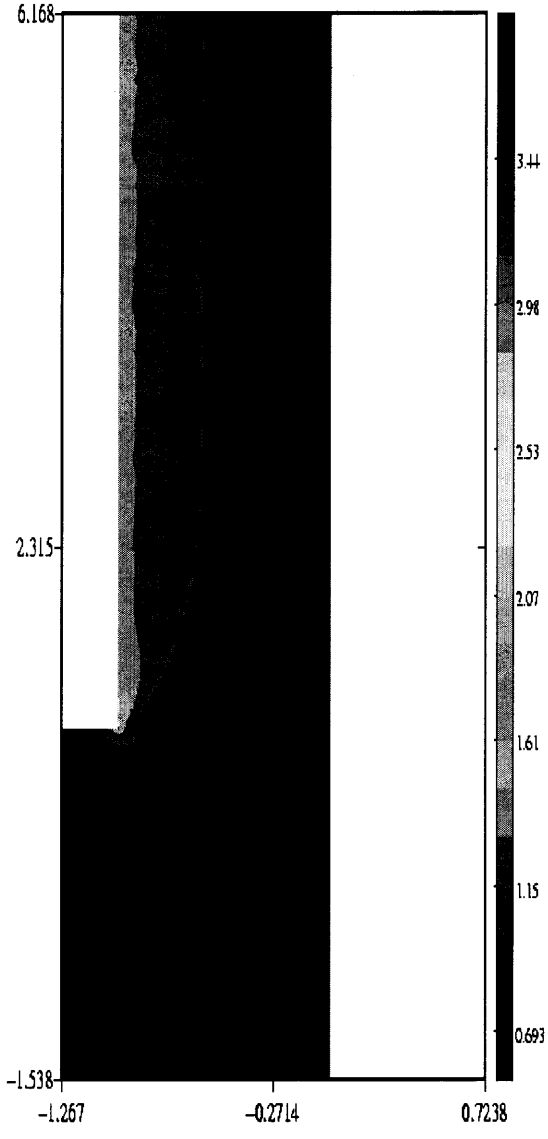

Figure 6.30 Isovalues of log(tr$\boldsymbol{A}$) in the four-to-one contraction device are shown for De = 0.5.

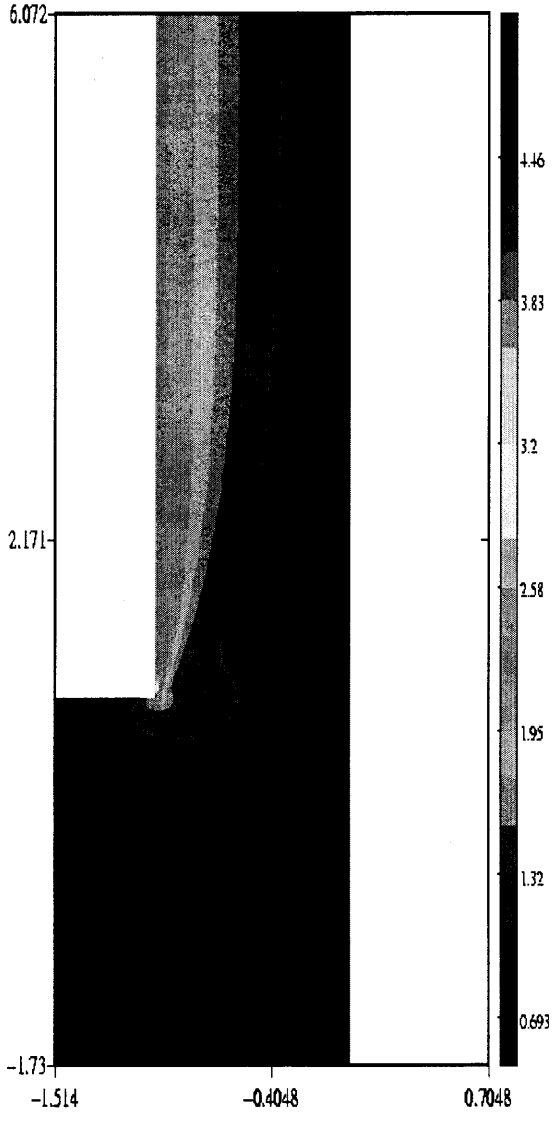

Figure 6.31 Isovalues of log(tr$A$) in the four-to-one contraction device are shown for De = 0.02.

6.7 Conclusions

The problem of a viscoelastic flow in a four-to-one contraction was studied numerically using a radial discretization near the corner. The numerical results show that by using a radial mesh, converged solutions both near and away from the corner can be obtained and that there is a region near the corner in which the configuration tensor and velocity gradient field for the viscoelastic fluid are of generalized power law form. The exponents of the power laws are computed by plotting $\log(\mathrm{tr}\underline{\underline{A}})$ and $\log|\underline{\underline{D}}|$ as a function of $\log(r)$ and computing the slope in the linear region of the plot. The computed exponent values agree with the known analytical results. These exponents have been obtained for different values of De between zero and one. The exponent of the power law depends on the angle θ. For our simulations, the power law behavior exists only for r between $1\text{x}10^{-2}$ and 0.2. For $r < 1.0\text{E-}3$, the solution reaches a constant value and for $r > 0.2$ the solution reaches value appropriate for the global flow.

The numerical results for the entire flow were also calculated along with the corner region. The pressure drop decreases evenly as the fluid passes through the domain. The pressure drop per unit length in the downstream narrower channel is smaller than in the upstream channel. The pressure drop is also large in the transition region where the flow area is suddenly decreased. Isovalues of $\mathrm{tr}\underline{\underline{A}}$ show that the polymeric material elements downstream of the corner are relatively more stretched which is a consequence of the hyperbolic nature of the constitutive equation.

CHAPTER 7

NUMERICAL STUDIES OF BOUNDARY LAYER CONTROL

7.1 Introduction

The most common use of the airfoils is in airplanes for generating the lift force, which allows them to remain suspended in the air. The other applications include propellers for airplanes and ships.

The performance of an airfoil depends on its shape, the angle of attack, and air speed. The airfoil stalls when the angle of attack is too large as the boundary layer on the upper surface separates. The focus of this work is to numerically study the separation process and to control the separation by injecting and sucking fluid on the upper surface.

In recent years, numerical methods have matured to an extent that it is possible to numerically study flow around the airfoils and wings. Advances in computer technology allow us to these numerical solutions in complicated domains in less computational time than before. These numerical studies can complement a large number of experimental studies that have been done to understand the boundary layer separation process and to use this understanding to prevent the separation of the boundary layer at large Reynolds numbers and at large angles of attacks.

The force acting on an airfoil can be decomposed into a lift force, which acts normal to the fluid velocity, and a drag force, which acts in the same direction as the fluid velocity. In most applications the drag is undesirable and the lift force should be as large as possible. The lift and drag forces are used to quantify the performance of an airfoil under given flow conditions.

In the past, both analytical and numerical methods have been used to study the airfoil problem. Analytically, due to the high Reynolds number involved and the complexity of flow domain, most studies assume that the fluid is inviscid. These inviscid solutions provide useful information about the lift. But the inviscid flows cannot be used to obtain the drag acting on the airfoil or the angle of attack at which the flow separates.

As noted before, when the boundary layer separates over the top surface of the airfoil there is a large increase in drag and the lift essentially reduces to zero. The boundary layer separates because the fluid momentum inside the boundary layer goes to zero. In simulations, the separation of the boundary layer can be noticed for an angle of attack of 15^{o}. The separation of the boundary layer becomes more noticeable when for a fixed value of angle of attack the Reynolds number (Re) is increased.

Also when the boundary layer separates, the fluid flow creates vortex shedding which consequently makes the airfoil vibrate. These vibrations can be avoided or reduced by preventing the separation of the boundary layer. The efforts of controlling the boundary layer have started many years ago. It is presumed that these efforts were triggered by the tests made by Prandtl, in the early 1900s. The first report published in the U.S. is by E. G. Reid and M. J. Bamber on the National Advisory Committee for Aeronautics (N.A.C.A.) was in 1928. They reported the results of experiments using both suction and blowing type boundary layer control on the U.S.A.-27 airfoil. These tests showed clearly the effectiveness of boundary layer control for improving maximum lift.

There are many airfoils designed to meet requirements for different applications. NACA developed a nomenclature for classifying these airfoils and tested their

performance by doing extensive wind tunnel testing. In this study, the NACA 0012-64 airfoil--which is a high performance airfoil--is used, see Figure 7.1.

Figure 7.2 shows the development of boundary layer on a surface. The fluid is flowing tangentially to the surface from left to right. The fluid velocity on the flat surface is zero and reaches the free stream value at a small distance δ away from the surface, where δ is called the boundary layer thickness. The fluid particles near the surface are retarded by friction. If the pressure gradient increases downstream, there is an additional retarding effect due to this cause. The fluid near to the surface may have insufficient momentum (which is an extension of Newton's law of motion), for it to continue its motion and so the fluid will be brought to rest at point P, see Figure 7.2.

Further downstream from this point, the adverse gradient will push the fluid near to the surface upstream and there will be a reverse flow. Therefore, the point P at separation divides the region near to the surface into two regions: the first where the fluid is moving upstream and the second where the velocity is downstream.

An example in which the separation of the boundary layer needs to be prevented is in the case of a quick maneuver required from a fighter aircraft, where the angle of attack is suddenly increased in order to change its velocity or direction. This rapid change in the angle of attack will lead towards the separation of the boundary layer and stall may occur. When the flow separates, the drag force increases and the lift force decreases. The airfoil eventually stalls when either the angle of attack or Re is increased.

The boundary layer may be laminar and turbulent. Turbulent boundary layer there is enhanced mixing which results in momentum continually brought to the surface. It also causes the retarded fluid near the surface to be carried to the fluid outside of the boundary

layer, thereby gaining momentum. As a result the fluid in a turbulent boundary layer is not slowed down so much as in a laminar layer, and can travel further against an adverse pressure gradient before being brought to rest. Therefore the separation point of a turbulent boundary layer is further downstream than that of a laminar layer.

The method used for preventing the separation of the boundary layer in this study is by injecting and sucking fluid on the top surface of the airfoil. This injection and suction of fluid affects the fluid flow close to the top surface of the airfoil. Injection of fluid at a large velocity provides additional momentum to the boundary layer which can delay the separation of the boundary layer. Suction of the slowly moving fluid, on the other hand, allows the fluid outside the boundary layer to enter inside the boundary layer and thus there is a net increase in the boundary layer momentum.

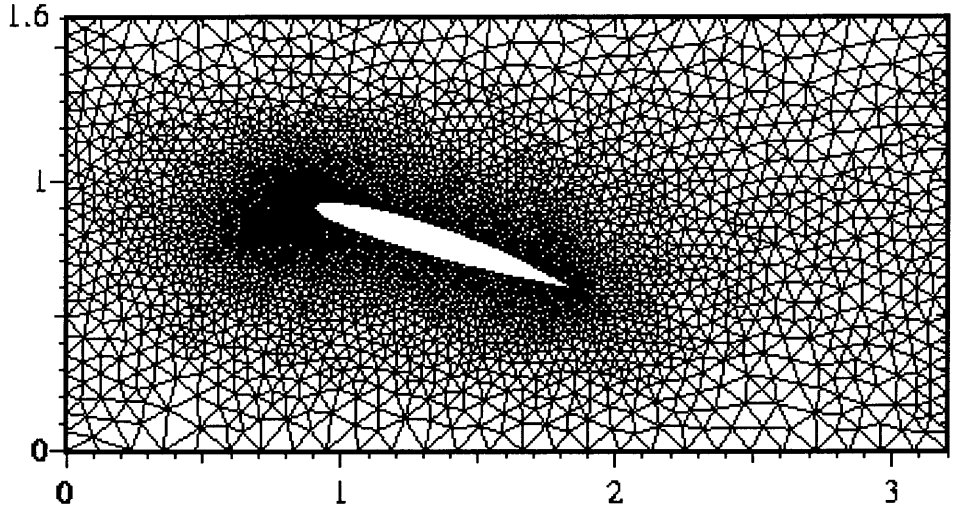

Figure 7.1. Finite element mesh on the airfoil, angle of attack 18°.

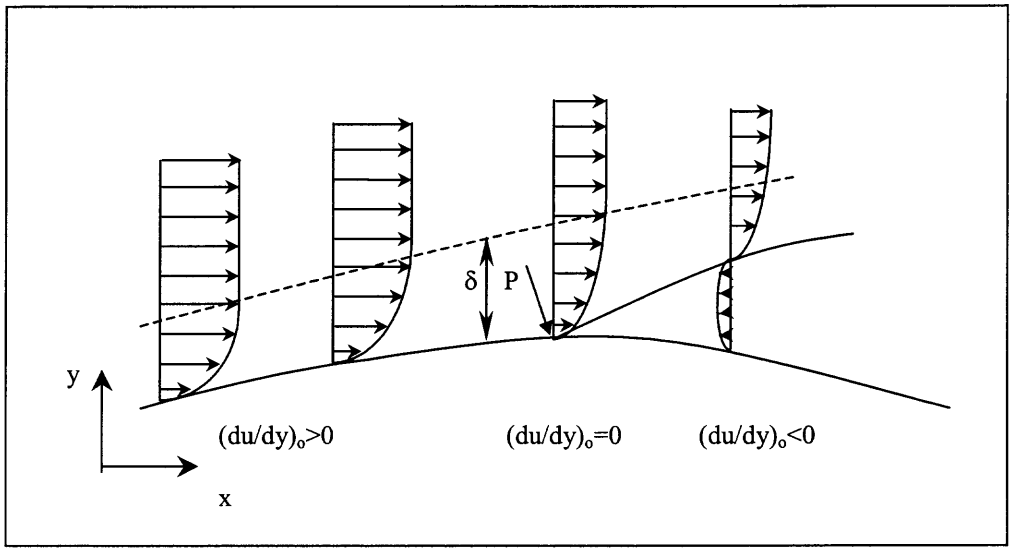

Figure 7.2 Two-dimensional separation of the boundary layer.

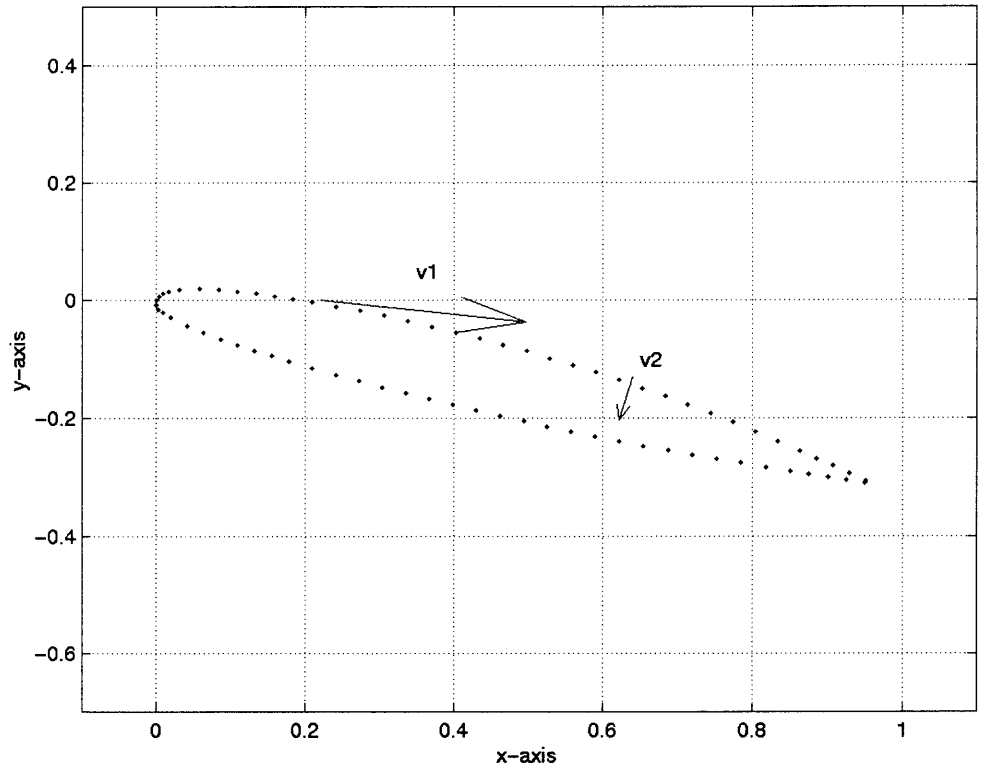

Figure 7.3 Injection and suction velocities in the airfoil, angle of attack 18°.

7.2 Two Dimensional Flow with Injection and Suction Over the Airfoil

In order to prevent the separation of the boundary layer in this two-dimensional study, the fluid was tangentially injected with velocity v1 into the main fluid flow near the leading edge of the airfoil. The injection point is selected close to the point where the separation is likely to occur. The optimal position of course depends on Re and the angle of attack.

In order to satisfy the mass conservation in the flow domain, the fluid is sucked with velocity v2, close to the trailing edge as shown in Figure 7.3. By assuming that the mass flow rates of injection and suction are the same, it is ensured that there is no source/sink of fluid inside of the airfoil. The orifices from where the fluid is sucked or injected are approximately twenty times smaller than the chord.

Different angles of attack were used in the range from 0^{o} to 40^{o}. The separation point depends on the angle of attack used, and also on the Reynolds number Re. In this investigation the angle of attack was fixed to be 18^{o} and only the Reynolds number was varied.

The injection velocity v1, which is the velocity near the leading edge, makes an angle of 4^{o} to the upper surface, and thus it is approximately tangential to the top surface of the airfoil. The magnitude of v1 is 2.9 or 5.8.

The FEM (finite element method) is used to mesh the rectangular shaped domain around the airfoil (see Figure 7.1). The height of domain used in simulations is 1.6 and the length is 3.2. The incoming velocity as well the velocity on the upper and lower domain surfaces is assumed to be one. The traction free boundary condition is applied at the domain exit.

7.3 Results

As already mentioned, the goal of this study is to delay the point of separation on the boundary layer or to avoid separation altogether. The Reynolds number is assumed to be 100, 200, 500 or 1000. The velocity v1 used for fluid injection and suction over the airfoil is varied between 2.9 and 8.7.

Simulations show that when there is no suction or injection, for the angle of attack of 10^{o} the vortex shedding starts for Re = 500. The size of the vortex bubble in this case is relatively small and it is located close to the trailing edge. For higher values of the angle of attack, the size of vortex bubble grows and the separation point moves towards the leading edge. When the separation occurs at a point close to the leading edge the airfoil stalls in the sense that the lift force acting on the airfoil falls dramatically. This can be seen clearly for an angle of attack of 18^{o}, see Figure 7.4. Numerically simulations also show that for a fixed angle of attack, the vortex bubble size increases with increasing Re which can be seen in Figures 7.4 and 7.5

Figures 7.6, 7.7 and 7.8 show the effect of varying the injection velocity and suction velocity on the size of the wake bubble. For the three cases shown in these figures, Re is fixed at 100, but the suction velocity is varied. The suction velocity is 2.9, 5.8 or 8.7. From these figures, it can be inferred that when v1 is increased the position of the separation point moves downstream. This is an important result because it implies that for a given Re and angle of attack, it may be possible to avoid separation by increasing injection or suction velocities. Also, from these figures, it can be seen that the position of the orifice where the suction takes place is also important. The separation is also delayed by moving the suction point closer to the airfoil trailing edge.

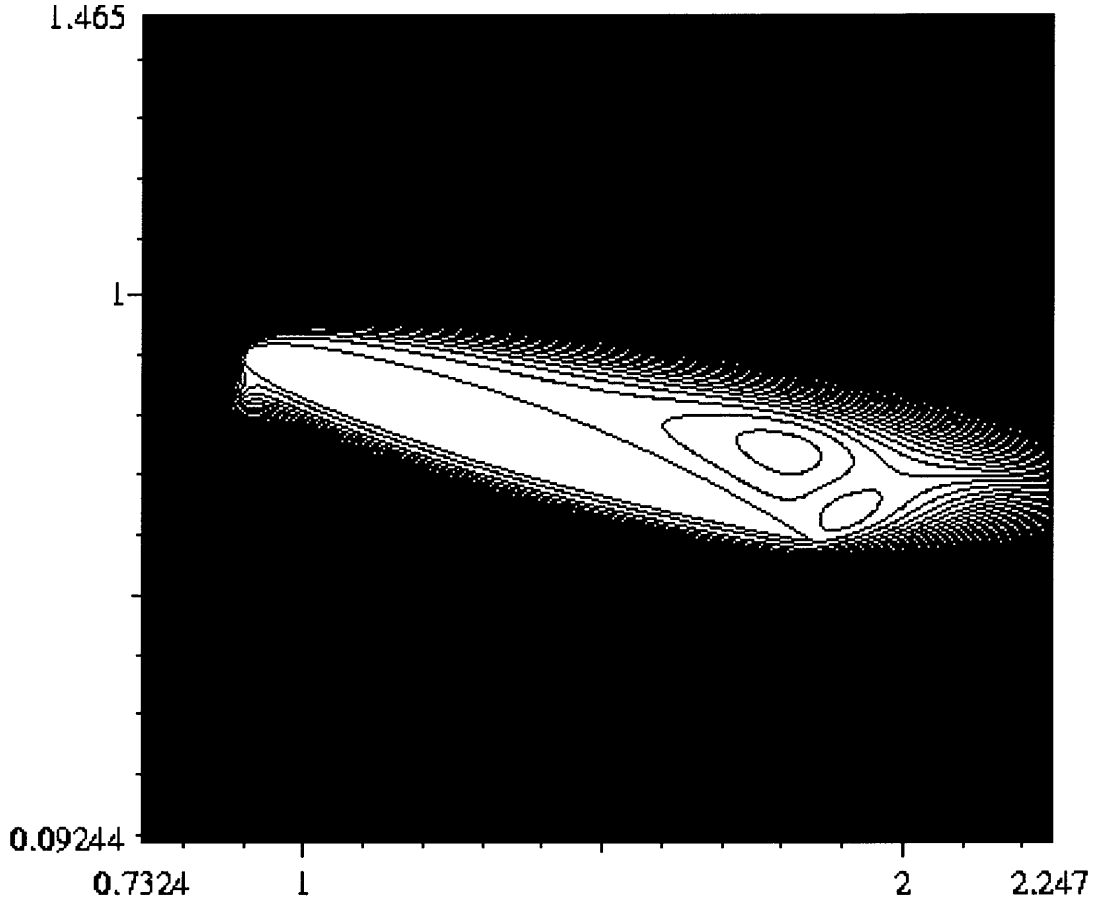

Figure 7.4 Streamlines for flow past an airfoil. The angle of attack is 18° and Re=100. The boundary layer separation point is near the leading edge. Also notice its relatively large sized wake bubble on the airfoil upper surface.

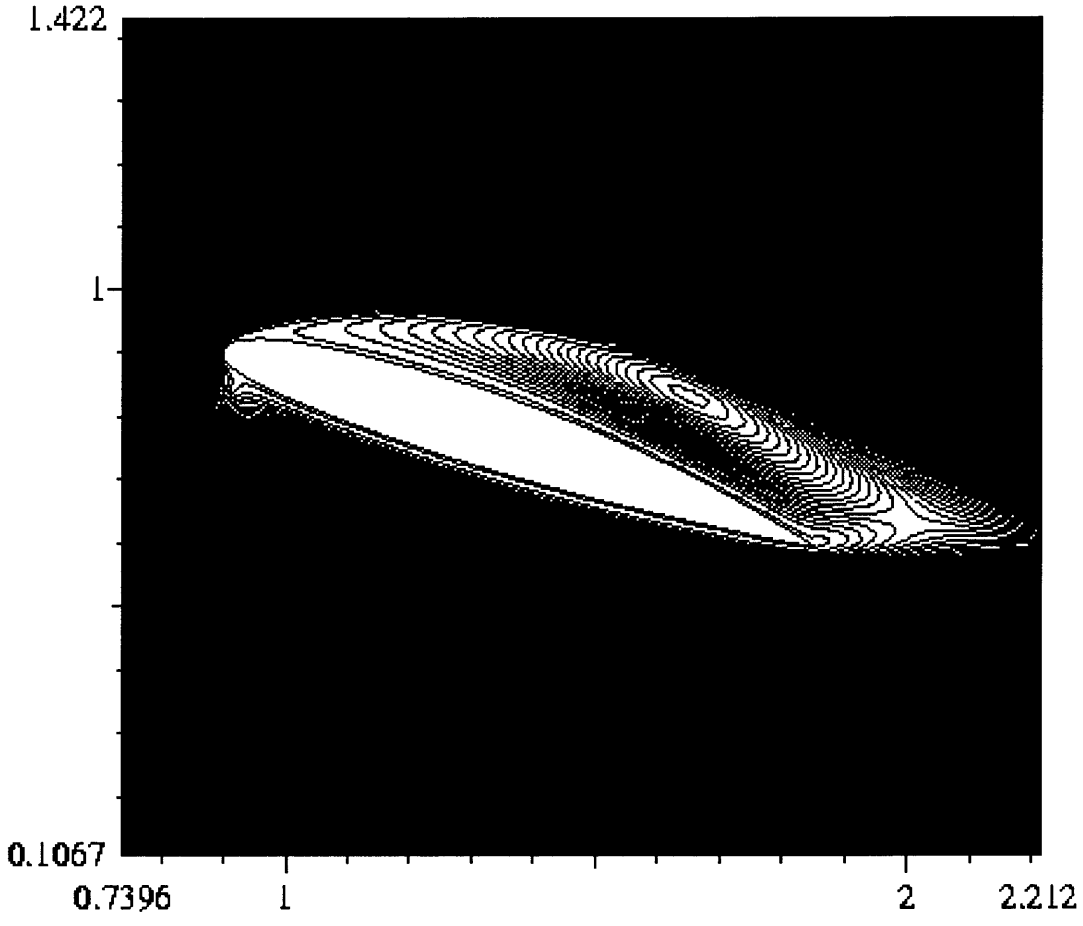

Figure 7.5 Streamlines for flow past an airfoil. The angle of attack is 18° and Re=500. The boundary layer separation point is near the leading edge. Also notice its relatively large sized wake bubble on the airfoil upper surface.

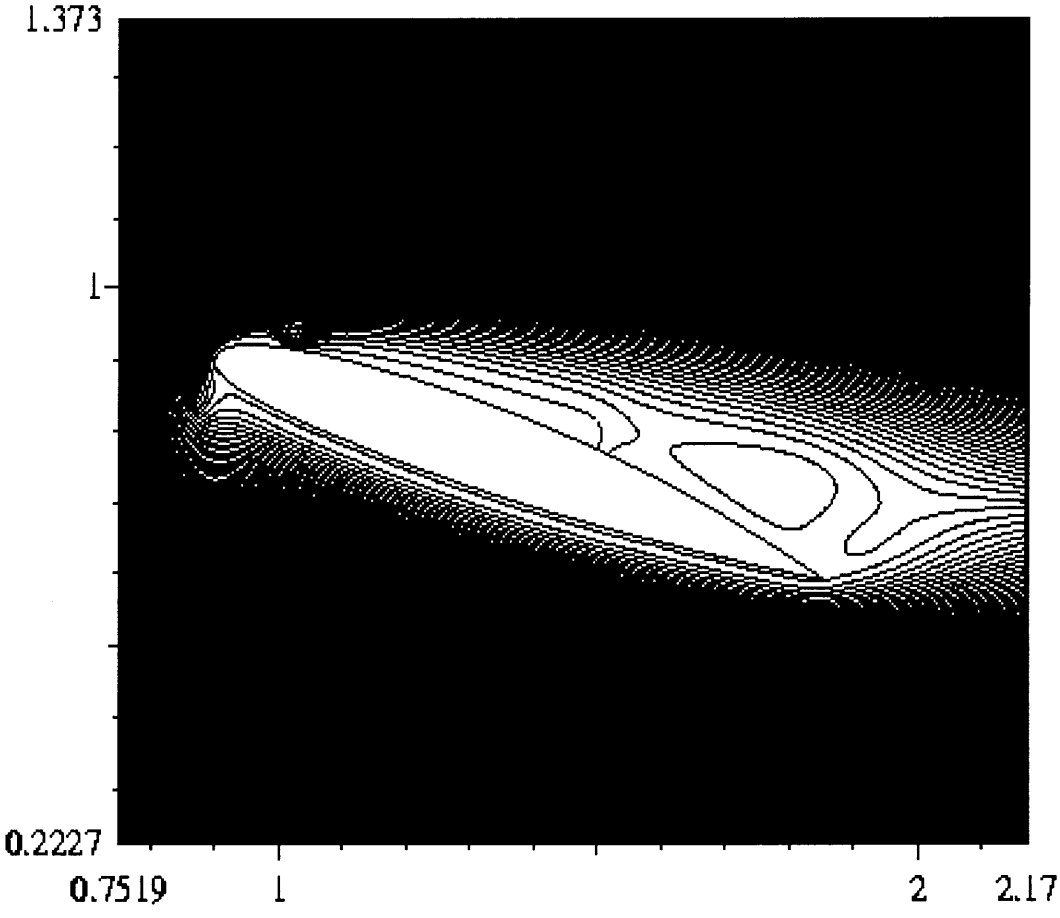

Figure 7.6 Streamlines for fluid flow past an airfoil with injection and suction. The angle of attack 18°, Re=100, v1=2.9. Notice that the wake bubble size is much smaller than for the case without suction and injection shown in Figure 7.4.

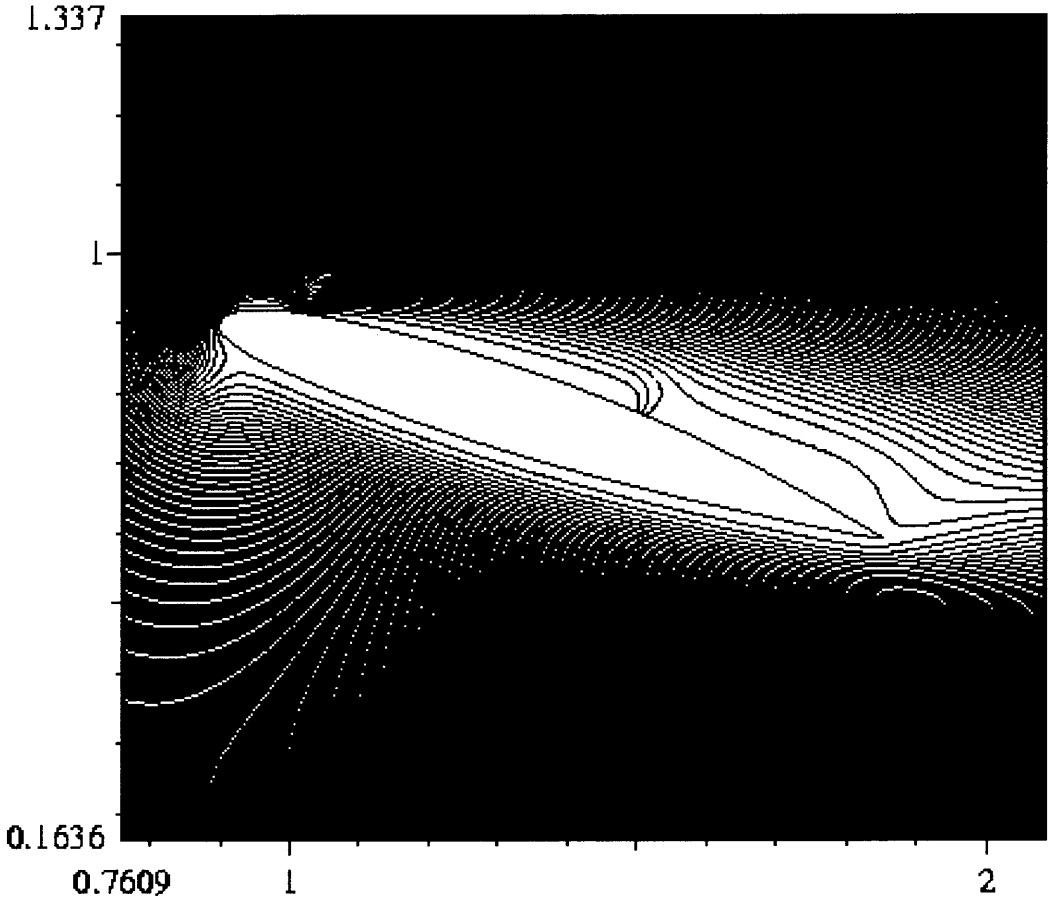

Figure 7.7 Streamlines for fluid flow past an airfoil with injection and suction. The angle of attack 18°, Re=100, v1=5.8. Notice that the wake bubble size is much smaller than for the case without suction and injection shown in Figure 7.4.

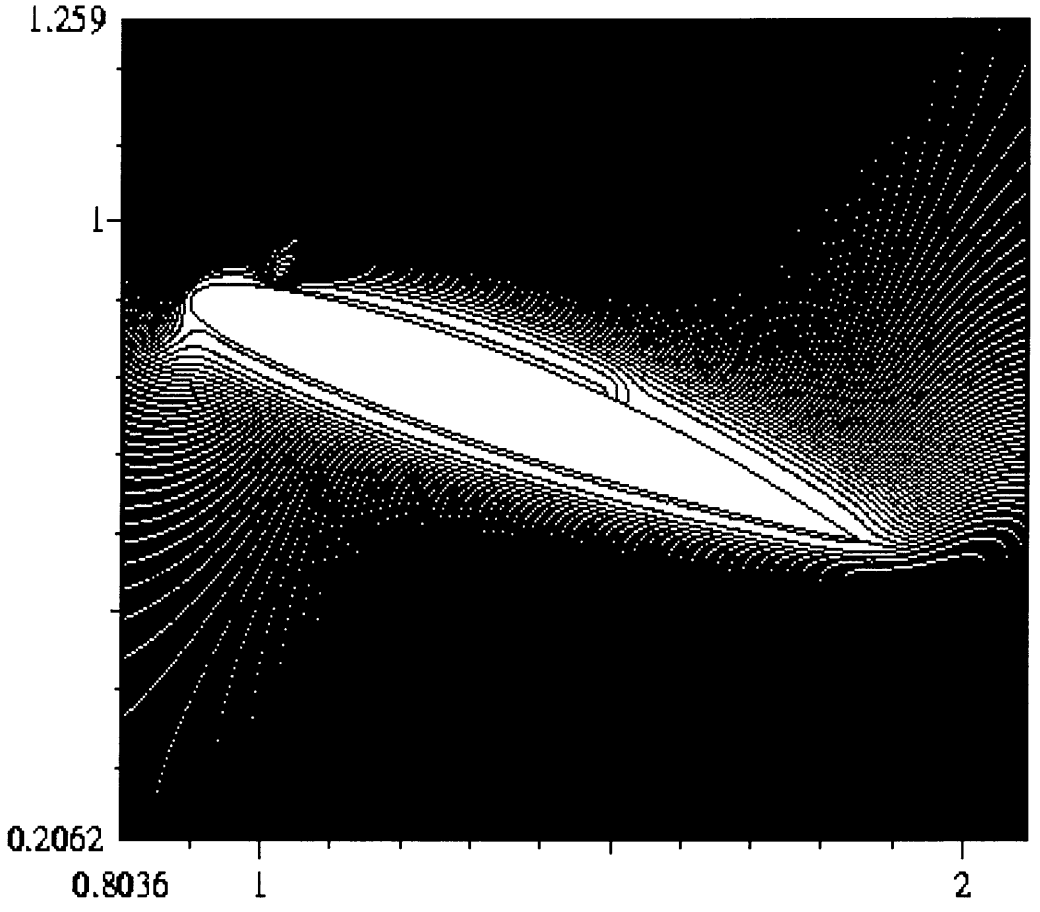

Figure 7.8 Streamlines for fluid flow past an airfoil with injection and suction. The angle of attack 18°, Re=100, v1=8.7. Notice that the wake bubble size is much smaller than for the case without suction and injection shown in Figure 7.4.

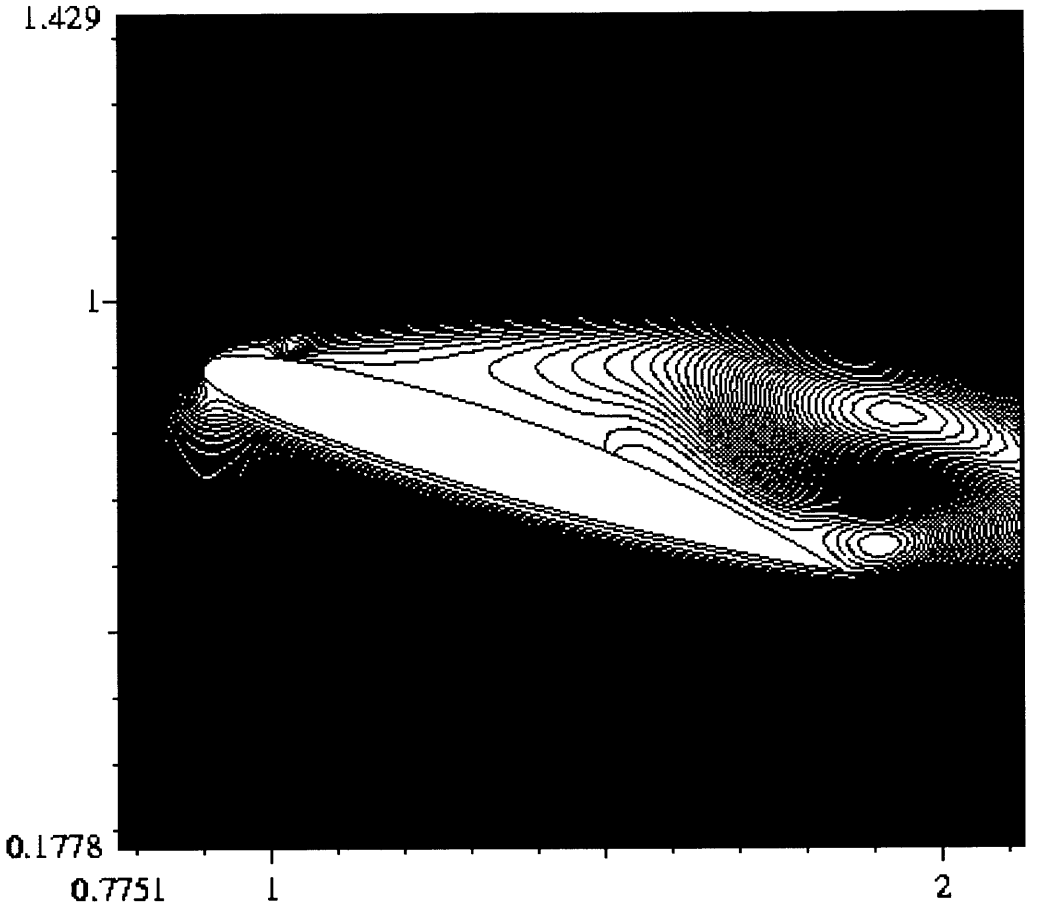

Figure 7.9 Streamlines for fluid flow past an airfoil with injection and suction. The angle of attack 18°, Re=500, v1=2.9. Notice that the wake bubble size is much smaller than for the case without suction and injection shown in Figure 7.5.

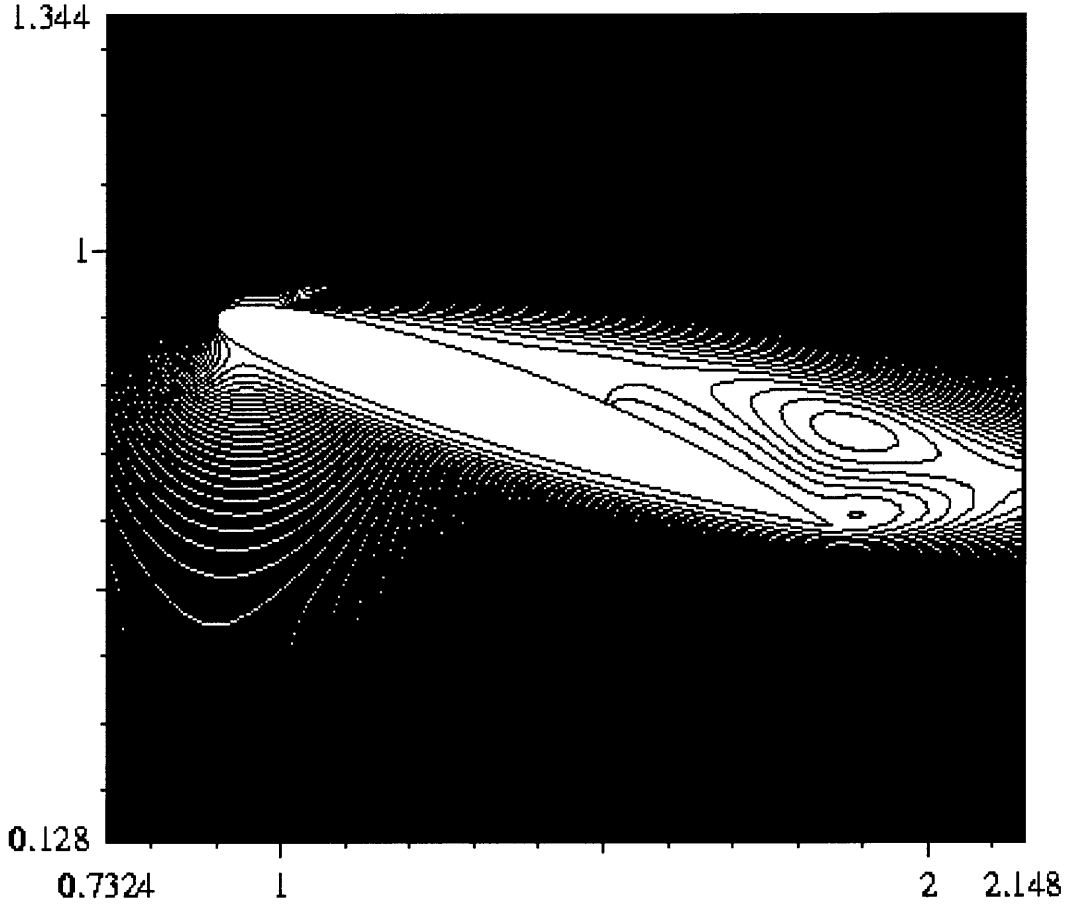

Figure 7.10 Streamlines for fluid flow past an airfoil with injection and suction. The angle of attack 18°, Re=500, v1=5.8. Notice that the wake bubble size is much smaller than for the case without suction and injection shown in Figure 7.5.

Next, the variation of the lift and drag coefficients with the angle of attack is described. First, the drag and lift acting on airfoil are defined as:

$$\text{Lift} = \int_{\Gamma} (\underline{\underline{\sigma}} \cdot \hat{n}) \cdot \hat{j} ds$$

$$\text{Drag} = \int_{\Gamma} (\underline{\underline{\sigma}} \cdot \hat{n}) \cdot \hat{i} ds$$

where σ is the stress tensor, **n** is the outer normal to the surface, ds is an infinitesimal surface element, the unit vector **i** points in the flow direction and **j** is perpendicular to the flow direction. The drag and lift coefficients are defined as

$$\text{Drag coefficient:} \qquad C_D = \frac{\text{Drag}}{\frac{1}{2}\rho U^2 (\text{Chord})}$$

$$\text{Lift coefficient:} \qquad C_L = \frac{\text{Lift}}{\frac{1}{2}\rho U^2 (\text{Chord})}$$

In this study for Re = 100, 200, or 500 the variation of the lift and drag coefficients with the injection/suction speed is also studied. In Figures 7.11, 7.12 and 7.13, the lift and drag coefficients for the case without suction/injection are shown. In Figures 7.14, 7.15, 7.16, 7.17, 7.18 and 7.19, the injection speeds are 2.9 and 5.8. The injection is at the leading edge and the suction at the trailing edge as shown in Figure 7.3.

Figures 7.11 to 7.19 show the effect of varying the angle of attack on the lift and drag coefficients. As expected, the lift increases with the angle of attack. The lift coefficient reaches its maximum value at approximately 40° at which the airfoil stalls. The drag coefficient also increases with the angle of attack, and the rate of increase is especially large near the stall angle. The drag coefficient also decreases when the Re is increased, which indicates that the viscous contribution to the drag is not negligible.

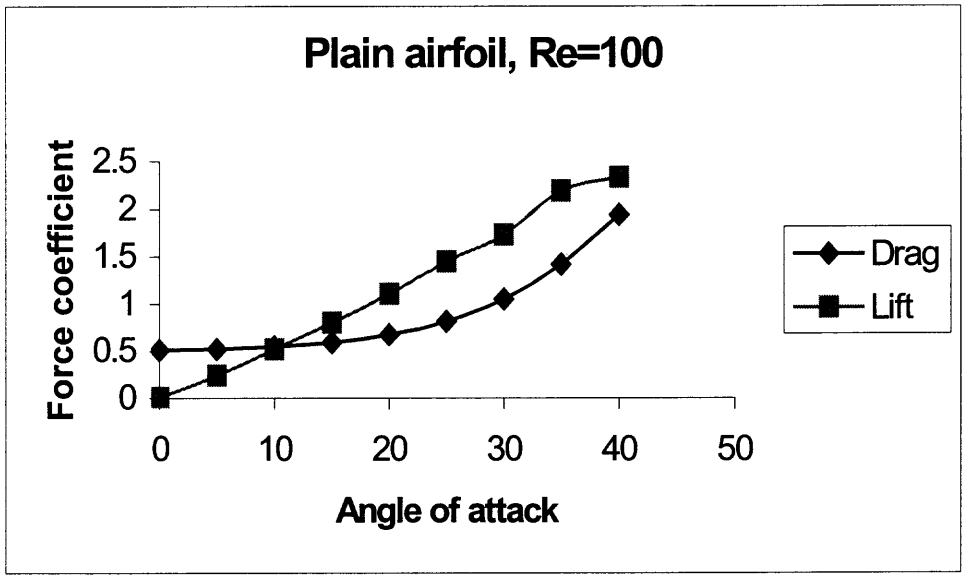

Figure 7.11 The Drag and lift coefficients for Re = 100, are shown as a function of angle of attack. There is no injection/suction in this case.

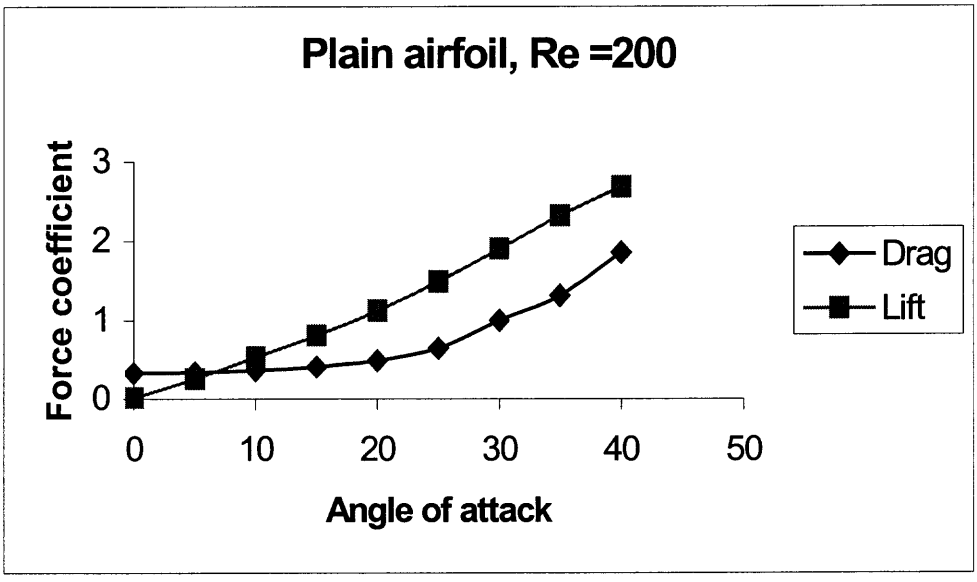

Figure 7.12 The Drag and lift coefficients for Re = 200, are shown as a function of angle of attack. There is no injection/suction in this case.

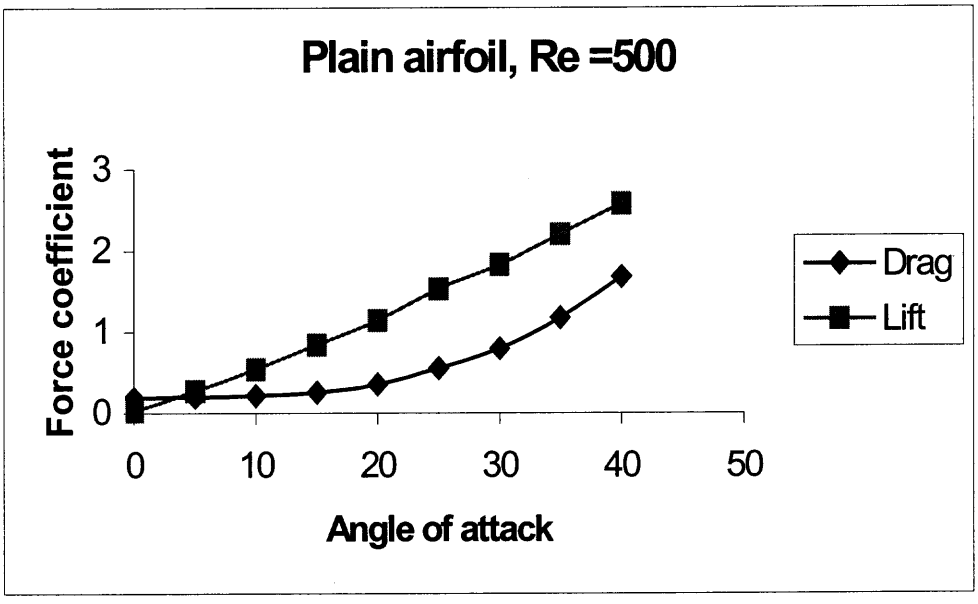

Figure 7.13 The Drag and lift coefficients for Re = 500, are shown as a function of angle of attack. There is no injection/suction in this case.

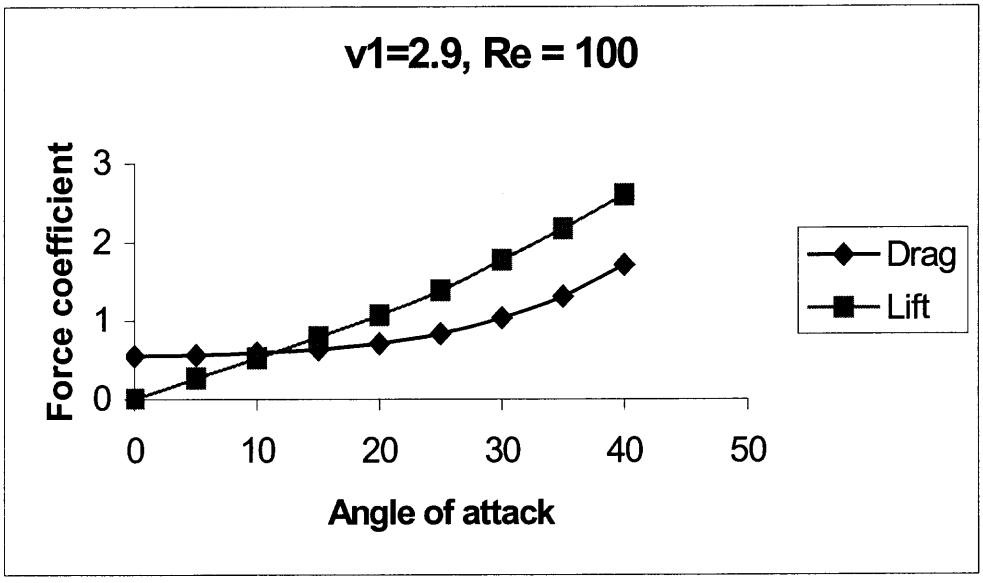

Figure 7.14 The Drag and lift coefficients are shown as a function of angle of attack. Re = 100 and the injection velocity v1 = 2.9.

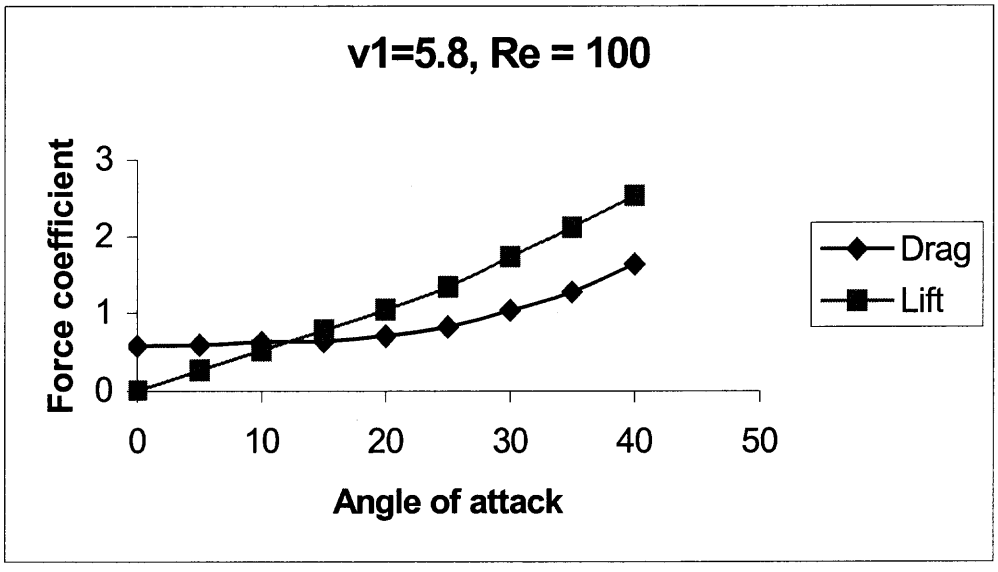

Figure 7.15 The Drag and lift coefficients are shown as a function of angle of attack. Re = 100 and the injection velocity v1 = 5.8.

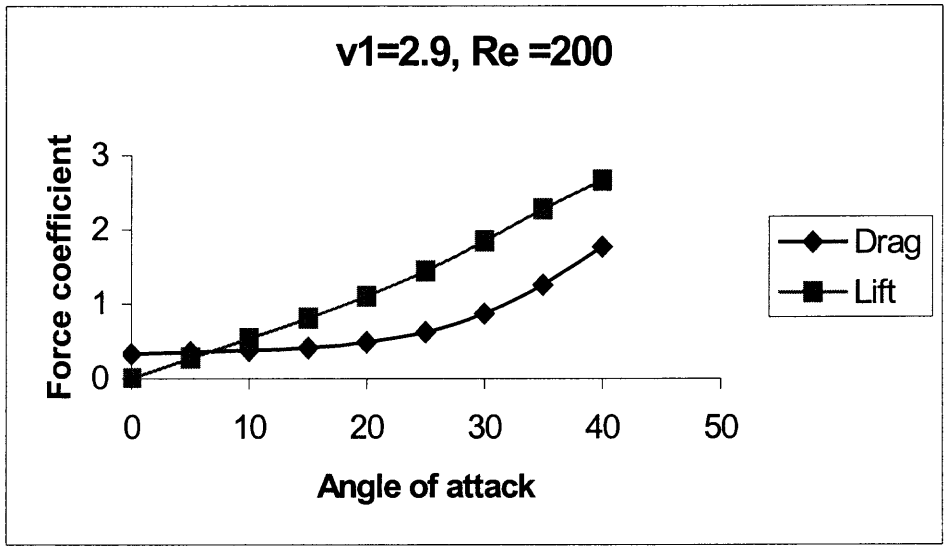

Figure 7.16 The Drag and lift coefficients are shown as a function of angle of attack. Re = 200 and the injection velocity v1 = 2.9.

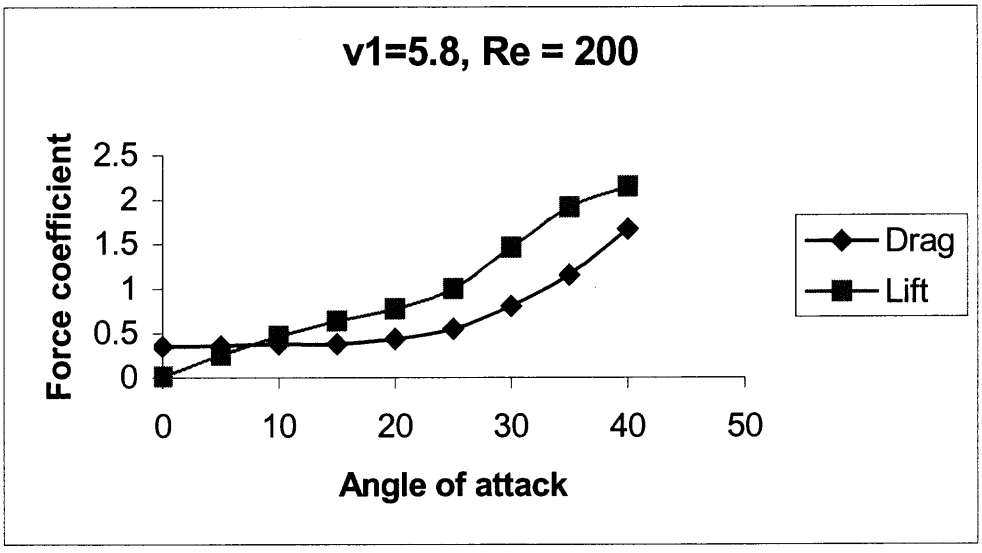

Figure 7.17 The Drag and lift coefficients are shown as a function of angle of attack. Re = 200 and the injection velocity v1 = 5.8.

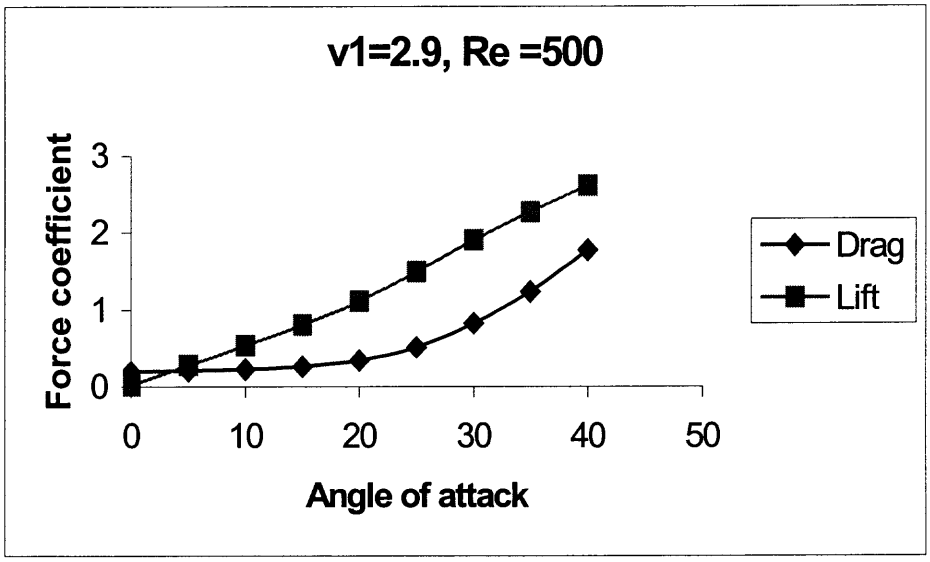

Figure 7.18 The Drag and lift coefficients are shown as a function of angle of attack. Re = 500 and the injection velocity v1 = 2.9.

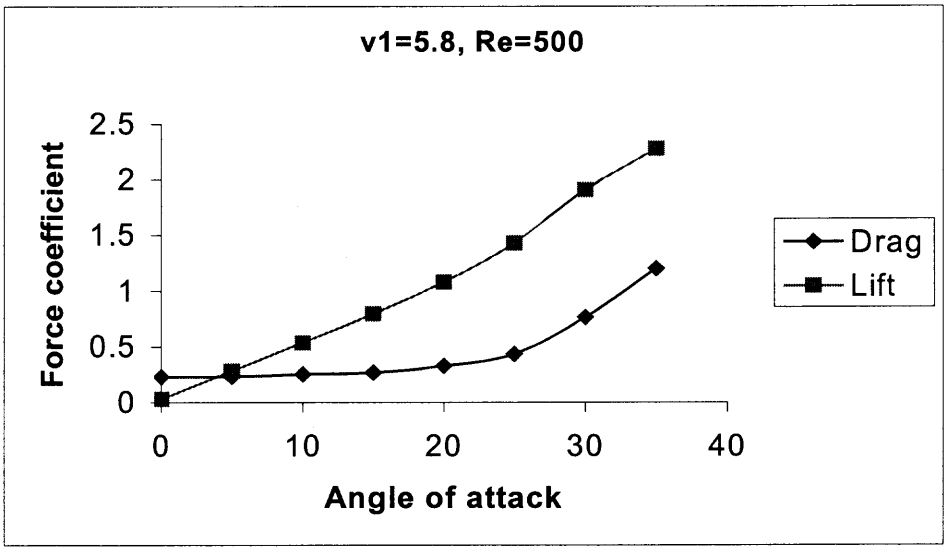

Figure 7.19 The Drag and lift coefficients are shown as a function of angle of attack. Re = 500 and the injection velocity v1 = 5.8.

Figures 7.20, 7.21 and 7.22 show that the viscous contribution to the drag decreases with increasing angle of attack and the viscous contribution to lift increases with increasing angle of attack. In order to understand role of the rate of suction and injection, the changes in the pressure and viscous contribution to the lift and drag were studied when the suction velocity is changed. Changes in both the lift and drag are small but significant. The pressure contribution to drag on the other hand increases slowly with the angle of attack until certain value of angle of attack for which the pressure drag starts increasing rapidly. The pressure contribution to lift increases almost linearly with the angle of attack.

Figures 7.23, 7.25 and 7.27 show the drag coefficients for different values of Re, and the Figures 7.24, 7.26 and 7.28 show the lift coefficients. The drag coefficient increases significantly when the angle of attack is relatively large. For smaller angle of attack the drag coefficient increases slowly until the angle of attack reaches a value for which the drag coefficient starts increasing rapidly. The drag coefficient also slightly decreases when the Re increases. The lift coefficient on the other hand varies almost linearly with increasing angle of attack for all the cases. According to the figures, there is a small increase in the lift coefficient value when injection and suction occurs on the airfoil.

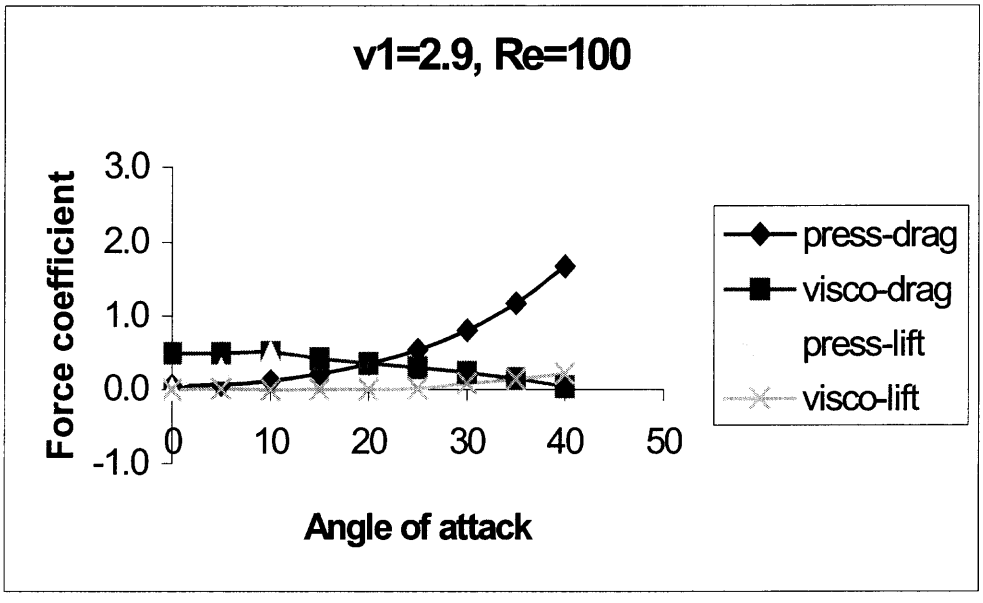

Figure 7.20 Pressure and viscous forces vs. the angle of attack for an airfoil with suction and injection over the surface v1=2.9, and Re = 100.

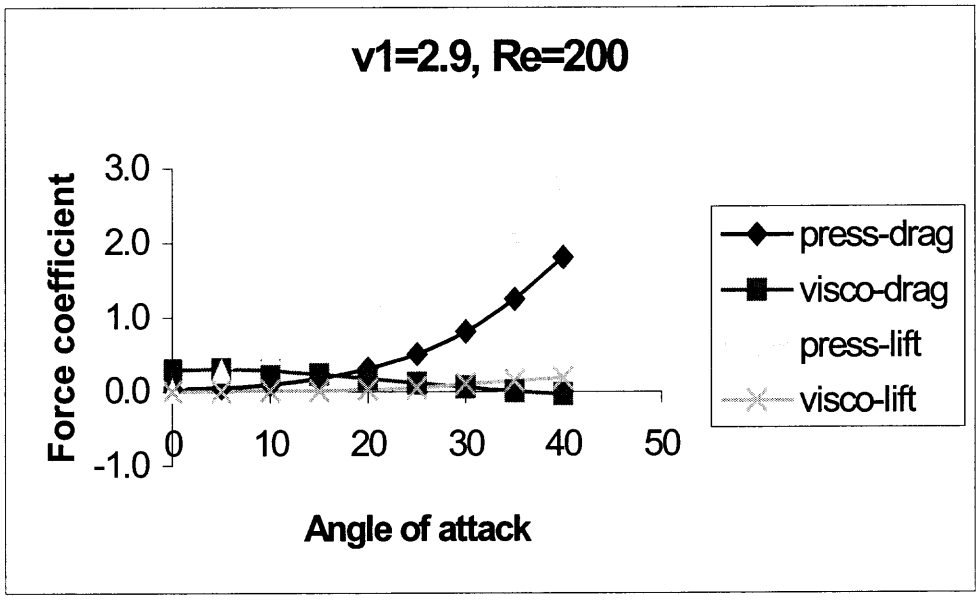

Figure 7.21 Pressure and viscous forces vs. the angle of attack for an airfoil with suction and injection over the surface v1=2.9, and Re = 200.

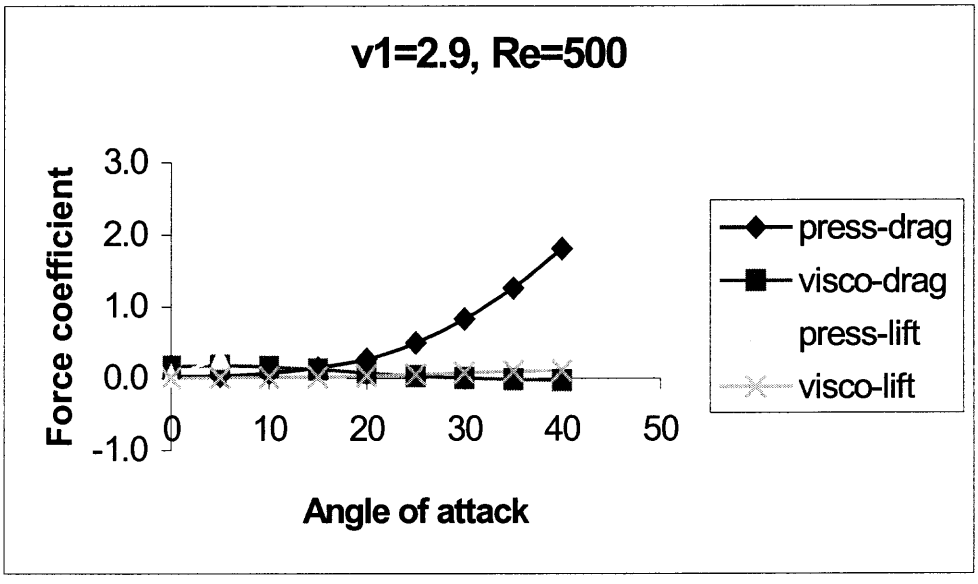

Figure 7.22 Pressure and viscous forces vs. the angle of attack for an airfoil with suction and injection over the surface v1=2.9, and Re = 500.

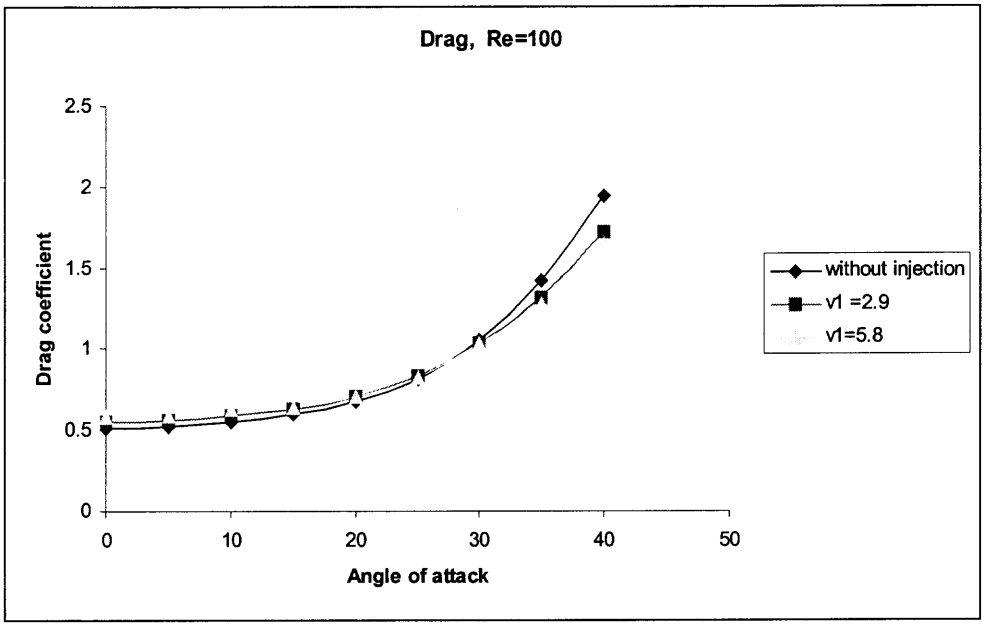

Figure 7.23 The drag coefficient on the airfoil for both cases with and without injection/suction, Re =100.

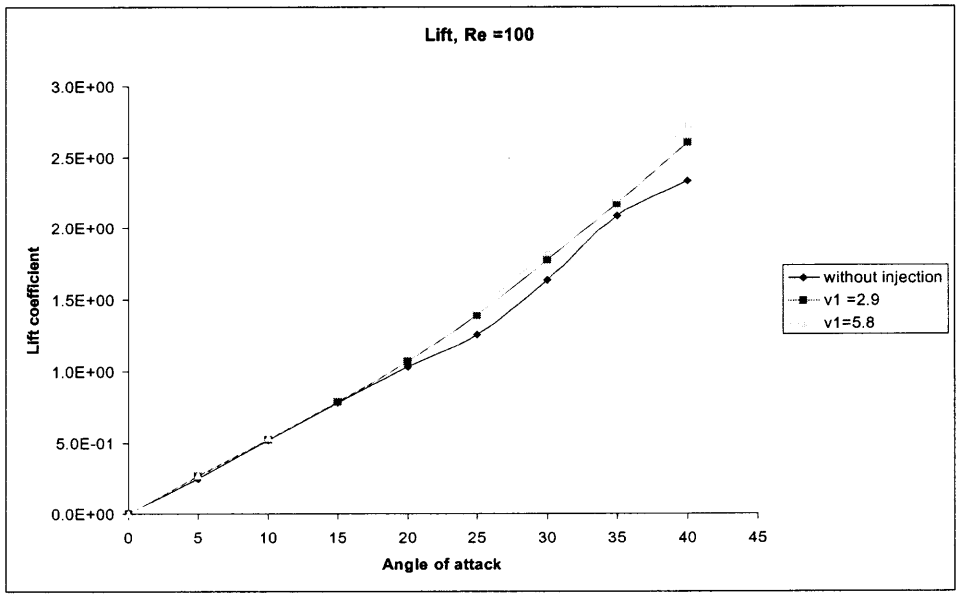

Figure 7.24 The lift coefficient on the airfoil for both cases with and without injection/suction, Re =100.

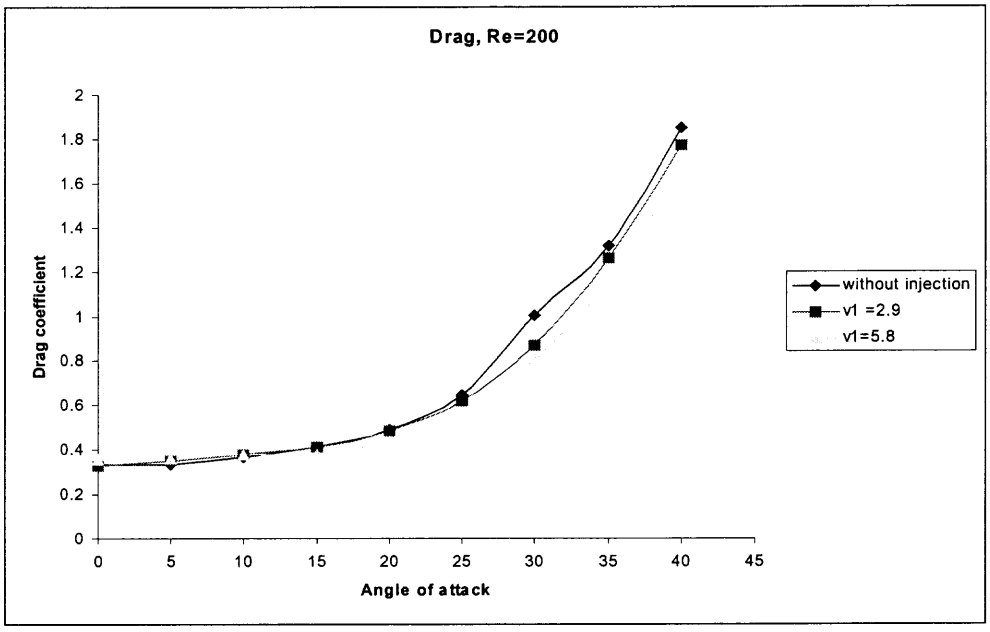

Figure 7.25 The drag coefficient on the airfoil for both cases with and without injection/suction, Re =200.

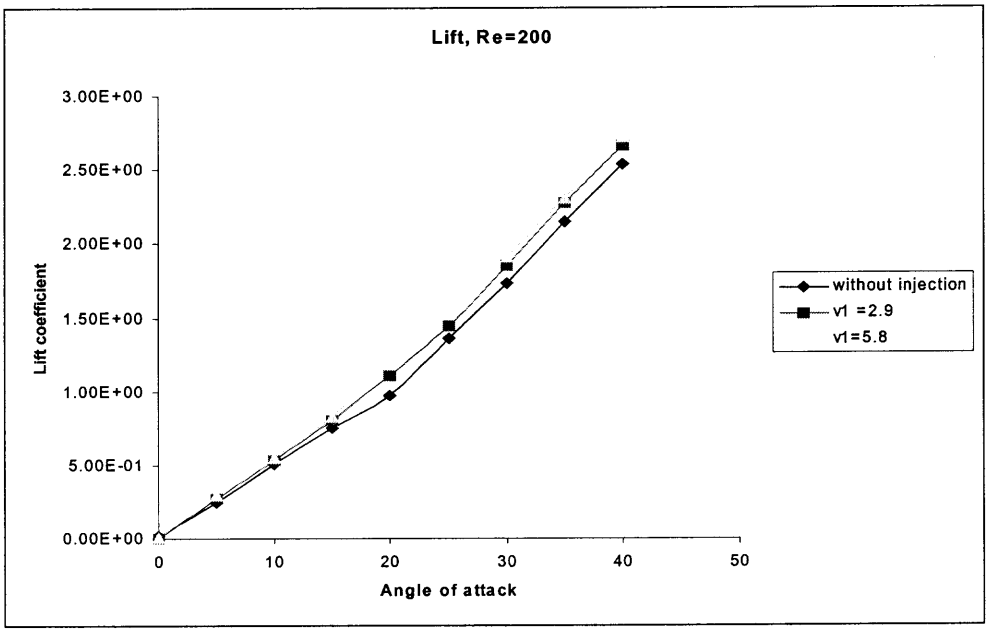

Figure 7.26 The lift coefficient on the airfoil for both cases with and without injection/suction, Re =200.

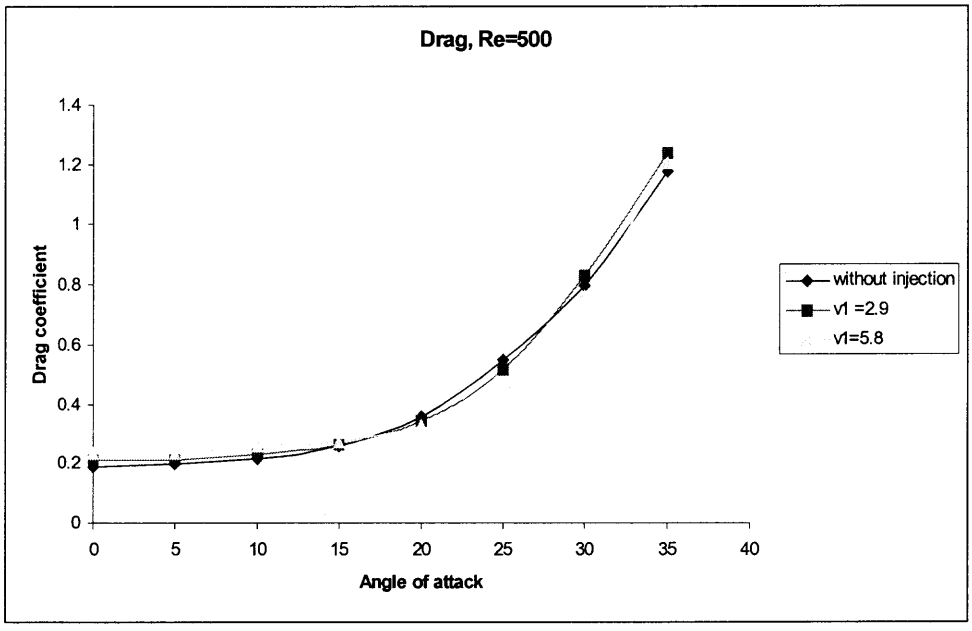

Figure 7.27 The drag coefficient on the airfoil for both cases with and without injection/suction, Re =500.

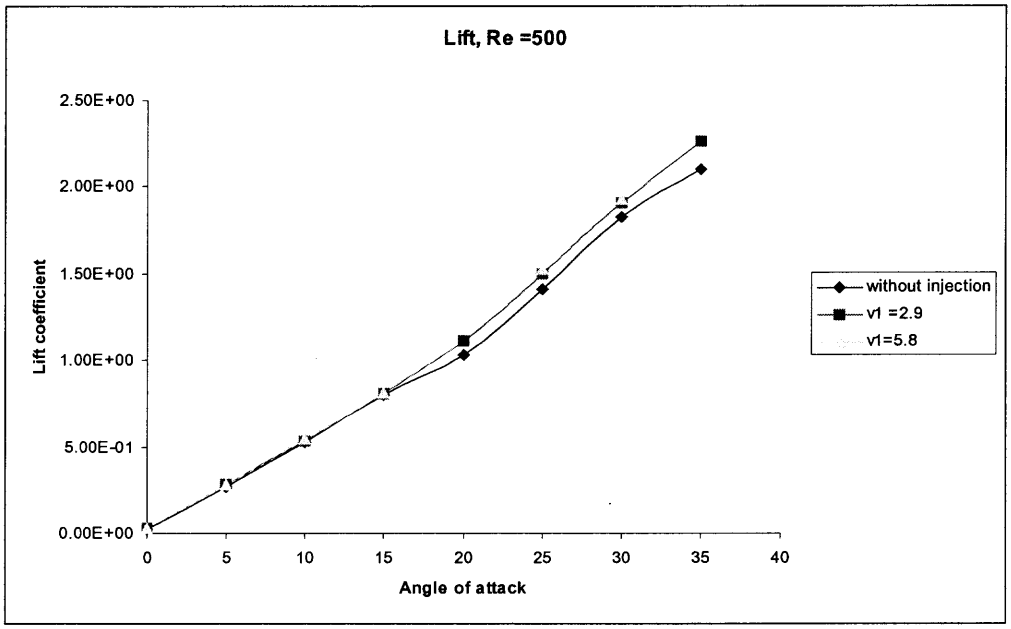

Figure 7.28 The lift coefficient on the airfoil for both cases with and without injection/suction, Re =500.

7.4 Summary

The numerical results show that the boundary layer separation on the upper surface of the airfoil which happens at large values of angle of attack and Re can be delayed by injection and sucking fluid on the upper surface. The injection point is close to the leading edge and the suction point is close to the trailing edge.

The suction/injection velocity required for avoiding boundary layer separation increases with increasing angle of attack and also with an increase in Re. The pressure drag decreases when the boundary layer separation is avoided but the viscous drag increases. The pressure contribution to lift also increases when the boundary layer separation is avoided.

REFERENCES

1. Abbott, I. H., and Von Doenhoff, A. E. (1959) *Theory of Wing Sections.* Dover publications, New York.

2. Alcocer, F. J., Kumar, V., and Singh, P. (1999) Permeability of periodic porous media, *Physical Review E* 59, 711-714.

3. Apelian, M. R., Armstrong, R. C., and Brown, R. A. (1988) Impact of the constitutive equation and singularity on the calculation of stick-slip flow: Modified upper-convected Maxwell model (MUCM), *Journal of Non-Newtonian Fluid Mechanics* 42, 141-188.

4. Astarita, G. (1979) Objective and generally applicable criteria for flow classification, *Journal of Non-Newtonian Fluid Mechanics* 6, 69-76.

5. Bear, J. (1972) *Dynamics of Fluids in Porous Media,* Elsevier, New York.

6. Bird, R. B., Hassager, O., Armstrong, R. C., and Curtiss, C. F. (1977) *Dynamics of Polymeric Liquids*, Vol. 2, Wiley, New York.

7. Bird, R. B., Stewart, W. E., and Lightfoot, E. N. (1976) *Transport phenomena*, Wiley, New York.

8. Bristeau, M. O., Glowisnki, R., and Periaux, J. (1987) Numerical methods for the Navier-Stokes equations. Applications to the simulation of compressible and incompressible flows. *Computer Physics Reports*.6, 73-187

9. Brooks, A. N., and Hughes, T. J. R. (1982) Streamline upwind/Petrov-Galerkin formulation for convection dominated flows with particular emphasis on the incompressible Navier-Stokes equations. *Computer Methods in Applied Mechanics and Engineering* 32, 199-259.

10. Burdette, S. R., Coates, P. J., Armstrong, R. C., and Brown, R. A. (1989) Calculations of viscoelastic flow through an axisymmetric corrugated tube using the explicitly elliptic momentum equation. *Journal of Non-Newtonian Fluid Mechanics* 33, 1-23.

11. Chen, C. L., Chow, C. Y., Van Dalsem, R. W. R., and Holst, T. L. (1989) Computation of viscous transonic flow over porous airfoils, *AIAA Journal,* vol. 26, 1067-1074.

12. Chilcott, M. D., and Rallison, J. M. (1988) Creeping flow of dilute polymer solutions past cylinders and spheres. *Journal of Non-Newtonian Fluid Mechanics* 29, 381-432.

13. Coates, P. J., Armstrong, R. C., and Brown (1988) Calculation of the steady state viscoelastic flow through and axisymmetric contraction with the EEME formulation, *Journal of Non-Newtonian Fluid Mechanics* 27, 299-321.

14. Davis, A. P., and Devlin, J. (1993) On corner flows of Oldroyd-B fluids. *Journal of Non-Newtonian Fluid Mechanics* 50, 173-191.

15. Dean, W. R., and Montagnon, P. E. (1949) *Proceedings of the Cambridge Philosophical Society* 45, 389-394.

16. Drummond, J. E., and Tahir, M. I. (1984) Laminar viscous flow through regular arrays of parallel solid cylinders. *International Journal of Multiphase Flows* 10, 515-540.

17. Dullien, F. A. L (1979) *Porous media, Fluid transport and pore structure*, Academic Press, New York.

18. Dupont, F., and Crochet, M. J. (1988) The vortex growth of a BKZ fluid in an abrupt contraction, *Journal of Non-Newtonian Fluid Mechanics* 29, 81-91.

19. Glowinski, R., and Pironneau, O. (1992) Finite element methods for Navier-Stokes equations. *Annual Review of Fluid Mechanics* 24, 167-204.

20. Guillope, C., and Saut, J. C. (1990) Existence of results for the flow of viscoelastic fluids with a differential constitutive law. *Nonlinear Analysis, Theory, Methods and Applications* 15, 849-869.

21. Harlen, O. G., Rallison, J. M., and Chilcott, M. D. (1990) High-Deborah-number flows of dilute polymer solutions, *Journal of Non-Newtonian Fluid Mechanics* 44, 229-265.

22. Harlen, O. G., Hinch, E. J., and Rallison, J. M. (1992) Birefringence pipes: the steady flow of a dilute polymer solution near a stagnation point, *Journal of Non-Newtonian Fluid Mechanics* 34, 319-349.

23. Higdon, J. L., and Ford, G. D. (1996) Permeability of three-dimensional models of fibrous porous media. *Journal of Fluid Mechanics* 308, 341-361.

24. Hinch, E. J. (1993) The flow of Oldroyd fluid around a sharp corner, *Journal of Non-Newtonian Fluid Mechanics* 50, 161-171.

25. Jackson, G. W., and James, D. F. (1986) The permeability of fibrous porous media. *Canadian Journal of Chemical Engineering* 64, 364-374.

26. James, D. F. and Mclaren, D. R. (1975) The laminar flow of dilute polymer solutions through porous media. *Journal of Fluid Mechanics* 70, 733-752.

27. Joseph, D. D. (1990) *Fluid Dynamics of Viscoelastic Liquids*. Springer-Verlag, New York.

28. Joseph, D. D., and Saut, J. C. (1986) Change of type and loss of evolution in the flow of viscoelastic fluids. *Journal of Non-Newtonian Fluid Mechanics* 20, 117-141.

29. Keunings, R. (1986) On the high Weissenberg number problem *Journal of Non-Newtonian Fluid Mechanics* 20, 209-226.

30. King, R. C., Apelian, R. C., Armstrong, R. C., and Brown, R. A. (1988) Numerically stable finite element techniques for viscoelastic calculations in smooth and singular geometries. *Journal of Non-Newtonian Fluid Mechanics* 29, 147-216.

31. Kuette, A. M., and Chow, C. Y. (1986) *Foundations of Aerodynamics,* Wiley, J. & Sons, New York.

32. Larson, R. G., and Higdon, J. L. (1986) Microscopic flow near the surface of two dimensional porous media. Part 2. Transverse flow. *Physics of Fluids* 1, 38-76.

33. Larson, R. G. (1988) *Constitutive Equation for Polymer Melts and Solutions*. Butterworth, New York.

34. Leal, L. G. (1991) *Laminar Flow in Convective Transport Processes*. Butterworth Heinemann Series in Chemical Engineering.

35. Lee, B. H. K (1989) Investigation of flow separation on a supercritical airfoil, *AIAA Journal,* vol. 26, 1032-1037.

36. Luo, X. L., and Mitsoulis, E. (1990) A numerical study of the effect of elongation viscosity on growth in contraction flows of polyethylene melts, *Journal of Rheology* 34(3) 309-342.

37. McLachlan, B. G. (1989) Study of a circulation control airfoil with leading/trailing edge blowing. *AIAA Journal,* vol. 26, 817-821.

38. Marchal, J. M., and Crochet, M. J. (1986) Hermitian finite elements for calculating viscoelastic flows. *Journal of Non-Newtonian Fluid Mechanics* 20, 187-207.

39. Marchal, J. M., and Crochet, M. J. (1987) A new mixed finite element for calculating viscoelastic flow. *Journal of Non-Newtonian Fluid Mechanics* 26, 77-114.

40. Metzner, A. B., and Marshall, R. J. (1967) Flow of viscoelastic fluids through porous media. *I&EC Fundamentals* 6, 393-400.

41. Moffatt, H. K. (1964) Viscous and resistive eddies near a sharp corner, *Journal of Fluid Mechanics* 18, 1-18.

42. Nishri, B., and Wygnanski, I. (1998) Effects of periodic excitation on turbulent flow separation from a lap, *AIAA Journal,* vol. 36, 547-556.

43. Northey, P. J., Armstrong, R. C., and Brown, R. A. (1990) Finite element calculation of time-dependent two-dimensional viscoelastic flow with the explicitly elliptic momentum equation formulation. *Journal of Non-Newtonian Fluid Mechanics* 36, 109-133.

44. Olbricht, W. L. (1996) Pore-scale prototypes of multiphase flow in porous media. *Annual Review of Fluid Mechanics* 28, 187-213.

45. Papathanasiou, T. D. (1996) A structure oriented micromechanical model for viscous flow through square arrays of fiber clusters. *Composites Science and Technology* 56, 1055-1069.

46. Patankar, S. V. (1980) *Numerical Heat Transfer and Fluid Flow*. McGraw-Hill, New York.

47. Pfenninger, W., and Groth, E. (1961) Low drag boundary layer suction experiments in flight on a wing glove of an F-94A airplane with suction through a large number of fine slots, *Boundary layer and flow control*, Vol. 2, Pergamon Press, Oxford, 981-999.

48. Rajagopalan, D., Armstrong, R. C., and Brown, R. A. (1990) Finite element for calculation of steady, viscoelastic flow using constitutive equations with a Newtonian viscosity, *Journal of Non-Newtonian Fluid Mechanics* 36, 159-192.

49. Rallison, J. M., and Hinch, E. J. (1988) Do we understand the physics in constitutive equation?. *Journal of Non-Newtonian Fluid Mechanics* 29, 37-55.

50. Renardy, M. (1988) Recent advances in the mathematical theory of steady flow of viscoelastic fluids. *Journal of Non-Newtonian Fluid Mechanics* 29, 11-24.

51. Renardy, M. (1989) Mathematical analysis of viscoelastic flows. *Annual Review of Fluid Mechanics* 21, 21-36.

52. Renardy, M. (1993) The stress of an upper convected Maxwell fluid in Newtonian field near a re-entrant corner, *Journal of Non-Newtonian Fluid Mechanics* 50, 127-134.

53. Rodriguez, S., Romero, C., Sargenti, M. L., Muller, A. J., Saez, A. E., and Odell, J. A. (1993) Flow of polymer solutions through porous media. *Journal of Non-Newtonian Fluid Mechanics* 49, 63-85.

54. Sangani, A. S., and Acrivos, A. 1982 Slow flow past periodic arrway of spheres, *International Journal of Multiphase flows* 8, 343-360.

55. Singh, P., Caussignac, Ph., Fortes, A., Joseph, D. D., and Laudgren, T. (1989) Stability of periodic arrays of cylinders across the stream by direct simulation. *Journal of Fluid Mechanics* 205, 553-571.

56. Singh, P., and Joseph, D. D. (1995) Dynamics of fluidized suspensions of spheres of finite size. *International Journal of Multiphase Flows* 21, 1-26.

57. Singh, P., Leal, L. G. (1994) Computational studies of the FENE dummbell model in a corotating two-roll mill, *Journal of Rheology* 38, 485-517.

58. Singh, P., and L. G. Leal (1995) Finite-element simulation of flow around a $3\pi/2$ corner using the FENE dummbell model. *Journal of Non-Newtonian Fluid Mechanics* 58, 279-313.

59. Singh, P., and L. G. Leal (1993) Finite-element simulation of the Start-up problem for a viscoelastic fluid in an eccentric rotating cylinder geometry using a third-order upwind scheme. *Theoretical and Computational Fluid Dynamics* 5, 107-137.

60. Stollery, J. L., and Dyer, D. J. (1989) Wing section effects on the flight performance of a remotely piloted vehicle, *AIAA Journal,* vol. 26, 932-938.

61. Szeri, A. J., Wiggins, S., and Leal, L. G. (1991) On the dynamics of suspended microstructure in unsteady, spatially inhomogeneous two-dimensional fluid flows. *Journal of Fluid Mechanics* 228, 207-241.

62. Szeri, A. J., Miliken, W. J., and Leal, L. G. (1992) Rigid particles suspended in the time-dependent flows -irregular versus regular motion, disorder versus order, *Journal of Fluid Mechanics* 237, 33-56.

63. Tabata, M., and Fujima, S. (1991) An upwind finite element scheme for high Reynolds number flows, *International Journal for Numerical Methods in Fluids* 14, 305-322.

64. Thompson, B. E. (1989) Trailing edge region of airfoils, *AIAA Journal,* vol. 26, 225-234.

65. Vorobieff, P. V., and Rockwell, D. O. (1998) Vortex breakdown on pitching delta wing: Control by intermittent trailing-edge blowing, *AIAA Journal,* vol. 36, 585-589.

66. Wuest, W. (1961) *Theory of boundary layer suction to prevent separation. Boundary layer and flow control.* Vol. 1, Pergamon Press, Oxford, 196-208.

67. Yon, S. A., and Katz, J. (1998) Study of the unsteady flow features on a stalled wing, *AIAA Journal,* vol. 36, 305-312.

68. Zanden, J. V., and Hulsen, M. (1988) Mathematical and physical requirements for successful computations with viscoelastic fluid models. *Journal of Non-Newtonian Fluid Mechanics* 29, 93-117.

69. Zick, A. A., and Homsy, G. M. (1982) Stokes flow through periodic arrays of spheres. *Journal of Fluid Mechanics* 115, 13-26.